Alma Mater Studiorum – Università di Bologna

in cotutela con Babol Noshirani University of Technology

DOTTORATO DI RICERCA IN CHIMICA

Ciclo XXXII

Settore Concorsuale: 03/B1

Settore Scientifico Disciplinare: CHIM/03

Fabrication of supercapacitors based on cellulose nanocomposites for use in biological fuel cell

Presentata da: Mehrdad Mashkour

Coordinatore Dottorato	**Supervisors**
Prof. Domenica Tonelli	Prof. Mostafa Rahimnejad
	Prof. Francesca Soavi
	Advisor
	Prof. Mahdi Mashkour

Esame finale anno 2021

To Dear Mom and Dad

To acknowledge just a little portion of your sacrifices. Without your supports, I never would have been able to get over the obstacles along the life road. I'm really fortunate that you are my parents, and I thank God for that.

Contents

Figures

Tables

Acknowledgments

My deep and sincere appreciation goes to my thesis supervisors Prof. Mostafa Rahimnejad and Prof. Francesca Soavi. They have been excellent mentors and have outstandingly directed me during my research at Babol Noshirvani University of Technology (BNUT, Iran) and University of Bologna (Unibo, Italy). They have profoundly helped me to attain excellent results, gain experience, and encouraged me to grow professionally with an international network. Indeed, during my visiting period in Italy, I was involved in the Italy-South Africa joint Research Programme 2018-2020, supported by the Italian Ministers of Foreign Affairs and of the Environment, that target the integration of high-power energy storage systems for sustainable water and renewable sources management (https://site.unibo.it/isarp.en),

I am also grateful to my advisor Prof. Mahdi Mashkour in Gorgan University of Agricultural Sciences and Natural Resources (Iran), for his great supports, especially in fabricating cellulosic nanocomposites.

I am also thankful to Prof. Carlo Santoro at the University of Milan Bicocca for introducing new concepts of MFC systems to me during several meetings and for his helpful collaboration in this thesis.

I would like to thank my defence examiner: Prof. Mohammad Hossein Sarrafzadeh, Prof Cristian Torri, Prof. Ghasem Najafpour and Prof. Mohsen Jahanshahi for their valuable comments on my PhD thesis.

I would like to appreciate Mir Taher Motahari at Danesh Gostar Hamgam Ba Sanat spin-off (Babol-Iran), who helped in MFC design and fabrication.

I would like to thank Prof. Catia Arbizzani at the Laboratory of Electrochemistry of Materials for Energetics (LEME) at Unibo for her help and excellent conditions during my stay at LEME.

I would also sincerely thank my precious and lovely colleagues at LEME, especially dear Federico Poli, for his great help and also Dr. Francesca De Giorgio, Dr. Irene Ruggeri, Dr. Morteza Rahmanipour, Mohammad Said El Halimi, Antonio Terella, and Alessandro Brilloni for their friendship.

I am thankful to my dear colleagues at Biofuel and Renewable Energy Research Center of BNUT; Dr. Kasra Pirzadeh, Dr. Hoda Ezoji and Dr. Masoumeh Pourali for their supports and friendship.

I would like to thank Dr. Saeed Khoshhal at Membrane Research Laboratory of BNUT for his great help during my Ph.D. and Dr. Masoumeh Hezarjaribi at Advanced Membrane Technology Research Lab of BNUT for her help in some analyses of my thesis.

A special thank goes to the office of International Affairs and Scientific Collaborations of BNUT and the International Office of Unibo for preparing the agreement of Ph.D. Cotutelle program for me.

I would also thank my dear friend Dr. Keyvan Malaie and Dr. Arash Sedghi, who helped me in my first days in Bologna. I am also grateful to my roommate in Bologna, Soheil Jalili, for all the beautiful days we had in Italy and my lovely landlady Gian Carla Draghetti who is friendly and provided an excellent stay in her apartment.

I would like to kindly acknowledge the financial supports provided by the Ministry of Science, Research and Technology of Iran for my stay in Italy during my Ph.D., Babol Noshirvani University of Technology (grant number: BNUT/5150010/1394) for my Ph.D. research activities, National Science Foundation of Iran (INSF-95819857), Italy-South Africa joint Research Programme 2018-2020, Italian Ministers of Foreign Affairs and of the Environment.

Very special thanks to dear Neda Rahmati, who permanently motivates me in difficulties and demanding conditions. I should appreciate her for the great and invaluable help during my Ph.D.

Last but foremost, I would like to appreciate my precious family members because I could surely not attain this great success without their supports.

Abstract

Today, because of the inexhaustibility of their resources and the reduction of environmental pollution, the consumption of renewable energy has been significantly considered by researchers. Microbial fuel cells (MFCs) are known to be attractive renewable energy sources in which microorganisms, as biocatalysts, are responsible for the decomposition of organic matter and thus simultaneously produce electricity and carry out the biological treatment. One of the greatest concerns of this technology is its poor power performance relative to the expense of its components. In this context, inexpensive cellulose and super-capacitive materials can improve MFC performance.

The aim of this Ph.D. thesis is to develop novel concepts of super-capacitive MFCs by focusing on nanocomposite anodes and cathodes constructed from low-cost bacterial cellulose (BC), carbon materials, and conductive polymers.

Specifically, the innovative concept of a monolithic membrane electrode assembly (MEA) produced using a binder-less coating process offers excellent capacitive features for MFCs, and BC-based capacitive bio-anodes were produced and exhibited outstanding capacitive properties in a super-capacitive MFC. Both electrode designs increased MFC electricity generation by improving MFC capacitance.

Chapter 1 provides necessary concepts on supercapacitors, MFCs, and different parts of each technology and introduces cellulosic nanomaterials utilized in energy storage devices. Finally, state of art in the field of super-capacitive MFCs is reported.

Chapter 2 provides the details of the processes and experiments exploited in this thesis. Chemicals, electrode fabrication methods, MFC structure, incubation of MFC, chemical and physical characterization methods, pre-treatment of the samples, electrochemical test, and each test's condition were reported.

Chapter 3 reports the results and related discussion of the physical and chemical properties of the monolithic BC-based MEA. The results of various characterization methods such as spectroscopy, microscopic imaging, X-ray diffraction, and thermal

analysis are discussed. This chapter's main focus is on BC-Nano zycosil (NZ) coating and its excellent properties for MEA in MFC systems.

Chapter 4 presents electrochemical properties of the BC-based MEA and compares them with the features of a commercial gas diffusion electrode (GDE) in a single-chamber MFC cell. Indeed, the main electrochemical features required for an air-cathode in a single chamber MFC are discussed, such as catalytic activity, barrier properties, energy and power production, columbic efficiency, and capacitance in the presence of each air-cathodes.

Chapter 5 provides the results of BC-based bioanode usage in a super-capacitive single-chamber MFC. The role of polyaniline and carbon nanotubes (CNTs) and the anodic biofilm on the cellulosic bio-anodes' capacitive response is studied in detail with various electrochemical methods, especially impedance spectroscopy. The double anode concept for improving the double-layer capacitance of the MFC is discussed. Also, the effect of capacitance on the power output of the system is explained.

In conclusion, the use of BC, a biopolymer synthesized by some species of bacteria, as a porous media membrane for fabricating a capacitive MEA in MFC was performed by a novel method. Binder-less coating of that side of BC, exposed to the air, with CNTs made a homogeneous coating by which the impedance of the MEA decreased noticeably. On the other side of BC, exposed to anolyte, NZ coating could create a barrier to oxygen cross-over and prevent anolyte leakage. This monolithic MEA structure with a low expense of fabrication is introduced for the first time in this thesis. MFC performance in the presence of the cellulosic MEA compared with the GDE showed higher power density, lower internal resistance, higher catalytic activity, and higher capacitance.

BC-based anodes demonstrated excellent capacitance. BC-CNT was covered with PANI through pulse electro-polymerization in this work. CNTs and PANI as super-capacitive materials showed different capacitance trends vs. anodic biofilm formation. PANI as a biocompatible conductive polymer provided a better condition on BC-CNT-PANI anode for microbial colonization. The effect of PANI on the capacitive response of biofilm by impedance was studied for the first time. Finally, MFC performance was improved by short-circuiting BC-CNT to a high capacitance PANI-modified BC-CNT as an additional anode giving rise to enhancing double-layer capacitance of anode and thus higher apparent capacitance and power density of the cell.

Chapter 1

Introduction

1.1 General overview of energy issue

1.1.1 Energy production and the world energy crisis

Today, with the rise of the world's population and numerous industries' advancement, energy resource usage has increased. Fossil fuels have the greatest share of the supply of this tremendous volume of electricity. Hence, the presence of these resources has influenced the fate of many countries and nations after they were found and realized by humankind. The world has learned that access to energy means controlling many things [1]. Today, fossil fuel consumption is growing significantly, with the development in the quality of living, the growth in the world's population, and developing countries' industrialization. However, the excessive use of fossil fuels, in addition to the further degradation of their resources, has caused significant detrimental environmental impacts, which have contributed to global climate change and environmental threats for humans and other living species [2].

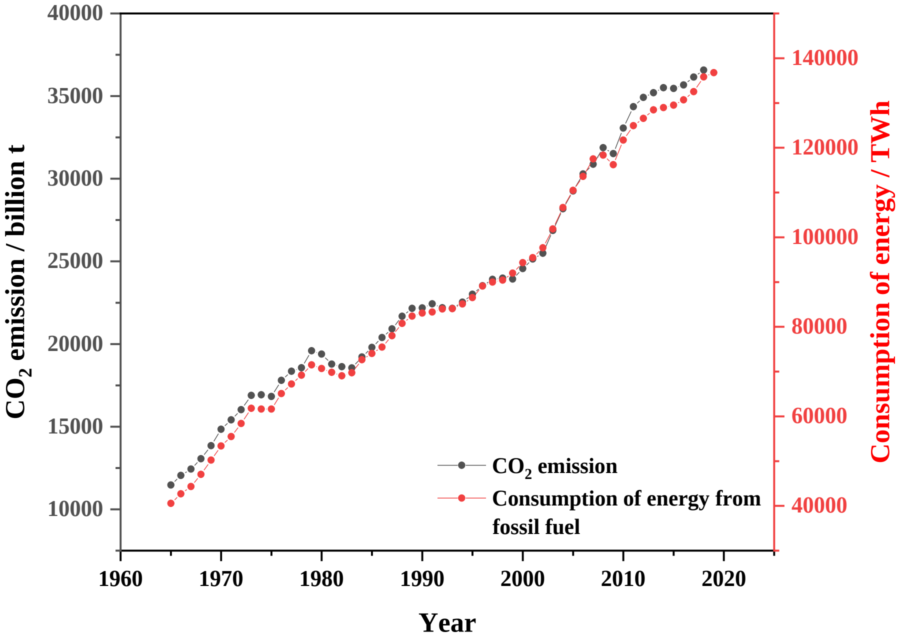

Figure 1.1.1.1. Energy consumption of fossil fuels and carbon dioxide emissions from 1965 to 2019

Figure 1.1.1.1 shows the amount of energy consumption from fossil fuels in the world and the amount of carbon dioxide emissions in the atmosphere from 1965 to 2019. Due to the growing need of human society, energy consumption has increased significantly during these years, while the increase in energy consumption has been accompanied by an increase in the amount of carbon dioxide emitted into the atmosphere.

Despite all this, the growing need for energy on the one hand and the limitation of fossil fuel resources, and the sound of the alarm, on the other hand, have led the world to move to other energy sources. Membership in international agreements related to reducing carbon dioxide emissions and the importance of environmental issues, even in the political community in many developed countries of the world, has led to the adoption and implementation of various laws to control pollution from fossil fuels. Hence, the global community is slowly moving towards finding more sustainable energy production methods, minimizing waste, reducing air pollution from vehicles, protecting forests, and reducing greenhouse gas emissions [3].

Excessive use of fossil fuels is causing global warming by carbon dioxide production. Therefore, the use of renewable sources and producing less carbon dioxide is of today's human needs. Unlimited sources of energy that do not affect the environment, have low carbon emissions, and at the same time are not limited to a specific part of the planet are sources that can be used as a substitute for fossil fuels. They are renewable energy sources [4].

1.1.2 Renewable energy sources

In one division, energy sources are divided into three categories: fossil fuels, nuclear and renewable energy, among which renewable resources play an essential role in the future of the world, so that the use of these resources, in addition to meeting the domestic needs of each country, can minimize emissions of air pollutants and greenhouse gases [5]. Renewable energy refers to the types of energy whose production source is a kind of inexhaustible and clean energy. Renewable energy sources include water energy behind dams, geothermal energy, solar energy, wind energy, sea waves, and biomass energy, which provide a significant percentage of the world's total energy needs [6]. Based on research conducted by a group of researchers, the global scenario for using renewable energy by 2040 is presented in Table 1.1.2.1 [7]. Accordingly, by 2040, almost half of the world's energy needs will come from renewable sources.

Figure 1.1.2.1 shows the growth of the use of renewable energy sources to generate electricity over time. According to the graph, the use of coal, which still produces the most energy, shows a declining trend.

Table 1.1.2.1. Scenario of renewable energy by the end of 2040 [7].

	2010	**2020**	**2030**	**2040**
Total consumption(million tons oil equivalent)	10549	11425	12352	13310
Biomass	1313	1791	2483	3271
Hydropower	285	358	447	547
Geothermal	86	186	333	493
Wind	44	266	542	688
Solar	15.4	69	260	548
Photovoltaic	2	24	221	784
Total source of renewable energy	1745.5	2964.4	4289	6351
Renewable energy source contribution (%)	16.6	23.6	34.7	47.7

However, according to Figure 1.1.2.1, gas among fossil fuels is increasing its share of the world's energy supply, which is less polluting than fossil fuels due to lower carbon dioxide emissions than oil and coal. Among renewable sources, the energy produced by dams has decreased in recent years due to drought and depletion of rivers' water.

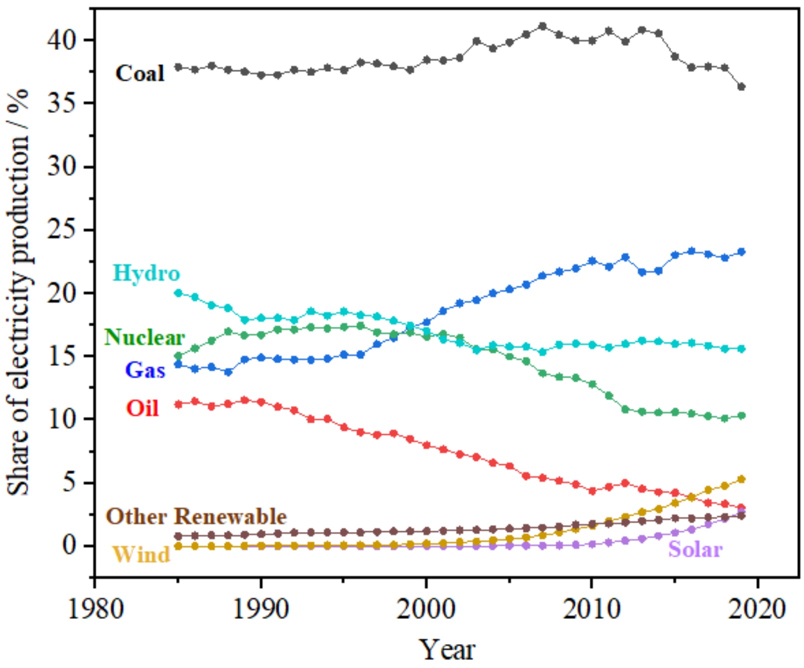

Figure 1.1.2.1. Electricity generation in the world using various energy sources including coal, gas and oil, hydropower, wind, solar, nuclear energy and other renewable energy

The use of renewable solar and wind energy is growing with a considerable slope and taking a more significant share in humans' production of energy. However, the percentage of other renewable sources such as biomass is still small, and the energy generation by them is much less compared to its other renewable counterparts. Therefore, more research needs to be done to improve the status of these resources.

As mentioned, renewable energy sources are unlimited. However, these resources face problems, such as the dependence of the intensity of energy production on environmental conditions and, consequently, the inability to continuously produce energy, limiting the use of these resources to provide energy in a wide range. An appropriate solution to overcome this limitation is to use energy storage devices. In this way, the energy produced from these unlimited sources can be stored at proper times, and their accumulated energy can be used continuously. Therefore, with energy storage, renewable sources can be considered reliable sources for energy production and supply.

1.2 Electrochemical energy storage device

Electrochemical devices used to store energy include batteries and supercapacitors. Figure 1.2.1 compares energy storage devices in terms of power density and energy density as a Ragone plot. Electrolytic capacitors are also included. Among the technologies, supercapacitors have been widely welcomed by researchers for covering a wide range of energy and power [8, 9].

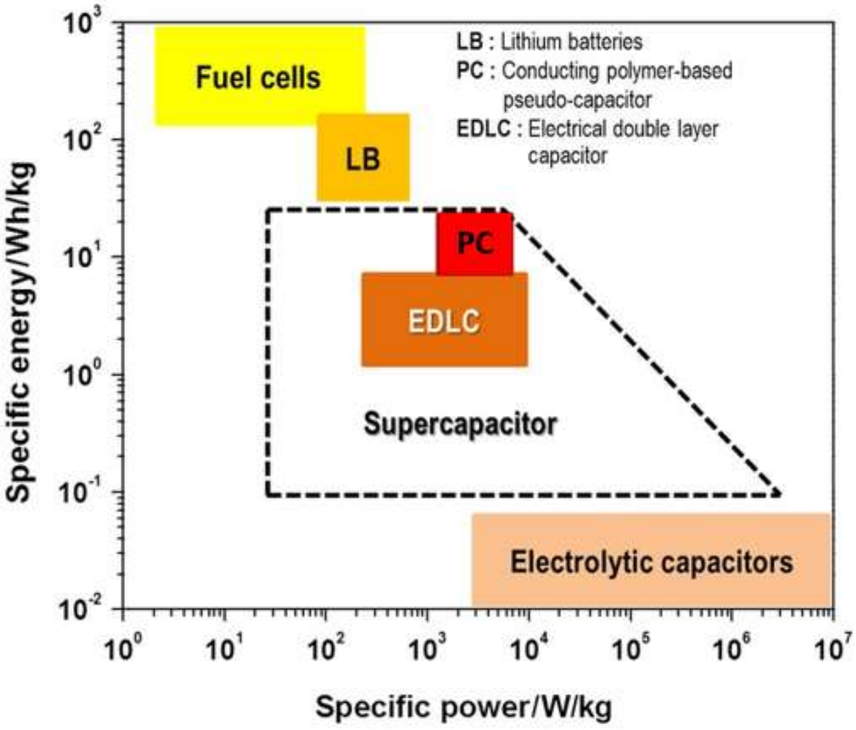

Figure 1.2.1. Ragone plot range for different kind of energy storage devices. Reprinted from ref. [10], with permission from Wiley.

1.2.1. Supercapacitors

A supercapacitor is actually a capacitor with a much higher capacity than other capacitors. The energy that can be stored in supercapacitors is 10 to 100 times higher than that of electrolytic capacitors. Supercapacitors are able to store and deliver electrical charge faster than rechargeable batteries. They are very useful when charging and discharging is fast. Unlike conventional capacitors, supercapacitors do not use conventional solid-state dielectrics. They can be classified in EDLC (electrostatic double-layer capacitor) and EPC (electrochemical pseudo-capacitor), which are briefly defined as follows [11, 12].

EDLC: Features carbon electrodes that store charge by an electrostatic process that set up the so-called double-layer capacitance. Charge separation occurs at the Helmholtz layers, i.e., at the interface between the electrode surface and the electrolyte.

EPC: Metal oxides and conductive polymers are used as electrodes. They feature a capacitive behavior that arises from fast, reversible faradic processes.

Each electrochemical capacitor has two electrodes that are mechanically separated by a separator and also connected to each other by ions through an electrolyte. An electrolyte is a combination of positive and negative ions dissolved in a solvent such as water. For each of the two electrodes, the surface is actually the area where the liquid electrolyte is in contact with the electrode's solid surface. Electrode polarization creates two electrical layers at the electrode/electrolyte interface. These two layers consist of two layers of electric charge: those present in the electrodes and a layer of ions with opposite polarity derived from electrolyte-soluble ions. These two layers are separated by a dielectric layer (consisting of solvent molecules such as water) in the internal Helmholtz plate. This charge arrangement can be modeled with the so-called “electrical double layer” Solvent molecules separate from the oppositely polarized ions by physical adsorption to the electrode's surface. They are assumed to be ideal molecular dielectric. In this process, there is no charge transfer between the electrode and the electrolyte. Therefore, the force that causes this adsorption is mainly electrostatic. The adsorbed molecules are polarized but do not undergo any chemical changes due to the lack of charge transfer between the electrode and the electrolyte [13].

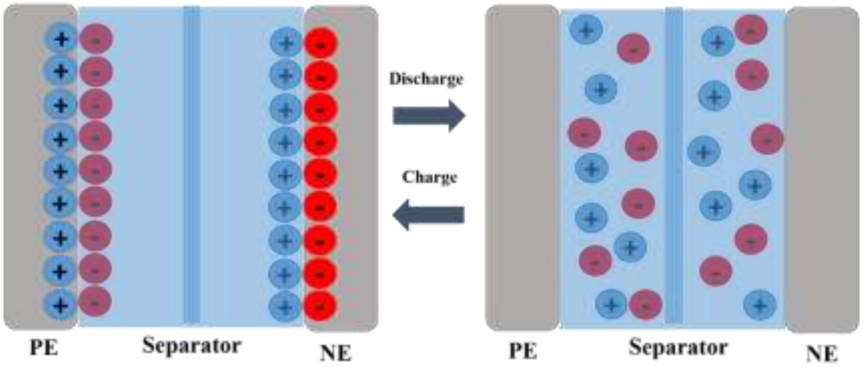

Figure 1.2.1.1. Concept of a supercapacitor operation

In pseudocapacitive electrodes, the charge is stored by fast and reversible Faradic redox reactions on the electrodes' surface. When this process provides a capacitor-like response, i.e., the stored charge linearly depends on the applied voltage, the electrode is termed “pseudocapacitive.” Given that the pseudo-capacitive process involved all the electrode bulk and not only its surface, pseudocapacitance often exceeds the double-layer capacitance for the same surface. Materials that show redox behavior for use as electrodes in pseudo-capacitors include metal oxides such as MnO2 doped in conductive electrode materials, as well as conductive polymers such as polyaniline coated on the surface of electrode materials [14-16].

To make supercapacitors, there are generally two methods that lead to the construction of symmetrical supercapacitors (same electrodes) and asymmetric (different electrodes), as shown in Figure 1.2.1.2.

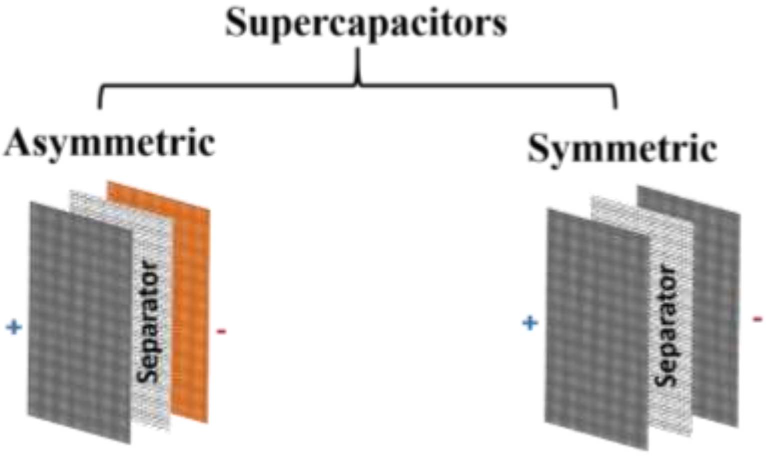

Figure 1.2.1.2. Symmetrical and asymmetrical supercapacitors

Electrode materials play a critical role in supercapacitors. Therefore, manufacturing electrodes with desirable properties and lower cost is an essential factor in constructing supercapacitors.

The materials utilized to make the electrodes of supercapacitors have high electrical conductivity, good thermal and chemical stability, and high cross-section and be environmentally friendly, corrosion-resistant, and inexpensive. In general, the smaller the electrode's pores, the higher the specific area and specific capacitance, resulting in an increase in energy density. On the other hand, small pores increase the equivalent series resistance and thus reduce the power density. Therefore, electrode porosity should be appropriately designed to match higher current and high energy performance. In general, the materials used to make supercapacitors electrodes include carbon materials, conductive polymers, and metal oxides, which are discussed below [9].

1.2.1.1 Carbon materials

Due to the low cost and appropriate availability of carbon-based raw materials and their ease of synthesis on an industrial scale, these materials are widely used in various fields. At high voltages applications, the materials used to make the electrodes must be free of oxygen-containing functional groups such as COOH, OH, and C=O because they are easily degraded at high voltage levels. Carbon nanotubes and graphene nanosheets, which have the sp^2 carbon material and have no bond on their surface, are ideal options for use in supercapacitors (Figure 1.2.1.1.1). Graphene is a suitable choice for high-efficiency energy storage systems due to its improved capacitance. The main attractive features of graphene are high flexibility, high electrical conductivity, and thermal stability. Carbon nanotubes can also form on a conductive surface without using a binder, which minimizes the electrode contact resistance in the supercapacitors. In addition to chemical stability, these materials have a high specific surface area that acts as a wide interface between the electrolyte and the electrode and increases storing energy [17].

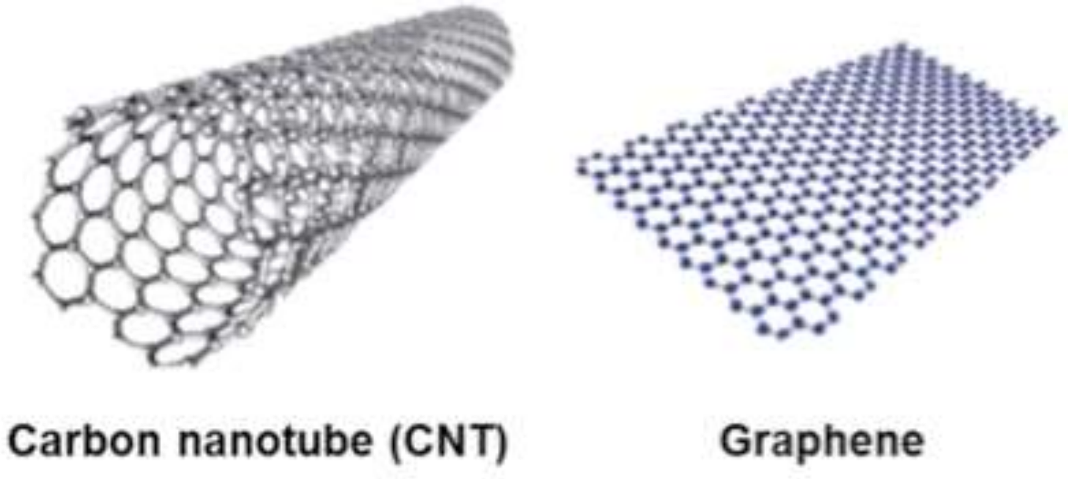

Figure 1.2.1.1.1. Structures of CNT and graphene

1.2.1.2 Metal oxides

Another material used to make electrodes in supercapacitors is metal oxides, which form active sites for the redox process. The most widely used metal oxides are nickel oxide, tantalum oxide, manganese oxide, tin oxide, aluminum oxide, iron oxide, and ruthenium oxide [18].

1.2.1.3 Conductive polymers

Most polymers are electrically insulating. In 1977 for the first time, researchers converted Polyacetylene, an insulating polymer, into an electrically conductive polymer using a chemical treatment. Conductive polymers generally can become conductive or semiconductors for electrical current. Despite the short history of these materials, having conductivity and pseudo-metallic properties resulted in researchers' considerable attention to this type of polymers. In addition to these materials' mentioned features, they have flexibility and low density, and their structures are modified by easy methods [19]. Electrodes based on conductive polymers have high capacitance, among which we can mention aniline-based polymer electrodes as one of the most efficient capacitive electrodes [8].

Polyaniline is a conjugated polymer whose conductive properties were discovered in the early 1980s using a doping process in various fields, including battery electrodes, corrosion coatings, and electromagnetic shielding devices. Using a salt, the imine nitrogens are protonated on the polyaniline structure in the doped emeraldine oxidation state, which makes these polymers electrically conduct. Doping agents can be added to the performing reaction till all imine nitrogens (half of all nitrogens) are doped, and this is possible by controlling the acidic doping solution. Therefore, by the use of a doping process, polyaniline can be converted to a conductive acid or be changed into a fully doped state from an insulated one. This polymer's doping process is possible chemically, electrochemically, and by using acids such as HCl and bases such as NH_4OH. In addition to polyaniline conductivity, the doping process significantly affects its molecular architecture [19, 20]. The PANI structures are visible in Figure 1.2.1.3.1.

Figure 1.2.1.3.1. Different forms of polyaniline

1.2.1.4 Cellulose and nano cellulose

In recent years, environmentally friendly materials that have various applications have received much attention. As the most abundant biopolymer on earth, cellulose has been widely used in multiple industries for many years. Polymeric cellulose is biodegradable, renewable, and the main constituent of all plant fibers. It is composed of β-D-glucopyranose repeating units and is mainly concentrated in the secondary cell wall. The primary components of wood fiber walls are microfiber bundles, sometimes called microfibrils. The diameter of a microfibril is 20-50 nm depending on the cellulose source and measurement method. A microfibril is made up of primary cellulose fibrils along with other wood components such as hemicelluloses, proteins, pectin, and lignin. Primary fibril is the smallest cellulose structure, consisting of 36 parallel cellulose molecules joined together by hydrogen bonds and consisting of amorphous and crystalline moieties. Nanocellulose generally refers to cellulosic materials that have at least one dimension on the nanometer scale. Nanocelluloses are produced in different ways and from various lignocellulosic sources. Nanocelluloses are classified into three main groups based on their dimensions, function, and preparation methods, which include cellulose nanocrystals, nanofibrillated cellulose, and bacterial nanocellulose,

1.2.1.4.1 Bacterial cellulose

Bacterial cellulose is the product of the biological synthesis of certain bacteria such as *Acetobacter xylynum*, *Acetobacter pasterurianum*, *Acetobacter rancens*, *Bacterium xylinoides*, and *Sarcina ventriculi*. Bacterial cellulose has a higher purity due to its lack of association with other types of biopolymers such as lignin and hemicellulose found in plants, as well as its tensile strength and ability to be absorbed much higher. In terms of chemical structure, this type of cellulose is similar to plant cellulose, but from a crystallographic point of view, its structure is different, and unlike type 1 cellulose of plants that have a single slope structure, bacterial cellulose crystal is of three slope type. The bacterium performs the biological synthesis of cellulose to create protection for itself, and these cellulose nanofibers are produced as three-dimensional networks at the surface of the culture medium. The resulting nanofiber network is extracted as a hydrogel from the culture medium, and after purification and removal of the constituent bacteria, it will be ready for consumption in different users [21]. Bacterial cellulose is an enhancer for the design of efficient and environmentally friendly nanocomposites. This renewable and biodegradable material has a Yang modulus of about 114 GPa and a high degree of crystallization (about 90%). The average degree of polymerization (DP) of bacterial cellulose is higher than plant cellulose and is about 14,400 units [22]. Optimal production and application of bacterial cellulose in the manufacture of nanocomposites, foams, and hydrogels with the aim of special industrial and medical applications are among the items that have attracted the attention of many researchers active in materials science.

1.2.1.5 Cellulose based supercapacitors

Cellulose is the primary material of paper and the most abundant biopolymer on the earth's surface and is also a key source of renewable materials on an industrial scale. Intrinsic hydrophilicity, mechanical flexibility, three-dimensional structure, and fibrous structure can make cellulose suitable for forming strong and stable structures from compressed films to hydrogels. These properties make cellulose an excellent structure in combination with functional materials. Recently, the use of cellulosic paper-based electrodes in the manufacture of electrical energy storage devices has become a hot topic in the scientific community [23-25].

Cellulose is inherently an insulator and cannot store electrical charge alone. However, if cellulose is modified with a conductive layer or conductive filler, electrically conductive composites will be formed that can be used as high-efficiency flexible electrodes in combination with active materials for energy storage applications [26, 27]. Numerous electrical energy storage devices are based on cellulose composites in which cellulose is used as a flexible substrate to strengthen the structure and increase the available surface area and has also shown attractive electrochemical performance [28-30]. Figure 3-2 shows a summary of the properties of cellulosic materials along with the materials used in them to make supercapacitors.

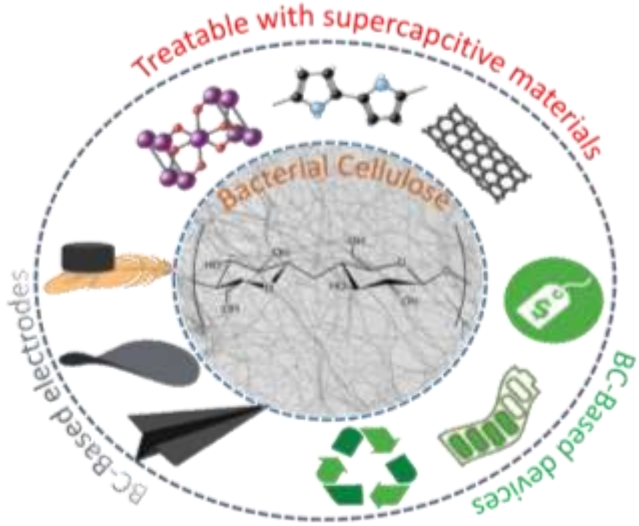

Figure 1.2.1.5.1. The properties of bacterial cellulose in supercapacitors

Due to all the above properties, BC is considered a suitable option in manufacturing components of electrical energy storage devices, especially supercapacitors.

1.2.2 Fuel cells

Fuel cells are electrochemical devices that convert the inherent chemical energy of fuels directly into electrical energy. Because the technology avoids the heat generation and mechanical work of conventional energy generation methods, fuel cells are not subject to the thermodynamic constraints of conventional heat engines defined based on the Carnot engine's efficiency [31]. Hence, fuel cells promise to produce energy with high efficiency and low environmental impact (in other words, the least pollutants). Fuel cells can use a variety of fuels and oxidants. However, today the most popular are conventional fuels such as natural gas and its derivatives or hydrogen, in which air acts as an oxidizing agent. In this system, fuel is continuously injected into the anode (negative electrode) and oxidized continuously on the cathode side (positive electrode). Figure 2.4.1 shows the schematic of a hydrogen fuel cell.

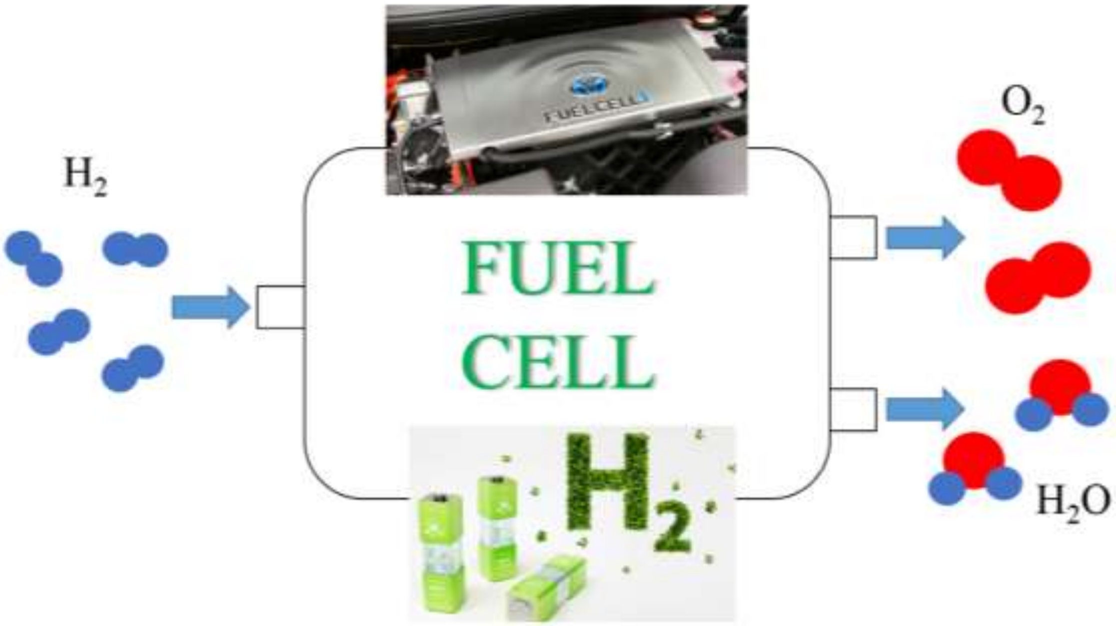

Figure 1.2.2.1. Schematic of a hydrogen fuel cell

At the fuel cell anode, ionized hydrogen gas releases electrons and protons, resulting in energy generation:

$$2H_2 \longrightarrow 4\,H^+ + 4e^- \qquad 1.2.2.1$$

At the cathode, oxygen reacts with protons and electrons at the anode, leading to water formation.

$$O_2 + 4H^+ + 4e^- \longrightarrow 2H_2O \qquad 1.2.2.2$$

Electrons flow in the external circuit from the anode to the cathode, and H^+ passes through the electrolyte. The efficiency of such processes strongly depends on the presence of electrocatalysts, the most efficient being Pt-based.

It is of great importance to note the electrolyte should only allow transferring to protons and while it performs as an insulator for electron transfer. Otherwise, the electrons will not flow in the external circuit, and as a result, the fuel cell will be short-circuited.

Theoretically, any material that can be chemically oxidized and continuously supplied can be utilized as a fuel in the fuel cell anode part. Similarly, an oxidizer can be any fluid that can be reduced at any rate. For operational reasons, the most common oxidant is the gaseous oxygen of the air. Additionally, the kinetic constraints for chemical catalysts oxidizing common fuels, including hydrogen, methane, and methanol in conventional fuel cells, made a tendency to biological fuel cells in which biocatalysts can oxidize a wide range of fuels.

1.2.3 Biological fuel cells

Like conventional fuel cells, biological fuel cells are operated by supplying fuel to the anode and oxidizing agent supply to the cathode. These cells convert the chemical energy received from organic matter directly into electrical power. In an anode, a fuel (e.g. glucose and acetate) is oxidized as follows:

$$C_6H_{12}O_6 + 6H_2O \longrightarrow 6CO_2 + 24H^+ + 24e^- \quad , E_o = 0.014\,V \qquad 1.2.3.1$$

At the cathode, the oxidant (oxygen) is reduced due to the presence of a chemical catalyst (or enzyme):

$$6O_2 + 24H^+ + 24H^- \longrightarrow 12H_2O \ , \ \ E_o = 1.23\,V \qquad 1.2.3.2$$

These chemical reactions lead to the production of electric current fluxes due to the production of electrons and protons from fuel oxidation. The theoretical potentials of cells for these reactions are similar to conventional fuel cells. The distinguishing feature of biological fuel cells is the use of organisms. In general, biological fuel cells are operated using biocatalysts and enzymes.

The tendency to use biological fuel cells dates back to the mid-nineteenth century. When Rorbeck et al. designed a fuel cell in which *Clostridium butyricum* was used as a biological substance to produce hydrogen during the glucose fermentation process. At first, Potter at Durham University in the UK showed that microorganisms could generate voltage and current [32]. Cohen revived Potter's idea in 1931 and showed that a batch system of biofuel cells could produce voltages above 35 volts [33]. Algae and bacteria were the first organisms used in biofuel cells, and in 1963 these cells were commercially exploited as a source of energy in radios and marine applications. NASA has also considered biofuel cells as long-term spaceflight to convert biological waste into electricity but has not achieved commercial success. Cells were later considered during the oil crisis of the 1970s and 1980s, and today we see a great deal of interest from scientists in this type of fuel cell. The reason for the tendency towards biological fuel cells is their ability to operate at ambient temperature and pressure. Neutral electrolytes are commonly used in these cells, and bio-catalysts (such as enzymes and pure and specific micro-organisms) may also be used. There are two main types of biological fuel cells: microbial fuel cells (MFCs) and enzyme fuel cells.

1.2.4 Microbial fuel cell

In the primary MFCs, the anode and cathode are placed in aqueous solutions in chambers separated by a membrane. In the anode chamber, microbes oxidize an electron donor fuel to produce electrons and protons. Microorganisms transfer electrons from an electron donor to an electron acceptor with higher electrochemical potential and generate electrical current. Electro-active microorganisms that accumulate as a biofilm on the surface of the anode carry out the oxidation reaction of organic matter, leading to the production of protons and the formation of an electric current. Finally, carbon dioxide is released as a byproduct of the oxidation process. Electrons and protons are consumed in the cathode chamber, the oxygen molecule is reduced, water molecules are formed, and electricity is generated [34-36].

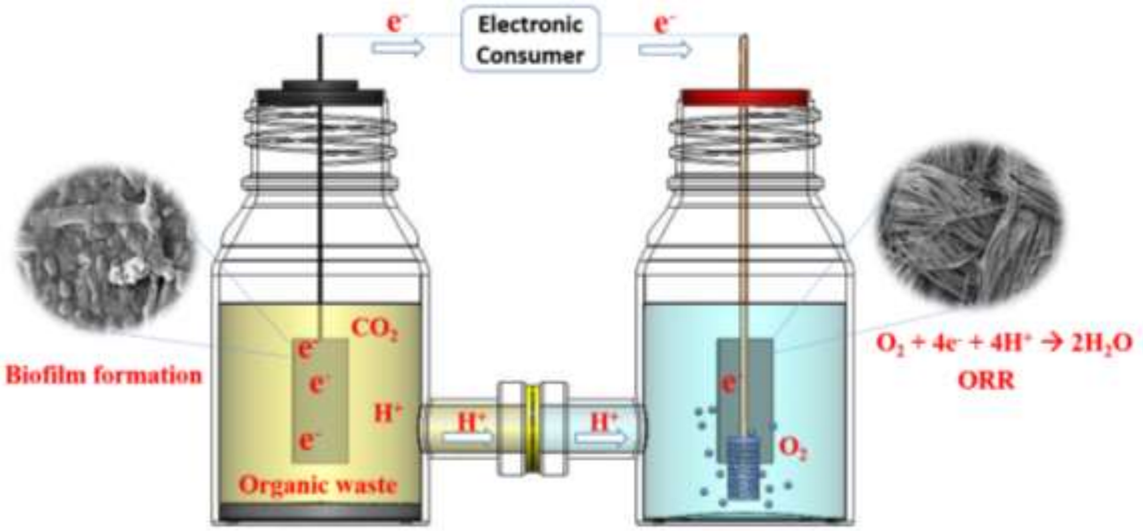

Figure 1.2.4.1. Schematic of a conventional H-type MFC with separated anaerobic and aerobic chambers

1.2.4.1 Microbial fuel cell principles

An MFC is based on the production of electrons by microorganisms and their electron transfer chains. The electron transport chain includes the microorganism's cell membrane and mitochondria for eukaryotes, where the proteins in it result in energy generation. In aerobic respiration, the main reaction is to oxidize an energy-rich substrate, like glucose, to reduce nicotine adenine dinucleotide (NAD $^{+}$) to NADH by receiving electrons from glucose. NADH is then oxidized, and the electrons are passed to adenosine triphosphate (ATP). In the case of anaerobic respiration, acetyl-CoA serves as an electron receptor, and then by the citric acid cycle, ATP is produced [37]. Electron uptake in microbial cells occurs before ATP accepts electrons and delivers them to the anode electrode. Since the microbial membrane isolates the reducing species produced in microbial cells during the metabolic process, the contact between the cells and anode usually does not give rise to considerable electron transfer, except in possible cases that electrons are directly transferred to the anode surface.

1.2.4.2 Microbial fuel cells' configuration

MFCs generally have two structures, two-chamber, and single-chamber. The two-chamber structure, in which the anode and cathode electrodes are located in two separate chambers with membranes, is an old structure, but due to some applications of MFCs such as biosensing, hydrogen production, and synthesis of some products, this structure is still of importance to researchers in this field [38, 39]. However, the use of membranes in this structure incurs a relatively high cost to the system and also increases the internal resistance of the MFC due to the electrical resistance of the membrane as well as the considerable distance between the anode and cathode electrodes. Due to the shortcomings of this structure, single-chamber fuel cells have been introduced. In the single-chamber structure, the membrane can be removed, and also, the oxygen required at the cathode part is provided in high concentration by the air compared to the two-chamber structure that uses limited oxygen dissolved in water [40]. By removing the cathode chamber and membrane, the working volume of the cell, the cost of construction, and the fuel cell system's internal resistance are reduced, making this type of structure more attractive for generating electricity than the two-chamber design. However, the removal of the membrane in the MFC structure will lead to the infiltration of oxygen into the anode chamber, and in the long-term run may disrupt the anaerobic conditions of the chamber and the activity of anaerobic microorganisms that make up the anode microbial biofilm. It also affects cell performance in anodic wastewater treatment and reduce the removal rate of organic matters. Therefore, creating a balance between the positive and negative effects of membranes on the performance of MFCs is important considering the application of this system. Figure 2.6.2.1 shows the two-chamber and single-chamber structures of the MFCs.

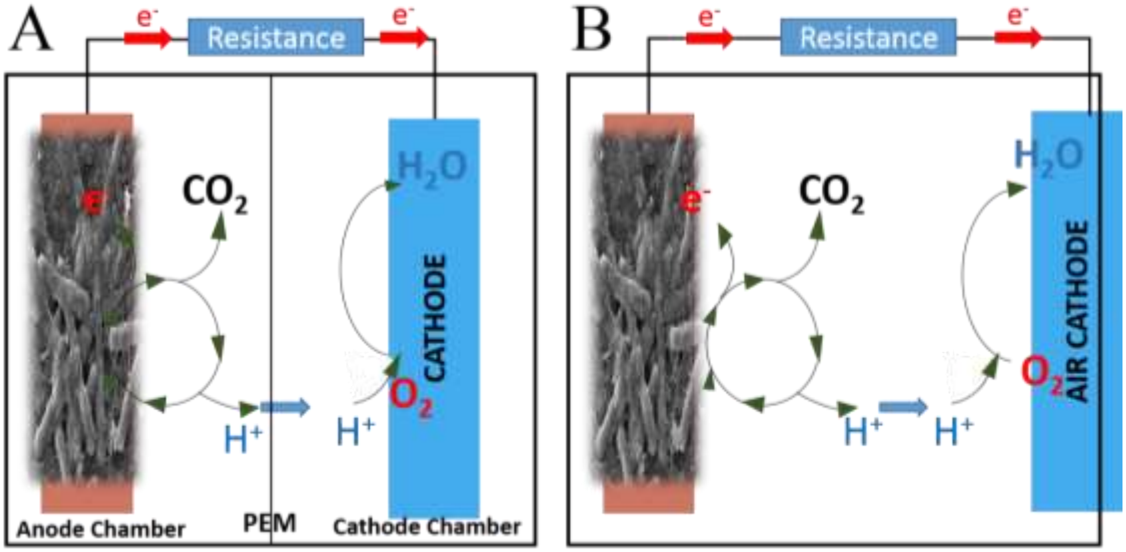

Figure 1.2.4.2.1. MFC configurations: A) two-chamber and B) single-chamber MFC structures: A) two-chamber and B) single-chamber.

1.2.4.3 Anode electrode and anodic biofilm behavior

As an essential compartment, the anode electrodes have a significant effect on MFC's power density. The composition, morphology, and surface characteristics of the anode constituents affect the MFC's overall performance, bacterial adhesion, electron transfer, and substrate oxidation. By increasing the anode active sites and improving electron transfer between the anode and the bacteria, activation losses can be minimized.

As mentioned above, electron transfer from microorganisms to the anode occurs either directly or through intermediates. In the direct method, the electron is transferred through direct contact with the cytochromes of the microorganism's outer membrane. Electron transfer can also take place using nanowires, which are produced by microorganisms themselves. Nanowires are electrically conductive bridges by which electrons can be transferred from the surface of microorganisms to the anode electrode's surface. Researchers have been able to detect and prove the presence of nanowires in *Shewanella* and *Geobacter* [41].

The outer layer of some groups of microorganisms is formed from lipid membrane, peptidoglycan, and non-conducting lipopolysaccharide, which all prevent the direct transfer of electrons to the surface of the anode electrode. For this reason, electron transfer mediators in the oxidized state are used to capture electrons from the cell membrane of a reduced microorganism. Then, they pass through the membrane and deliver the electrons to the anode and re-oxidize the organism. This process increases the electron transfer and ultimately improves the power obtained from the system. Electron transfer mediators must easily pass through the cell membrane and easily receive electrons from electron carriers in the electron transfer chain. Also, they should have high solubility in the anolyte and react quickly with the electrode [42, 43].

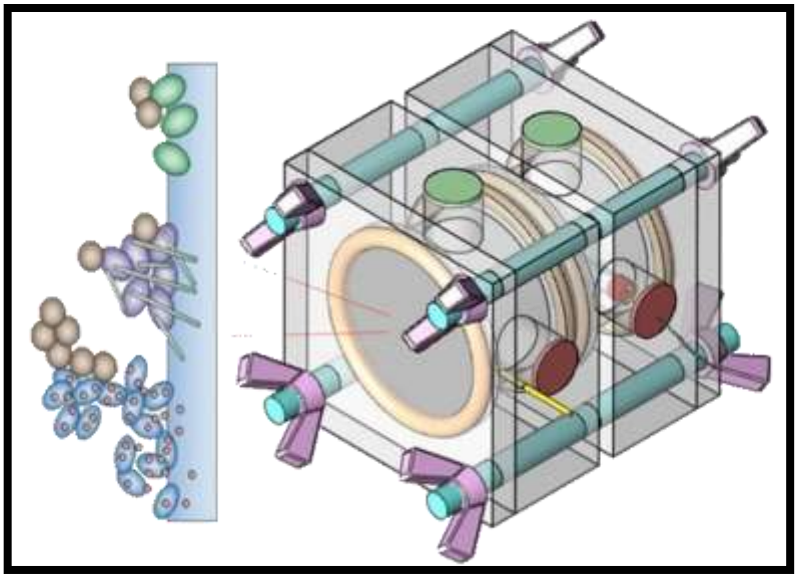

Figure 1.2.4.3.1. Mechanisms of electron transfer by microorganisms: electron transfer through direct contact (green), electron transfer through nanowire (purple), electron transfer by mediators produced by microorganism (blue) and electron transfer through artificial mediators (brown)

On the other hand, the cost of using these materials should be considered. Since most microbial cells are electrochemically inactive, mediators such as humic acid, tionine, and methyl blue are utilized as electron transfer mediators. Different mechanisms of electron transfer from bacteria to the anode are shown in Figure 2.6.3.1.

1.2.4.4 Cathode electrodes of microbial fuel cells and oxygen reduction reaction

As mentioned, in an MFC, electrons reach the surface of the cathode electrode through an external circuit, and protons pass through a separator or membrane, and then the reaction of the cathode part is completed in the presence of an electron acceptor. Among chemical reactions at the cathode side, the oxygen reduction reaction has been of the most importance. The low rate of this reaction in chemical and bioelectrochemical fuel cells is known as one of the main barriers to performance enhancement. Although the current and power output densities of MFCs are still two to three orders of magnitude lower than those of conventional fuel cells, reduction kinetics of oxygen as the main electron acceptor in these systems can play a significant role in their development [44]. Because of mixed potentials in real conditions and thermodynamic limitations, ORR's redox potential in MFC is much lower than the theoretical value (around 0.5 V) [45]. Unmodified metal and carbon cathodes usually perform poorly in ORR, and the current densities obtained by them in MFCs are very low.

Oxygen reduction reaction occurs by two paths in MFCs: through the four-electron path by converting O_2 to H_2O, and the other, through the two-electron path with forming H_2O_2 from O_2 reduction [46]. A Four-electron pathway is preferred in MFC. The two-electron pathway is an imperfect oxygen reduction reaction that leads to low energy conversion efficiency and the formation of intermediates and free radicals that can be destructive. When carbon electrodes are used as cathodes in MFCs, two consecutive electron reduction reactions are performed to form H_2O_2. In general, the oxygen reduction mechanism depends on several parameters such as the nature of the electrode material, pH, and current density [47]. ORR rate faces three main limiting steps consisting of O_2 adsorption on cathode active sites, dissociation of O_2 bond, and electron transfer.

To improve ORR in fuel cells, different types of catalysts are used. Platinum group, non-platinum group, and non-metal group. Platinum and platinum-based materials are the most widely used catalysts in MFCs. Platinum is considered as the standard material in fuel cells and MFCs. The reduction of oxygen on the platinum surface is accomplished by a direct four-electron transfer process in acidic and alkaline solution electrolytes. Despite platinum's good performance as a catalyst in ORR, its high price makes it difficult to be utilized in the MFCs. Many research has been conducted on the development of alternative cathodes for noble metal catalysts. Other metal cathodes such as gold, rhodium, nickel, copper, stainless steel, etc., can also reduce O_2. However, these materials have less catalytic activity than platinum. The ORR on the surface of electrodes other than platinum is associated with greater over-potential and consequently lower current density. Additionally, non-platinum metal cathodes are electrochemically oxidized more easily and rapidly than platinum due to their higher reactivity in potential of oxygen reduction. This oxidation also reduces their continuous performance and catalytic properties, causing the cell to decline faster [48].

One possible solution to decrease the cost of cathodes for ORR is to reduce the platinum mass loading by mixing different catalysts like metal oxides and carbon materials to the platinum group. However, in MFC case in which the electrolytes are usually not sterile and contain biological substances, both platinum and metal oxides may be irreversibly poisoned. Hence, carbon materials are also utilized as catalysts in ORR at MFCs. The electro-catalytic activity of carbonaceous substances in ORR is attributed to quinone groups and, as previously mentioned, involves adsorption, decomposition, and electron transfer at the active surface. The mechanism of ORR and the catalytic activity of carbonaceous materials vary according to the type of carbon. For glassy carbon and pyrolytic graphite, ORR is carried out through two-electron pathways, and H_2O_2 is produced, while in the case of oxidized graphite and oxidized glassy carbon, H_2O_2 is reduced to H_2O. Carbon nanotubes have presented acceptable stability and excellent electro-catalytic activity to reduce oxygen in alkaline solutions. The proposed ORR mechanism on the CNT surface is similar to quinone’s. The reaction is done based on the mechanism of formation of peroxide, either HO_2^- or a combination of both HO_2^- and OH^-, depending on the CNT preparation method and the CNT modified electrode's potential [49, 36].

1.2.4.5 Membrane in microbial fuel cells

The membrane in an MFC system is utilized to separate anode and cathode chambers and perform as a barrier against oxygen transfer to the anode chamber. It can also transfer ions selectively between the anode and cathode chambers. An ideal membrane should have high ionic conductivity, electron insulation, proton conductivity, durability, chemical stability, biocompatibility, non-clogging, and biofilm formation and have a reasonable price. Choosing the right membrane depends on several important factors. If the anode operates anaerobically, oxygen delivery to the anode chamber should be minimized or generally restricted. This factor is difficult to control; because most membranes are active in perfectly humid conditions, oxygen can be released by the water in the membrane. Despite the benefits of membrane use mentioned, membranes provide relatively high electrical resistance in MFCs. Therefore, the researchers proposed an architecture consisting of a membrane and an electrode called a membrane electrode assembly as a suitable solution to reduce the internal resistance of the MFC [50].

1.2.4.6 Membrane electrode assembly

Membrane electrode assemblies (MEAs) are a set of membranes and electrodes in which the electrode and membrane are connected directly to each other. This structure minimizes the distance between the electrodes and thus the ohmic resistance. In MFCs, it is common to use a membrane electrode in which only the cathode is attached to the membrane, and the anode is located away from the membrane (Figure 1.2.4.6.1). In contrast, the anode is placed on the surface of the membrane, placing it in direct contact with diffused oxygen and affecting the anode biofilm's activity. Besides, the possibility of microbial biofilm formation on the membrane surface increases, which negatively affects cell performance. Membrane cathodes are bonds between an ion exchange membrane and a catalyst layer that include an electron conductor, a catalyst for an oxygen reduction reaction, and a binder or binding agent. The catalyst may be on the surface of an electrically conductive material, which itself can be a high-specific carbon material. The bonding agent can be an inert polymeric material such as PTFE, PVDF, or ion exchange materials such as Nafion [51-53].

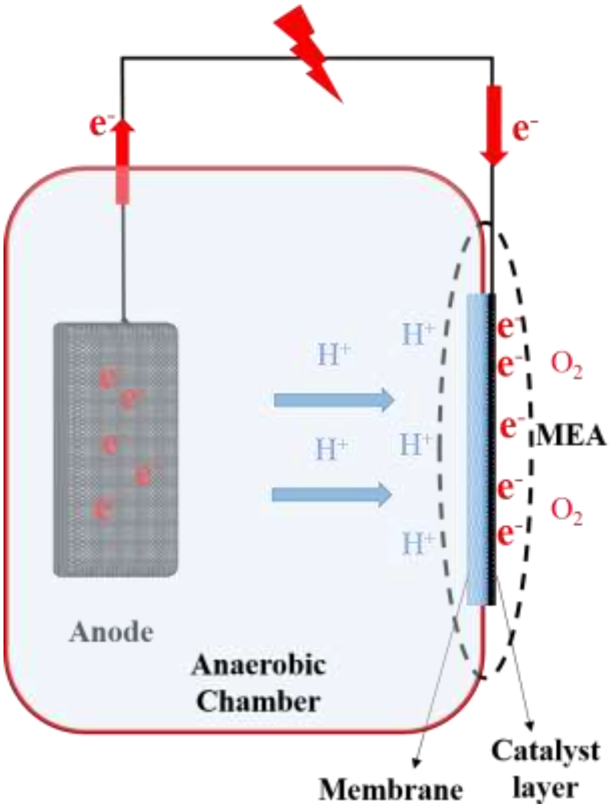

Figure 1.2.4.6.1. A single chamber MFC with using membrane electrode assembly air-cathode

In single-chamber MFCs (SCMFCs), the air-breathing cathode prevents anolyte leakage and provides ORR sites [54]. As mentioned in the literature, many materials and structures are employed in the cathode fabrication process [55]. Typical air-breathing cathodes feature a membrane electrode assembly (MEA) design. MEA key components are: i) the conductive substrate where the electrocatalytic reduction of O_2 takes place, and ii) the hydrophobic layer. Carbon paper and carbon cloth are introduced as commercial conductive substrates coated by a mixture of Vulcan XC-72R carbon and poly-tetra fluoro ethylene (PTFE) to build gas diffusion electrodes (GDE) air-cathodes [56]. These air-cathodes are commercially available and are applied in various types of fuel cells. PTFE is used to bind the carbon mixture to the substrate. Furthermore, it is used to make the GDE surface hydrophobic, and hence, to prevent leakage [57].

In addition to conductive substrates, non-electrical conductive ones are also used to fabricate MEA air cathodes. A variety of ultrafiltration membranes, proton, cation, and anion exchange membranes, can be used as MEA substrates. MEA’s substrate plays a vital role as a barrier to anolyte leakage and affects proton or cation exchange, which is required for MFC operation[58, 59]. For example, commercial Nafion proton exchange membranes coated with carbon-catalyst mixtures are used as MEA in PEMFCs and have also be implemented in MFCs [60]. Besides the high price of materials, the fabrication process of these electrodes is expensive [51]. PTFE binder, Nafion membrane, and its complex synthesis and treatment and also high-temperature process altogether increase the final cost of produced electricity by MFC in competition with other electrical power sources [61]. Hence, scientists are making an effort to find low-cost air cathodes based on cheap materials and obtained by environmentally friendly processes to make MFC technology more practical.

Cellulose has caught the eye of scientists because it is the most widely available biopolymer in the world [62, 63]. Ci et al. extracted nano-cellulose fibers from corn, treated and modified the nanofibers' surface, and then used them to fabricate a gas diffusion layer (GDL) without PTFE for the carbon cloth electrode. This air cathode showed better performance than the commercial electrode featuring a PTFE-based GDL [57]. Among cellulose and its derivatives, bacterial cellulose (BC) has received extensive attention due to its three-dimensional porous nano-structural network, high purity, flexibility, high mechanical strength, and excellent tear resistance in aquatic environments [64-66]. These novel features, as the heritage of *Acetobacter,* make BC an excellent green substrate for electrode fabrication in MFCs and energy storage devices[67, 68]. Mashkour et al. used polyaniline, and polypyrrole coated BC as cheap bio-anodes in an H-type MFC, giving a much higher power density response than graphite [28, 29]. Also, Mashkour et al. fabricated flexible conductive paper based on BC with CNT and Gum Arabic binder by a drop-casting method. They could reach a low sheet resistance of 1 Ω.cm evaluated by the 4-probe method [69]. In recent years, great interest has been seen in exploiting BC in biofuel cells (BFCs). Lv et al. in 2016 and Li et al. in 2020 prepared a BC-CNT composite by vacuum filter method, immobilized enzymes on BC-CNT, and used it as anode and cathode in an enzymatic BFC [70, 71]. Moreover, a BC based proton exchange membrane (PEM) was fabricated by Vilela et al. with poly sulfonic acid treatment and used it in a SCMFC with a micro porous layer (MPL)-carbon cloth air-cathode. The internal resistance of the MFC was high and the open circuit voltage (OCV) of the cell was low due to the lack of proper BC's connection to the carbon cloth cathode [72].

1.3 Application of supercapacitors in microbial fuel cells

Supercapacitors (SCs), for storing and delivering energy at high densities of current and power, are known as one of the most significant energy storage devices. Also, they feature an extremely long cycle-life: they can be charged/discharged millions of times. In addition, SCs, unlike conventional batteries, can store energy at any voltage, which is limited only by the electrolyte electrochemical stability. For this reason, they are more consistent with the dynamic behavior of bio-electrochemical cells. Using external SCs for storing electricity generated by MFCs has been previously studied by the scientist. They collect low-produced MFC power and then supply the electricity required for low-consumption electronic devices. Besides, it has been shown that in MFC, higher electricity is harvested through periodic rather than continuous MFC operation. Hence, another solution to enhancing MFC's efficiency is using the intrinsic capacitive properties of the MFC electrodes. Both MFCs and SCs use high surface carbon as their main electrode component. Efforts have recently been made to combine capacitive materials with MFC electrodes in order to boost power efficiency and storage of charge. The creation of the Helmholtz layer by electrolyte ion adsorption in the MFC/electrode interfaces results in the apparent cell capacitance [73, 74].

1.3.1 Using external capacitors and supercapacitors for MFC generated electricity improvement

Based on MFC behavior, higher performance in periodic compared to continuous discharging, many researchers have taken advantage of charging capacitors and supercapacitors after several times of MFC discharge and then discharging the filled capacitors. A capacitor, composed of two terminals that are separated with dielectric materials, can store energy. By connecting a capacitor to an MFC, the capacitor is filled by the MFC’s generated charge. In fact, the capacitor functions as a consumer with differing resistance based on the MFC discharging current and the capacitor voltage to be filled [75]. At below, some of the reported works are reviewed:

Dewan et al., in 2009, used a dual-chamber MFC with graphite plate as anode and platinum mesh coated with carbon-manganese oxide as the cathode to achieve a 700 mV OCV. They compared the performance of the MFC-connected capacitor with that of the individual MFC for power generation. They used an ultra-capacitor of 10 F (maximum charging potential of 2.5V). Due to the MFC's low working potential (nearly 0.5 V), the capacitor could not be fully filled. In order to charge the capacitor, the positive and negative terminals of the capacitor were connected to the cathode and the anode of the MFC. Various MFC voltages were used to charge the capacitor. Optimum charging process, depending on the amount of charge stored in the capacitor, the duration of the charging time, and the output power was achieved at a potential of approximately 0.35 V. The maximum power generated by the MFC with the capacitor was more than two times higher than the individual MFC. This work has also shown that the MFC and DC power supply have different behavior when charging the capacitor due to the MFC's charging voltage during the charging phase. Hence, using MFC as a power supply for charging capacitors has a complicated mechanism and relies on the optimized voltage to achieve the full stored charge. Continuous energy harvesting from individual MFCs leads to a high voltage drop and thus reduces the charge received by the MFCs, while using a capacitor as well as several short-term discharging steps with rest time intervals increases the charge and power produced by MFCs [76].

In addition to conventional capacitors, supercapacitors are also coupled externally to MFCs. Poli et al., in a recent study, used three different SCs (1F, 3F, and 6F) to enhance energy harvesting from a single chamber MFC. In this work, they prepared an SCMFC with carbon brush anode and activated carbon-stainless steel air-cathode (OCV of 570 mV) and a working volume of 100 ml. At first, maximum power of 0.56 mW at 2 mA was obtained from the individual cell. Complete discharging of the cell by a discharging current of 2 mA took about 450 s while, by connecting SCs of 1F, 3F, and 6 F, it took a bit more than 450 s, more than 1100 s, and about 1900 s, respectively. In this work, the maximum discharging current was shown 4 mA with high cell resistance. On the contrary, using SCs, the MFC-SC was discharged by much more current of 100 mA. Therefore, using SCs resulted in a much lower resistance of the combined system than the individual MFC. Moreover, pulse power output (mW) of MFC-SC with 10 s pulses showed the value of around 5, 12, and 25 by SCs of 1F, 3F, and 6F, respectively, which were much higher than that obtained by the MFC (about 1 mW) [77].

1.3.2 Improving internal supercapacitive features of microbial fuel cells

MFCs' electrodes placed in two different aerobic and anaerobic environments become polarized without any external source and make an OCV under 1 V under thermodynamics limitations in a single cell. Accordingly, MFCs can be considered as asymmetric and self-rechargeable electrochemical double-layer supercapacitors.

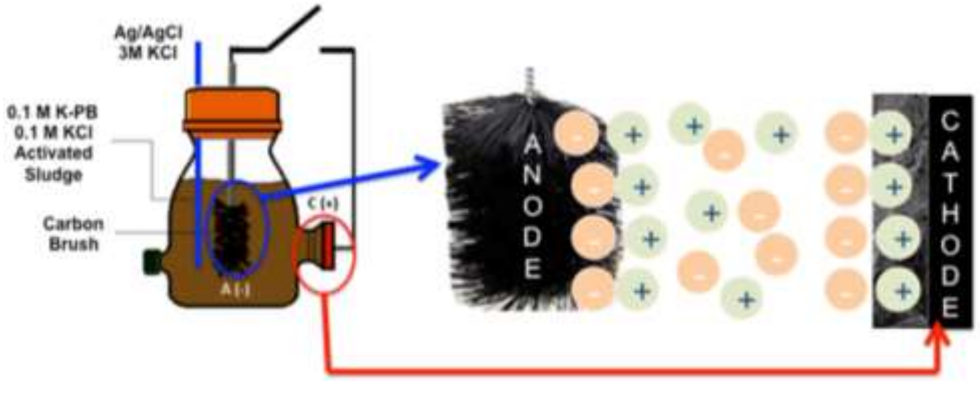

Figure 1.3.2.1. Concept of double-layer capacitance in MFC. Reprinted from ref. [78], with permission from Elsevier.

This hybridization of the two concepts of MFC and supercapacitor has opened a new window to researchers in these fields. This hybridization serves to integrate the internal supercapacitive properties of the MFC to maximize its output power and energy [79]. To this end, the modification of MFC electrodes with super-capacitive materials is of considerable significance.

For the first time, Deeke et al., in 2011, introduced MFC as a storage device of renewable energy by studying the capacitive response of the anode electrode. They used a dual-chamber MFC with graphite plate cathode in diluted ferricyanide catholyte. Bare and activated carbon-PVDF modified graphite were utilized as non capacitive and capacitive anode electrodes. The first concept of charging/discharging in MFC was performed by anode voltage controlling on -0.3 V (for discharging) and then leaving the system on OCV (for self-charging). In this way, the two anodes' voltage and current behaviors were studied respectively in charging and discharging periods.

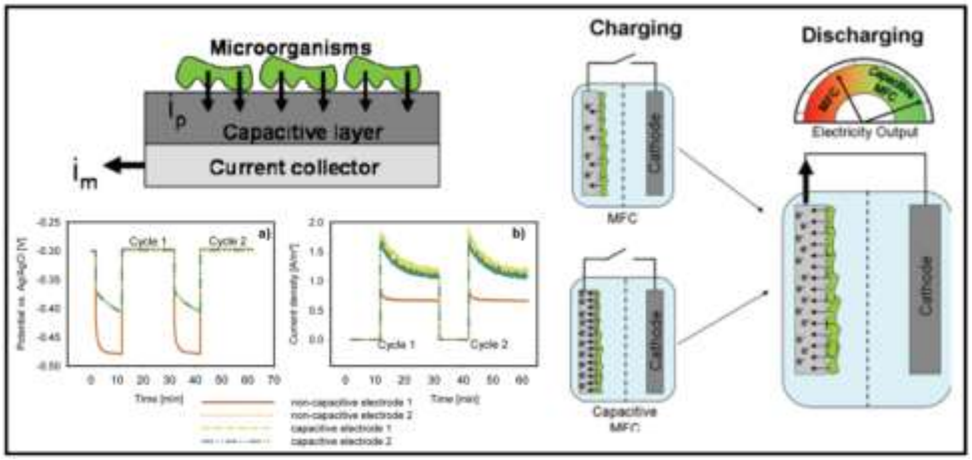

Figure 1.3.2.2. MFC electrochemical behavior in the presence of capacitive and non-capacitive anodes. Reprinted from ref. [80], with permission from the American Chemical Society.

They showed that increasing discharging time improved the charge storage of the anode. Also, it was revealed that the anode discharging process took longer than its charging duration. Different charge/discharge periods indicated that the measured charge was higher than expected for the capacitive electrode, while for the non-capacitive anode, it was lower. The higher performance of the capacitive anode was attributed to the kind of binder

(PVDF), activated carbon, and the thickness of the coated layer[80]. In 2013, the same research team found that the specific surface area of coating and the surface roughness increased by decreasing the capacitive layer's thickness, and thereby, thin coated anode outperformed the thicker ones [81].

Malvankar et al., as the first research group, introduced capacitance of anodic microbial biofilm. A dual-chamber MFC, with two pairs of gold anodes and a cathode, was used in that work. Each pair of anodes were fixed on a non-conductive substrate by a 50 μm gap. One pair was colonized, and the other pair was used as control. Electrochemical Impedance Spectroscopy revealed that the colonized anode active biofilm's capacitance had an increasing trend and showed a higher value than the almost constant capacitance of the control anode during 50 days. Also, by comparing four kinds of active biofilms having different amounts of cytochrome hemes, they found the biofilm with a higher content of cytochrome had higher capacitance. Therefore, C-type cytochromes have the capability of charge storage in biofilm. On the other hand, biofilm without cytochrome does not increase electrode capacitance and even presents worse performance than a non-colonized anode. The research also showed that an active biofilm is electrically conductive as it could make a conductive bypass over the non-conductive interval between the pair of anodes [82].

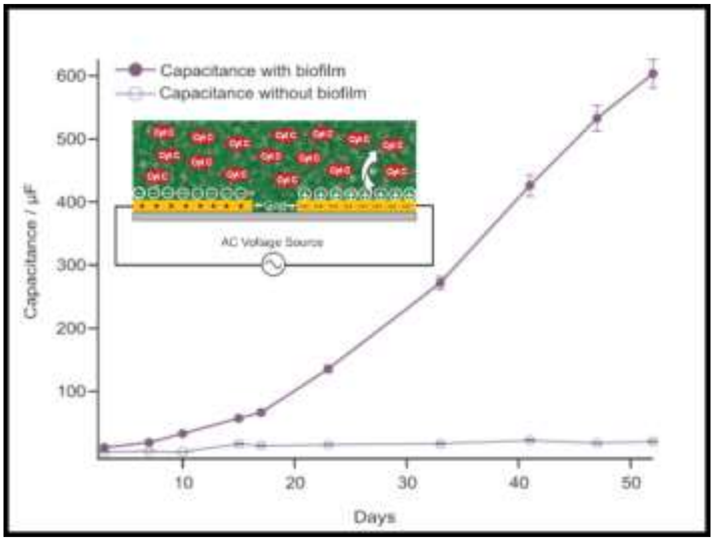

Figure 1.3.2.3. Effect of biofilm formation on the capacitance of the capacitive anode. Reprinted from ref. [82], with permission from Wiley.

Agnes et al. in 2013 studied the effect of carbon nanotubes and enzymes on the supercapacitive behavior of biological fuel cells. They suggested a hybrid device in which CNTs performed as supercapacitor electrodes and glucose oxidase for producing electrons. In this study, galvanostatic discharging pulses of 3 mA for 10 ms were applied for the BFC supercapacitive performance evaluation. It was shown that the system could recover its capacitance in a short time (10 s) after each discharging pulse, and the cell with continuous glucose feeding demonstrated excellent performance with low voltage drop even after 40000 cycles. The system's high performance may be attributed to the high enzyme activity in oxidizing glucose and high capacitance of the CNTs. As both glucose and oxygen exist in human blood, the system can be considered an implantable power supply [83].

Santoro et al., in 2015, presented a new concept of supercapacitive MFC design. They took advantage of two strategies to enhance MFC performance: AC-based air-cathode modification with iron-aminoantipyrine (Fe-AAPyr) and bilirubin oxidase (BOx) and also using an additional capacitive carbon-brush electrode (AdE) short-circuited to the air-cathodes. Electrode modification with Fe-AAPyr and BOx increased cathode potential (vs. Ag/AgCl) to 175 and 315 mV compared to 105 mV for bare AC cathode. However, the modification could not considerably decrease the ohmic drop of cathode voltage occurred by galvanostatic discharge (344, 339, and 299 mV for bare, Fe-AAPryr, and BOx modified). By short-circuiting the AdE, the cathodes' capacitive response increased significantly, and the ohmic drop for the cathodes-AdE decreased to a very low value (41, 36, and 36 mV). In this work, galvanostatic discharging was utilized to measure power density which was the first use of this method for MFC calculations. In this approach, two parameters of discharging pulse current and pulse time were found very effective on the MFC power output. MFC with BOx-modified cathode-AdE produced the highest power, more than three times higher than the system with bare cathode-AdE. Moreover, the supercapacitive MFC showed self-charging in 20 s after each 2 s pulse of 6 mA. Mixed-use of high voltage cathodes and also AdE for the first time enhanced internal supercapacitive feature of the MFC EDLC based supercapacitor [73].

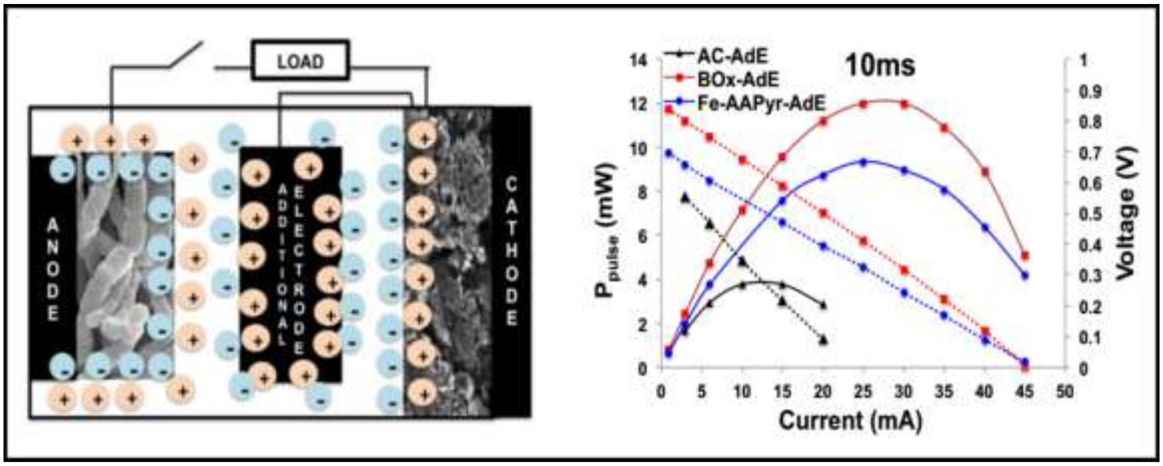

Figure 1.3.2.4. Effect of the double-layer capacitance of an additional cathode and different cathode modifiers on the MFC performance. Reprinted from ref. [73], with permission from Elsevier.

1.4 Aim of the thesis

The aim of this Ph.D. thesis is to develop the concept of super-capacitive MFCs by fabricating low-cost cellulosic nano-composites with high capacitance in order to increase cellulose-based MFCs performance. Specifically, a novel design of monolithic MEA (based on BC and CNTs) and also an innovative study of the cellulosic anode and cathode capacitance in super-capacitive MFCs have been presented in detail.

For the first time, BC has been modified by Nano Zycosil (a cheap organosilane) to make a hydrophobic surface for BC. By this approach, high-cost hydrophobic agents like PTFE used in commercial air-breathing cathodes are replaced with low-cost materials. Thus, MFC fabrication cost decreases by introducing the new organosilane.

Impedance spectroscopy, cyclic voltammetry, and galvanostatic discharging have been proposed to study the capacitive properties of the MEA

A new design of a quadruple MFC made by four single-chamber MFCs has been introduced.

Electro-polymerization of PANI on BC-CNT has been performed by a fast and chemical initiator-less pulse chronopotentiometry. Thus, a binder-less CNT coating and initiator-less PANI coating have been suggested for making anode electrodes.

Studying the capacitance of BC-based bioanodes modified with super-capacitive CNTs and PANI has been performed in detail by Electrochemical Impedance Spectroscopy (EIS).

The concept of additional capacitive bio-anode has been proposed in this thesis, and its effect on MFC performance has been studied by the galvanostatic discharging method.

Chapter 2

Experimental sections

Chapter 2 addresses materials and methods utilized in this thesis, including chemicals, electrolytes in the MFC, electrode fabrication methods, MFC configuration and incubation, and all physical, chemical, and electrochemical characterization methods.

Elsevier is acknowledged for the permission to reprint some parts of the following publications:

- M Mashkour, M Rahimnejad, M Mashkour, F Soavi, Increasing bioelectricity generation in microbial fuel cells by a high-performance cellulose-based membrane electrode assembly. Applied Energy, 282 (2021), 116150. Copyright (2021).

- M Mashkour, M Rahimnejad, M Mashkour, F Soavi, Electro-polymerized Polyaniline Modified Conductive Bacterial Cellulose Anode for Supercapacitive Microbial Fuel Cells and Studying the Role of Anodic Biofilm in the Capacitive Behavior, Journal of Power Sources 478 (2020), 228822. Copyright (2020).

2.1. Chemicals

Table 2.1.1 demonstrates all chemicals used in this study:

Table 2.1.1. List of chemicals utilized in this thesis with their specifications

No.	Chemicals	Purity	Company	Country
1	Hydrochloric acid	37%	Merck	Germany
2	Activated carbon	-	Honey Well	Germany
3	carbon black	-	-	-
4	polytetrafluoroethylene	60%	DuPont	USA
5	Ethanol	99%	Merck	Germany
6	Carbon nanotubes (MW)	95%	Neutrino Noavarane Nano	Iran
7	sodium dodecyl sulfate	-	Alderich	USA
8	Nano zycosil	98%	Zydex Industries,	India
9	Aniline	99%	Merck	Germany
10	Di-potassium hydrogen phosphate	Analytical grade	Merck	Germany
11	Potassium di-hydrogen phosphate	Analytical grade	Merck	Germany
12	Potassium acetate	Analytical grade	Merck	Germany

2.2. Electrode fabrication

2.2.1. Air-cathode fabrication

Two types of air-cathode were fabricated in this work, including stainless steel (SS) mesh based and BC-based electrode:

2.2.1.1. SS mesh based cathode fabrication process

Activated carbon powder, superconducting carbon black powder, and polytetrafluoroethylene (PTFE) binder were mixed together in a mass ratio of 10:30:60. During mixing, isopropyl alcohol was slowly added to the carbon mixture to form a paste. The pasty ball was then spread on a clean glass surface which was previously washed with water and ethanol. Then, the dough with dimensions of 2.5×2.5 cm^2 and a thickness of 0.2 mm was placed on the surface of a stainless steel mesh with a thickness of 0.3 mm and was prepared for pressing. A hydraulic press machine (at LEME, UNIBO) was used for pressing carbon paste on a steel mesh surface. After pressing, the electrode was placed in the oven at 60 ° C for 3 hours to remove excess alcohol. The final dimensions of the electrode were 2.5 by 2.5 cm^2 and the surface density of the carbon layer on the surface of stainless steel mesh was approximately equal to 28 mg /cm^2. The resulting electrode can be seen in Figure 2.2.1.1.1.

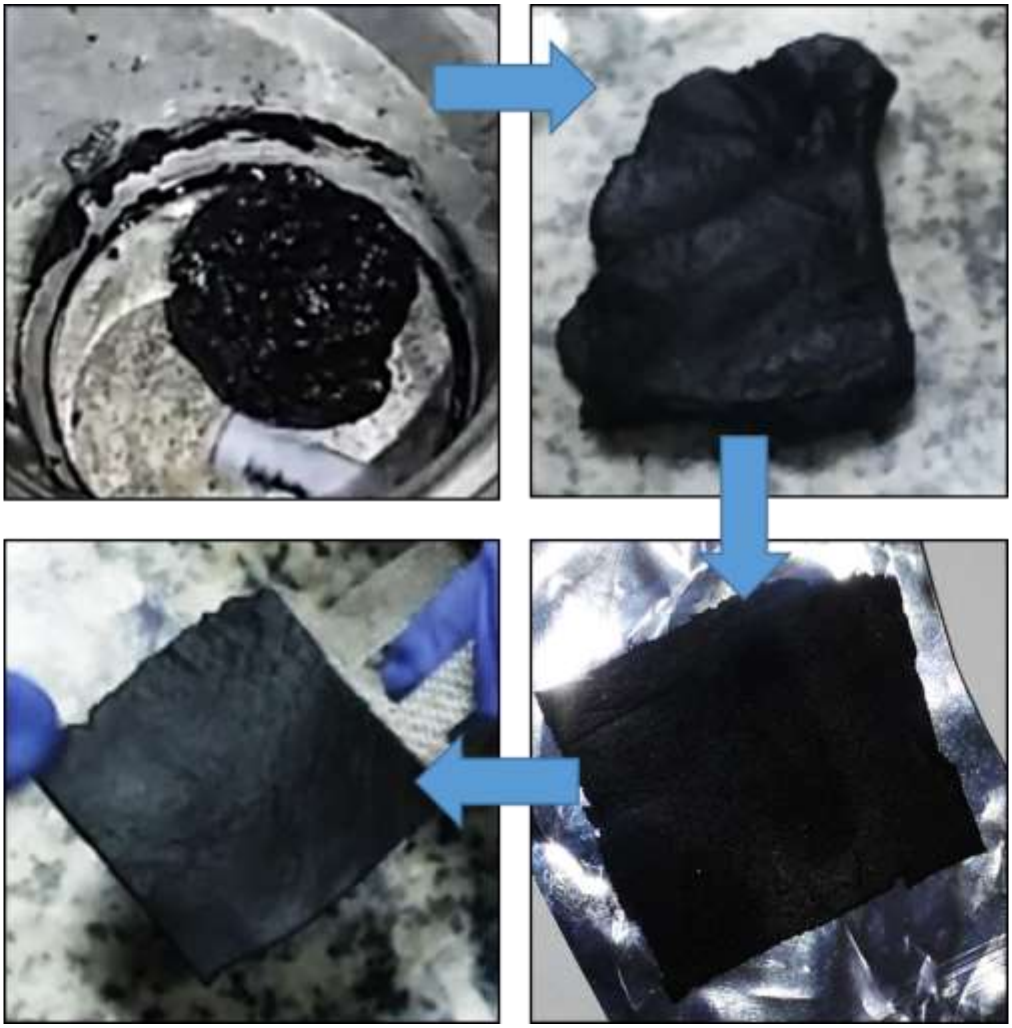

Figure 2.2.1.1.1. The fabrication process of SS mesh air-cathode

2.2.1.2. Bacterial cellulose-based membrane electrode assembly fabrication process

As shown in Figure 2.2.1.2.1, a solution containing 10 mg of CNT and 25 mg of sodium dodecyl sulfate was mixed with 25 mL of Milli-Q water under 15 min ultrasound to achieve a homogeneous solution of CNT. The solution was then poured onto the BC membrane

(Nano-Novin Polymer, Iran) to cover BC by Buchner's vacuum force [70]. The CNT-coated BC was then put at ambient temperature for complete drying.

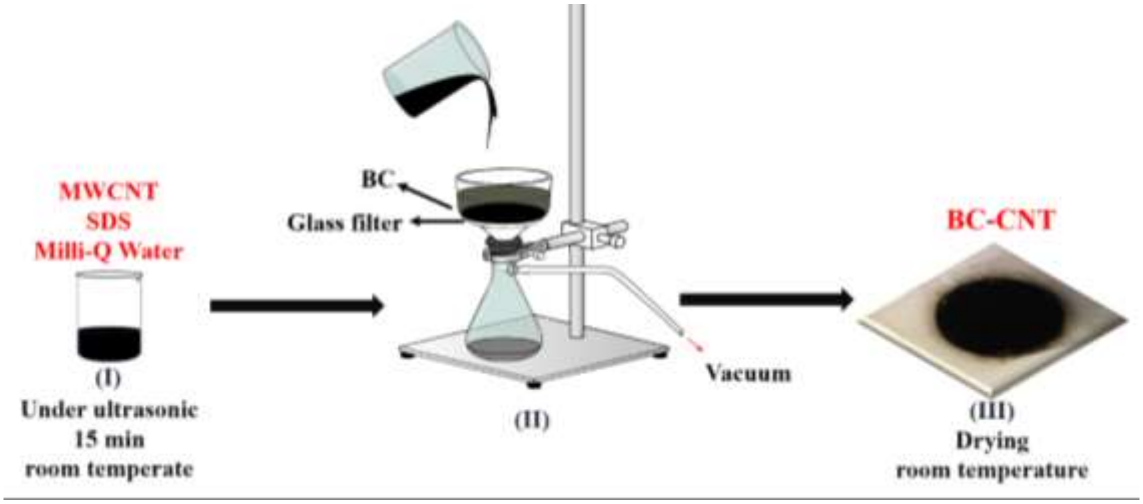

Figure 2.2.1.2.1. The procedure of CNT coating on BC membrane

The uncoated side of CNT coated BC was covered by NZ-water solution (1:5, v/v) as a hydrophobic agent with a painting brush and left to dry overnight to yield the hydrophobic BC-CNT-NZ.

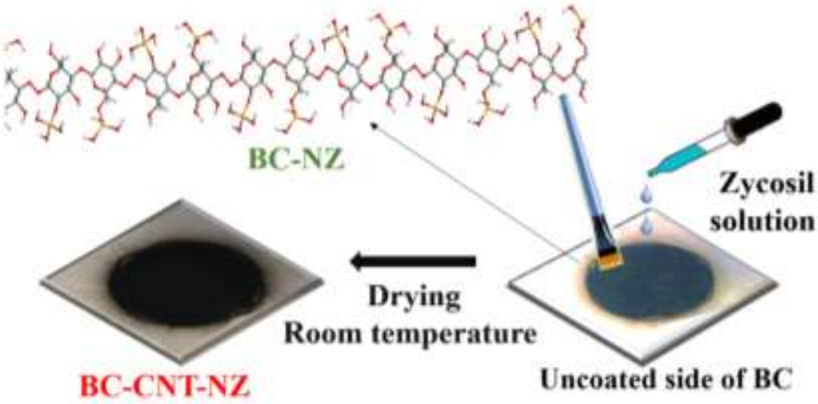

Figure 2.2.1.2.2. The procedure of NZ coating on BC membrane

2.2.2. Anode fabrication

At first, 10 mg of CNTs were mixed with sodium dodecyl sulfate in 25 ml of Milli-Q water under ultrasound (15 min) to form a homogeneous suspension. Afterward, a sheet of wet BC (Nano Novin Polymer, Iran) with a thickness of 2 mm was placed on the glass filter of an Erlen Bochner flask. CNT coating on BC was carried out by vacuum filtering. Then it was left at ambient temperature for complete drying. The BC-CNT membrane was fixed at the bottom of a handmade electrochemical three electrodes cell (with a capacity of 12 ml) shown in Figure 2.2.2.1. The BC-CNT, spiral-shaped titanium mesh (with an extra surface), and silver wire were placed respectively as working, counter, and reference electrodes in the cell (Fig.1 A). Because of BC's hydrophilic nature, a Mylar sheet was placed under the BC-CNT substrate to prevent the solution leaking from the cell. The CNT-coated surface was exposed to the monomer solution (230 μl of aniline in 10 ml of 1M HCl).

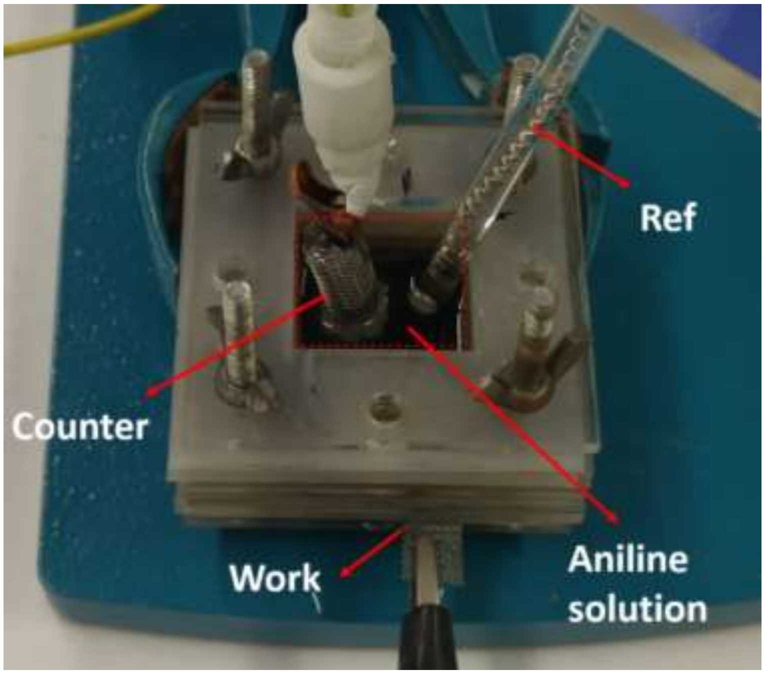

Figure 2.2.2.1. Electrochemical three-electrode cell for electro-polymerization of aniline on BC-CNT

Electro-polymerization of aniline on BC-CNT was performed in two steps; at first, pulse chronopotentiometry technique (20 pulses, for each one 2 mA/cm^2 during 50 s and -2 mA/cm^2 during 50 s) was carried out. Then chronopotentiometry for 1000 s with a current density of 2 mA/cm^2 (per BC-CNT surface) was exploited by a Volta Lab potentiostat. The electrochemical process is visible in Figure 2.2.2.2. After electro-polymerization, a green layer of emeraldine was formed on BC-CNT. The film was washed several times with

Milli-Q water to separate unreacted monomers and increase the pH of BC-CNT-PANI to neutral. Then it was dried under ambient temperature.

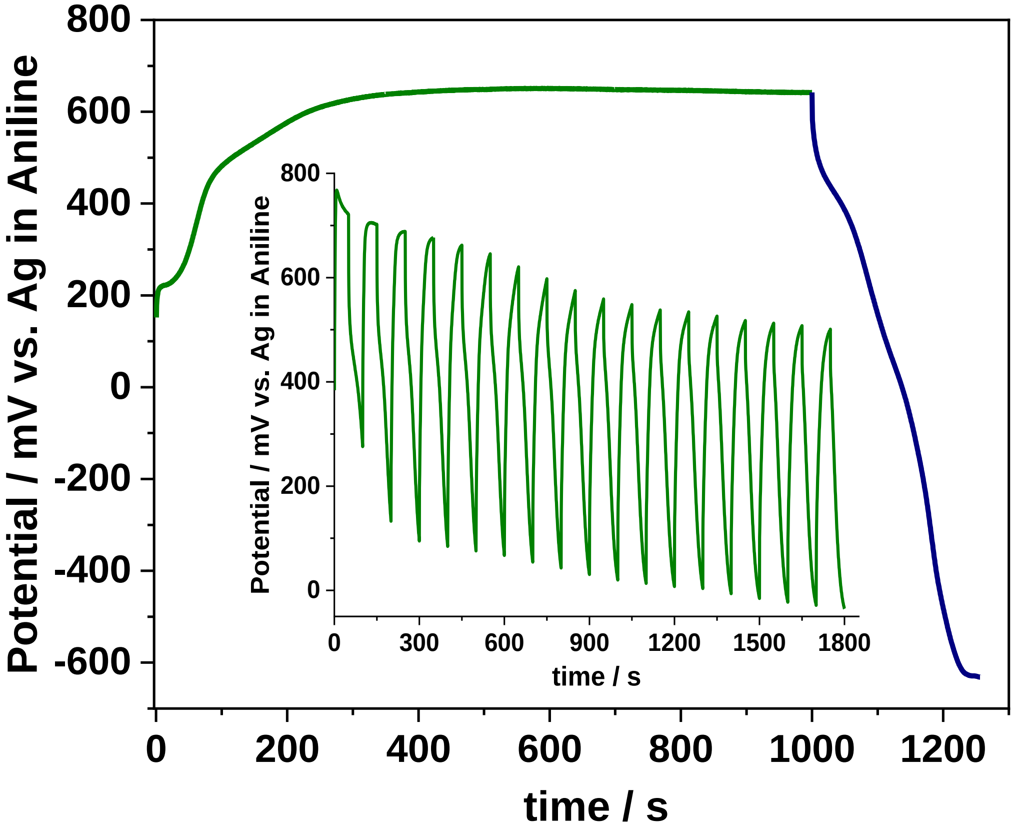

Figure 2.2.2.2. Chronopotentiometry techniques for electro-polymerization of aniline on BC-CNT

Finally, BC-CNT and PANI coated BC-CNT were provided as the cellulosic anode. For the anodes, both coated BC sheets were separately placed on an SS current collector of the same size and then pressed well between two plastic meshes to have a good connection with SS. The assembled anode is shown in Figure 2.2.2.3.

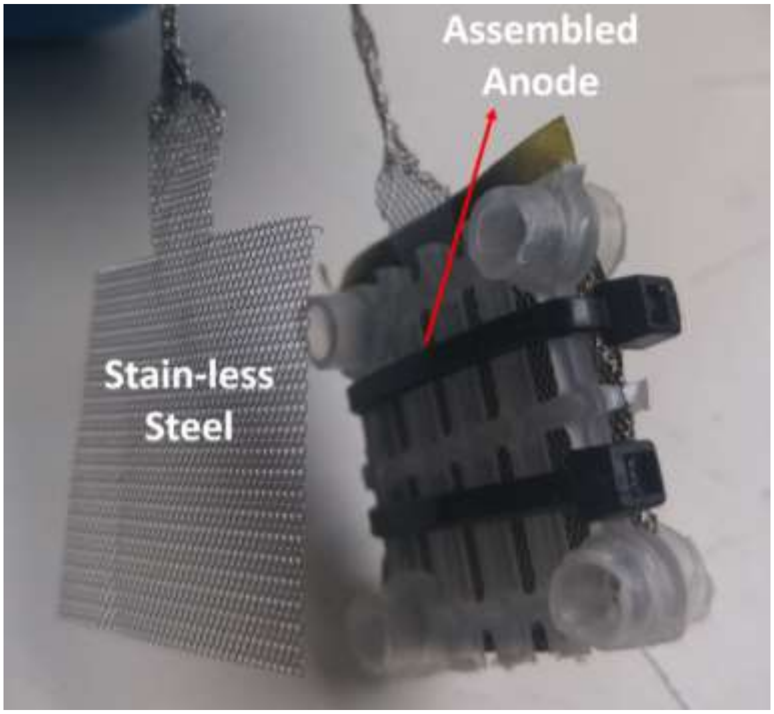

Figure 2.2.2.3. Assembled anode electrode by conductive BC and SS mesh current collector

2.3. Microbial fuel cell configuration

A quadruple MFC constructed by four single-chamber MFCs and a middle chamber was used in this study. It should be noted that each SCMFC is cubic, made by Plexiglas and is able to have a maximum of four electrodes (2.5 cm × 2.5 cm) on its four sides. The working volume of each chamber is 250 ml. Also, there are several holes for reference electrodes, purging required gases like nitrogen and oxygen, and also for feeding. There is a big hole on the top of each chamber for anodes, which is isolated from the air by a silicon cap. Each air-cathode is fixed to the chamber body by two silicon gaskets, a Plexiglas frame, and eight SS screws. The MFC configuration is demonstrated in Figure 2.3.1. Anode-cathode connection modes in this thesis are shown in Table 4.3.1.

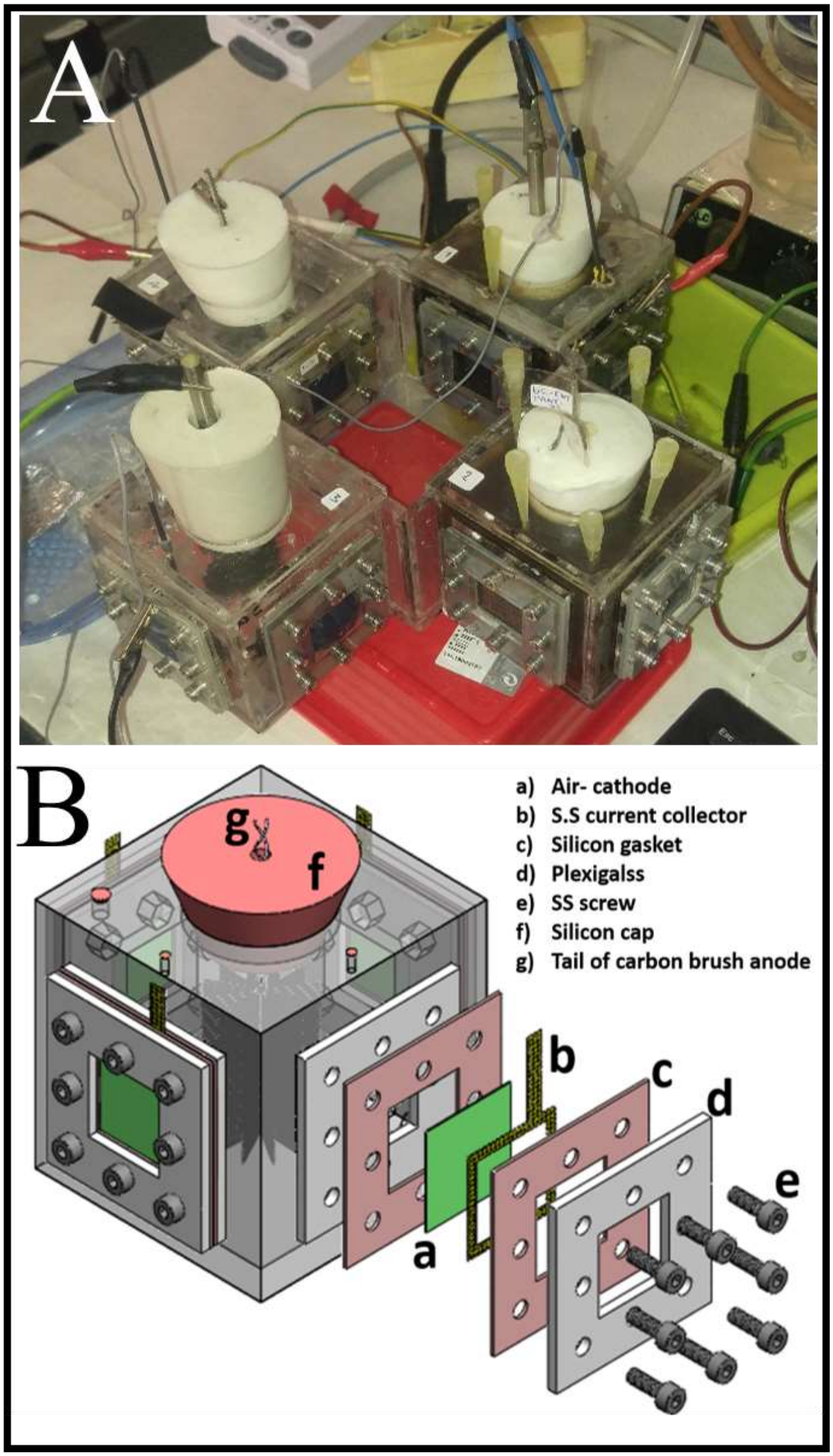

Figure 2.3.1. Quadruple MFC configuration (A) details of one chamber (B)

Table 2.3.1. Anode-cathode connection modes in this study

No.	Anode	Cathode
1	Carbon brush	Gas diffusion electrode
2	Carbon brush	BC-CNT-NZ
3	BC-CNT	Activated carbon coated SS mesh
4	BC-CNT-PANI	Activated carbon coated SS mesh
5	BC-CNT & BC-CNT-PANI	Activated carbon coated SS mesh

2.4 MFC incubation

The system was incubated with anaerobic sludge from the hydrolysis stage at biogas plant (Biotech. Sys. Srl, Bologna, Italy). The sludge was diluted 50:50 V/V by phosphate buffer solution (0.1 M PBS), and potassium acetate (2.5 g/l) was used as the feed for bacteria. Buffer salts provide a suitable neutral pH and prevent significant pH drop during the microbial growth phase and MFCs' operation [84]. After incubation, the MFCs were left in open-circuit voltage (OCV) overnight. Then the circuits were closed by 1 kΩ resistances for colonization. In closed-circuit mode, once the voltage reached under 100 mV, acetate was added. It took 21 days for colonization, and then the resistors were removed, and the systems continued on OCV mode.

2.5 Characterization methods

Attenuated total reflectance fourier transform infrared spectroscopy (ATR-FTIR) was exploited to find functional groups of NZ on BC film by a Brucker device. The degree of crystallinity was measured by x-ray diffraction (XRD) (Philips, Germany) and quantified by the Segal equation [85]. No pretreatment of the sample was required for ATR-FTIR and XRD experiments

Field Emission Scanning Electron Microscopy (FESEM) (TESCAN, Czech Republic) was utilized for investigating the surface morphology. Two kinds of samples were analyzed by FESEM. For BC and BC-NZ, pretreatment was necessary to make the surface of the samples conductive by one-minute gold deposition. While for BC-CNT and BC-CNT-PANI, the coating was not vital. To do imaging bio-anodes, it is essential to wash the incubated anode with clean MilliQ water very carefully and also slowly (not with a water jet) to maintain attached bacterial biofilm. The samples were then placed in a desiccator at ambient temperature to slowly remove the sample's humidity (overnight). Finally, gold deposition is also required for high-resolution imaging in the FESEM technique. Because of BC's excellent surface for bacteria attachment, no chemicals for fixing were needed in this thesis.

Energy-dispersive x-ray (EDX) spectroscopy measurements provided the atomic percentage of the elements. This technique took 5 minutes for BC-NZ. Longer test duration resulted in burning the sample because of cellulose's nature.

Atomic force microscopy (AFM) (Philips, Germany) was used to calculate the average roughness of the surface (by Nanosurf Easyscan software) [86].

Thermo-gravimetric analysis was carried out to determine the thermal stability of materials. The experiment was performed with TA Instruments (Q50 TGA, USA) where 11 mg of each BC and BC-NZ were first deformed to be embedded in the miniature crucible and then heated under Ar atmosphere from ambient temperature to 500 °C, with a ramp of 10 °C min^{-1}.

Contact angle measurements (Sharif Solar, Iran) were performed to investigate the NZ coating effect on hydrophobicity. To do the experiment, BC and BC-NZ were stuck to microscope slides by double-sided adhesive glue. A drop of water with a certain volume was poured on the sample surface. After ten seconds, the image was captured.

Measuring dissolved oxygen (DO) was carried out in one chamber of the MFC filled by buffer solution with DO meter help (DELTA OHM, Italy). The experiment was performed at room temperature.

2.6 Electrochemical measurements

2.6.1 Electrochemical impedance spectroscopy

Impedance spectroscopy (EIS) was performed in the SCMFC, in three-electrode mode. The reference electrode in all electrochemical measurements was Ag/AgCl, (3M KCl). For studying air-cathodes, GDE and BC-CNT-NZ as the working electrodes and carbon brush anodes as the counter electrodes were utilized. In all experiments, the reference electrode was located near the working electrode to reduce the cell ohmic resistance effect. Also, for studying BC-CNT and BC-CNT-PANI, they were used as working electrodes, while the counter was the SS mesh air-cathode. The frequency range for EIS was 100 kHz to 20 mHz. The goal of EIS was determining charge transfer resistance (R_{ct}) and the capacitance of the electrodes by the equations discussed in the results chapters.

2.6.2 Cyclic voltammetry

For studying the air-cathodes, cyclic voltammetry was performed to determine the voltammetric capacitance of the air-cathodes. The scan rate was 10 mV s^{1-} and the potential window was from -0.3V to 0.3V vs. Ag/AgCl. The capacitance was calculated by the current integrated vs. time over the potential. For studying BC-based anodes, CV was done in the potential window from -0.6V to 0.3 V vs. reference electrode by a 0.2 mV/s scan rate to examine the anodes' electrocatalytic behavior. CV analysis also provided the capacitive response of the anodes by the abovementioned method.

The CV was also used for studying the electro-catalytic activity of PANI in O_2 saturated, and Ar saturated atmosphere. For this aim, the GC electrode was coated by PANI through chronopotentiometry (Figure 2.6.2.1 A), similar to that described in section 4.2.2 at a standard three-electrode cell. Before coating, the surface of GC was polished by a specific paste. The standard setup Ag wire as a reference, Pt as the counter, and GC as working electrode are visible in Figure 2.6.2.1 B. The cell is connected to Ar and O_2 inlet for providing required conditions.

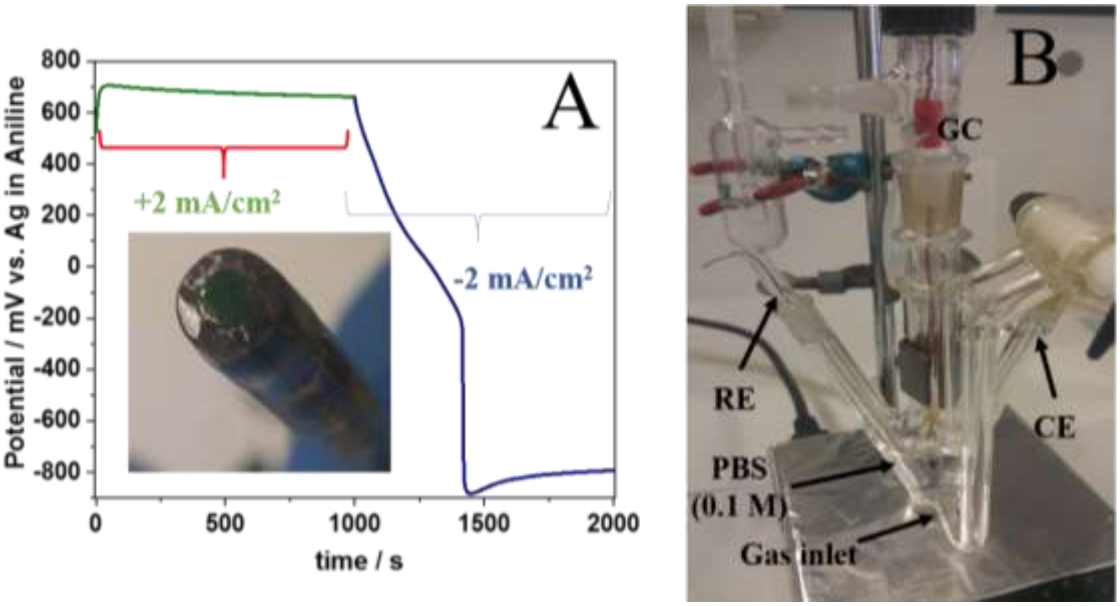

Figure 2.6.2.1. Electro-polymerized GC and its method (A), Standard cell for CV test in O_2 and Ar (B)

2.6.3 Linear sweep voltammetry

Linear sweep voltammetry (LSV) was performed in two and three-electrode modes respectively to record the full cell and single electrode polarization with a scan rate of 0.2 mV/s from OCV to V=0. Also, MFC power density was calculated with LSV from Eq 2.6.3.1[40]:

$$P = V_{Cell} \times I \tag{2.6.3.1}$$

Where V_{Cell} is the cell voltage, and I is the current (mA). The output power can be normalized by cell volume or electrode surface to reach power density. In this thesis, for the cathode electrode case, the cathode surface is used for calculating power density. In contrast, for the anode electrode case, cell volume is utilized for reporting power density.

2.6.4 Rotating disk electrode

LSV was carried out by a rotating disk electrode (RDE) at different rotation speeds to investigate CNT's ORR catalytic activity in a circum-neutral electrolyte. In the RDE test, the working electrode was a glassy carbon (GC) RDE coated with CNT through the procedure described in ref. [87]. Typically, 8 mg of the catalyst was dispersed in a 1 mL solution of deionized water (670 mL), ethanol (300 mL), and Nafion (5%, 30 mL), and it was sonicated for 15 min. Then, 20 μL of the ink was drop cast on the GC electrode (diameter of 2 mm). The experiment was done in a standard-three electrode cell filled by 50 ml PBS (0.1 M, pH=7.6) saturated with oxygen before measurements. A Pt counter electrode and an Ag/AgCl reference electrode were used. Also, the cell had a jacket in which water was under circulation to set a homogeneous determined temperature (25˚C in this work) (Figure 2.6.4.1).

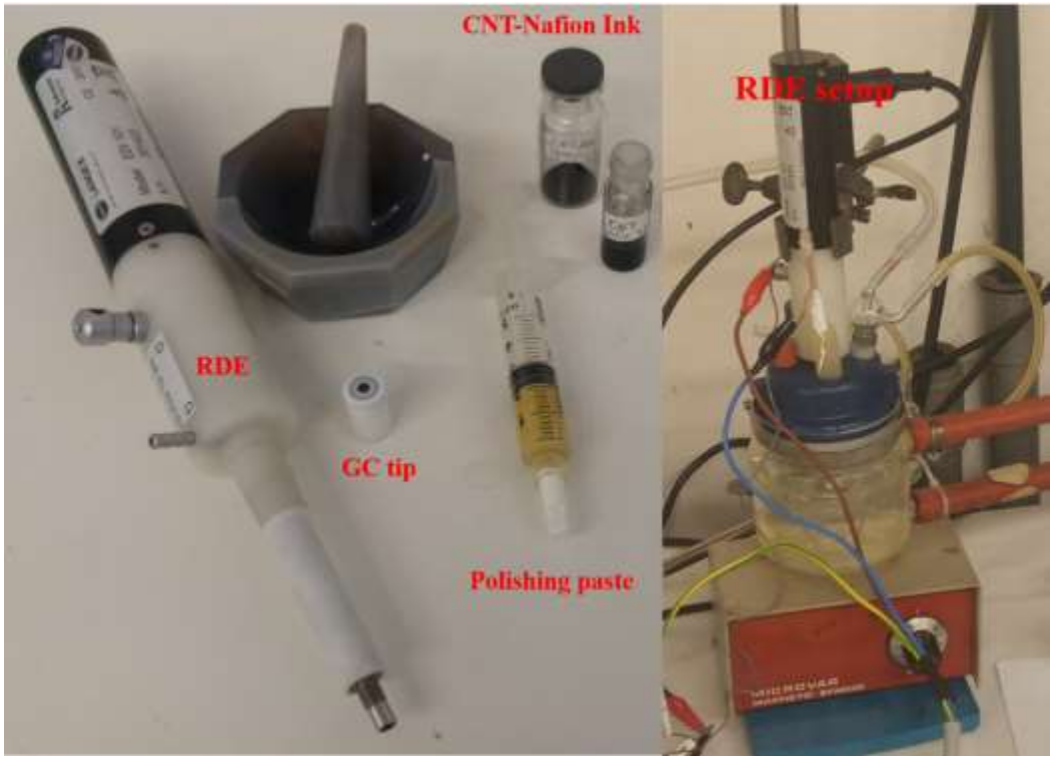

Figure. 2.6.4.1. Rotating disk electrode setup and its compartments

The LSV curves were analyzed to give the Koutecky-Levich (K-L) and Tafel plots (Eq 2.6.4.1 and Eq 2.6.4.2):

$$\frac{1}{j} = \frac{1}{j_L} + \frac{1}{j_K} = \beta\omega^{\frac{-1}{2}} + \frac{1}{j_K} \qquad (2.6.4.1)$$

$$\log j_K = \gamma\eta + \log j_{K_0} \qquad (2.6.4.2)$$

Where j_L, j_K, and j are limiting, kinetic, and measured currents densities, respectively. β is the slope of the K-L plot, and ω represents the angular velocity of the electrode. Also, γ is the Tafel plot slope, and η is measured over-potential[88].

2.6.5 Galvanostatic discharging

For the Galvanostatic (GLV) test, different pulse currents (I_{pulse}) were set to discharge MFC in various pulse times (t_{pulse}): 0.1s, 0.5s, 1s, and 2s. After each discharge, the SCMFC was left to rest in OCV until a stable voltage was achieved (shown in Figure 2.6.5.1).

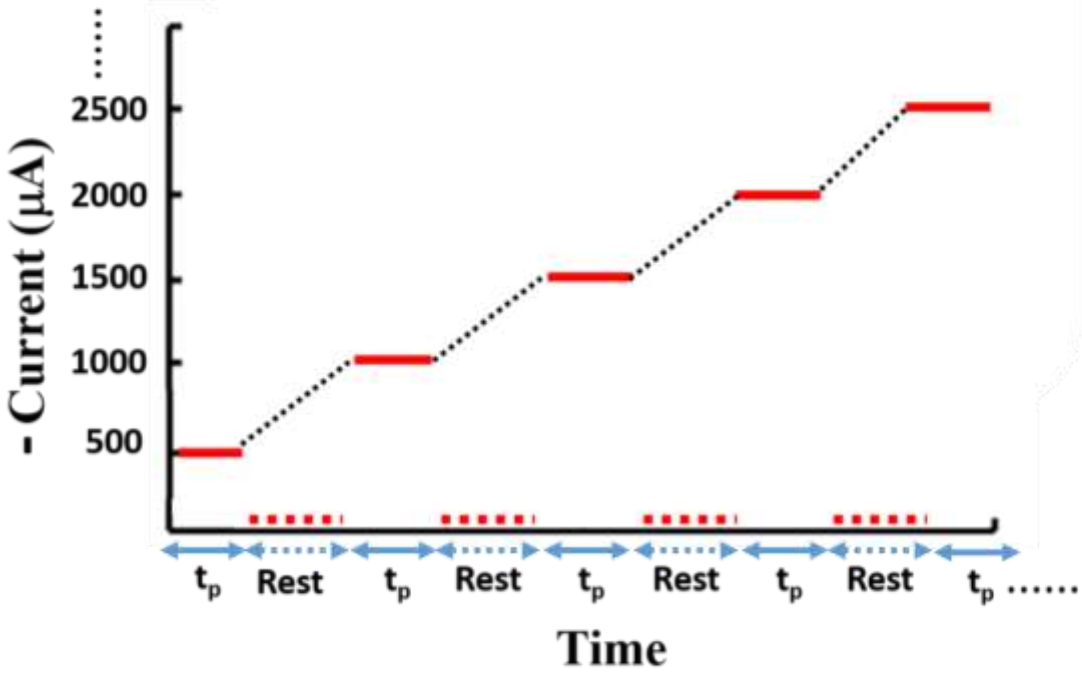

Figure 2.6.5.1. Method of galvanostatic discharging in this study

In this method, cell voltage and anode and cathode potentials were recorded versus the reference electrode (Ag/AgCl) and plotted vs. time. The pulse power (P_{Pulse}) was calculated by the cell GLV discharge, according to Eq.2.6.5.1 [73, 89, 90]:

$$P_{pulse} = E/t_{pulse} = (I_{pulse} * \int_0^t V\,dt)/t_{pulse} \qquad (2.6.5.1)$$

This method is also useful for cell capacitance calculation based on Eq. 2.6.5.2:

$$C_{Cell} = I_{Pulse} \times \left(\frac{dV}{dt}\right)^{-1} \tag{2.6.5.2}$$

2.6.6 Columbic efficiency

Columbic efficiency (CE) was determined by Eq. 4.6.6.1 [91], in which M, F, and V are constant values representing the molar mass of acetate, Faraday's constant, and the SCMFC working volume, respectively. ΔCOD is the difference between the anolyte measured chemical oxygen demand at the beginning and end of a batch.

$$\mathrm{CE} = \frac{\mathrm{M} \int_0^{\mathrm{t}} \mathrm{I}\ \mathrm{dt}}{8 \times \mathrm{F}\ \ \mathrm{V}\ \Delta\mathrm{COD}} \times 100 \tag{2.6.6.1}$$

Chapter 3

Bacterial cellulose-Nano Zycosil: hydrophobic cellulosic layer for membrane electrode assemblies of microbial fuel cells

Typical air-breathing cathodes feature a membrane electrode assembly (MEA) design. MEA key components are: i) the conductive substrate where the electrocatalytic reduction of O_2 takes place, and ii) the hydrophobic and proton-conductive membrane layer. A big challenge in MFC technology is fabricating low-cost membranes and electrodes. Cellulose is the most abundant biopolymer in the world. Among cellulose and its derivatives, bacterial cellulose (BC) has received extensive attention due to its three-dimensional porous nano-structural network, high purity, flexibility, high mechanical strength, and excellent tear resistance in aquatic environments. Also, nano-zycosil (NZ), a diluted solution of hydroxyalkyl-alkoxy-alkylsilyl, has been introduced as a cheap and commercially accessible organosilane. It can change the surface chemistry of bacterial cellulose to moderate its hydrophilicity. In this chapter, BC-NZ characteristics as a novel membrane layer for MEAs are investigated by lots of characterization methods consisting of ATR-FTIR, EDX, FESEM, contact angle, AFM, XRD, TGA, and DTG. Also, some operating parameters necessary for an MEA are discussed.

Elsevier is acknowledged for the permission to reprint some parts of the following publication:

- M Mashkour, M Rahimnejad, M Mashkour, F Soavi, Increasing bioelectricity generation in microbial fuel cells by a high-performance cellulose-based membrane electrode assembly. Applied Energy, 282 (2021), 116150. Copyright (2021).

3.1. ATR-FTIR results

BC and BC-NZ films ATR-FTIR spectra are reported in Figure 3.1.1. In order to have a comprehensive and qualitative comparison of the FTIR spectra, the absorption range was divided into 4000-2500 cm^{-1} and 1500-500 cm-1. Successful treatment of BC with NZ was proved by the bands shown at 775 cm^{-1} and 1270 cm^{-1}, which can be the bending vibrations of Si-CH$_3$ [92]. Besides, the stretching vibration of Si-CH$_3$ was clearly observed by a small peak at 2966 cm^{-1} [93, 94]. The latest peak around 3000 cm^{-1} presented proof of the hydrophobic property of BC. Also, the clear and sharp signal among 1025 cm^{-1} and 1035 cm^{-1} showed Si-O bond [95]. In this wave number range, it can be found even a peak proving the C-O deformation of cellulose (overlapped with alkoxy group's Si-O). Thus, for both BC and BC-NZ, the peak normalized intensity at 898 cm^{-1} was calculated and resulted in 1.26 and 1.42, respectively. Therefore, BC-NZ peak increased intensity was attributed to Si-O bond.

The fingerprint region between 1500 and 700 cm^{-1} is of great importance for identifying BC structural changes. The BC crystalline structure was surveyed using two key indexes: total crystalline index (TCI) and lateral order index (LOI) [96, 97]. TCI and LOI were calculated by the ratio of A_{1372}/A_{2920} and A_{1430}/A_{898}, respectively, for both BC and BC-NZ. The bands at 1430 cm^{-1} and also 898 cm^{-1} reflect the crystalline and amorphous BC [98]. A decrease in both LOI and TCI (Table 5.1.1) showed that a slight reaction between BC and NZ had degraded a little the ordered structure of BC and its crystallites. Additionally, the hydrogen bond index (HBI), which is defined as A_{3340}/A_{1330}, was evaluated for both samples, and then no noticeable change in HBI was observed (Table 5.1.1). Hence, the change in –OH group of BC was not significant. This behavior was mentioned earlier by Zanini et al. and Sai et al. for silanized cellulose [99, 93].

Table 3.1.1. Total crystalline index, lateral order index, and hydrogen bond index of BC and BC-NZ

	TCI	LOI	HBI
BC	1.04	1.02	1.01
BC-NZ	0.97	0.85	1.01

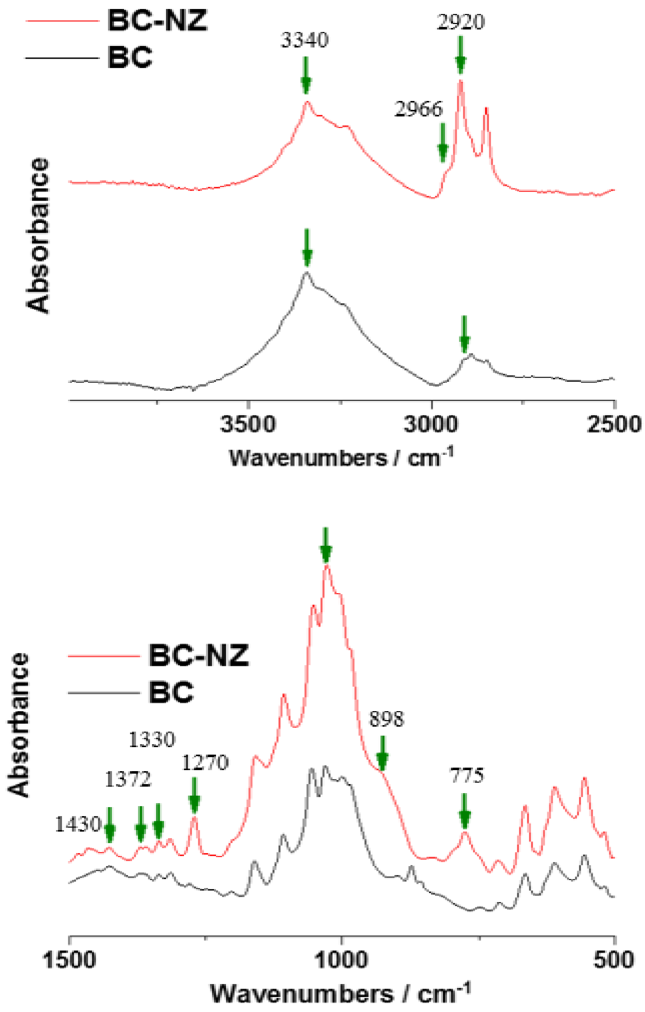

Figure 3.1.1. ATR-FTIR spectra of BC and BC-NZ

3.2. EDX analysis

Besides ATR-FTIR spectra, EDX analysis (Figure 3.2.1) was also done for studying the atomic distribution of carbon, oxygen, and Si on the BC-NZ surface. The results demonstrated that 2.43% of atoms on the BC-NZ surface were Si. Additionally, as can be seen in EDX mapping, Si atoms were distributed homogeneously on BC's fibers. Therefore, the BC surface is expected to become a hydrophobic surface by the successful NZ coating. The main reason for BC treatment with NZ was surface hydrophobicity.

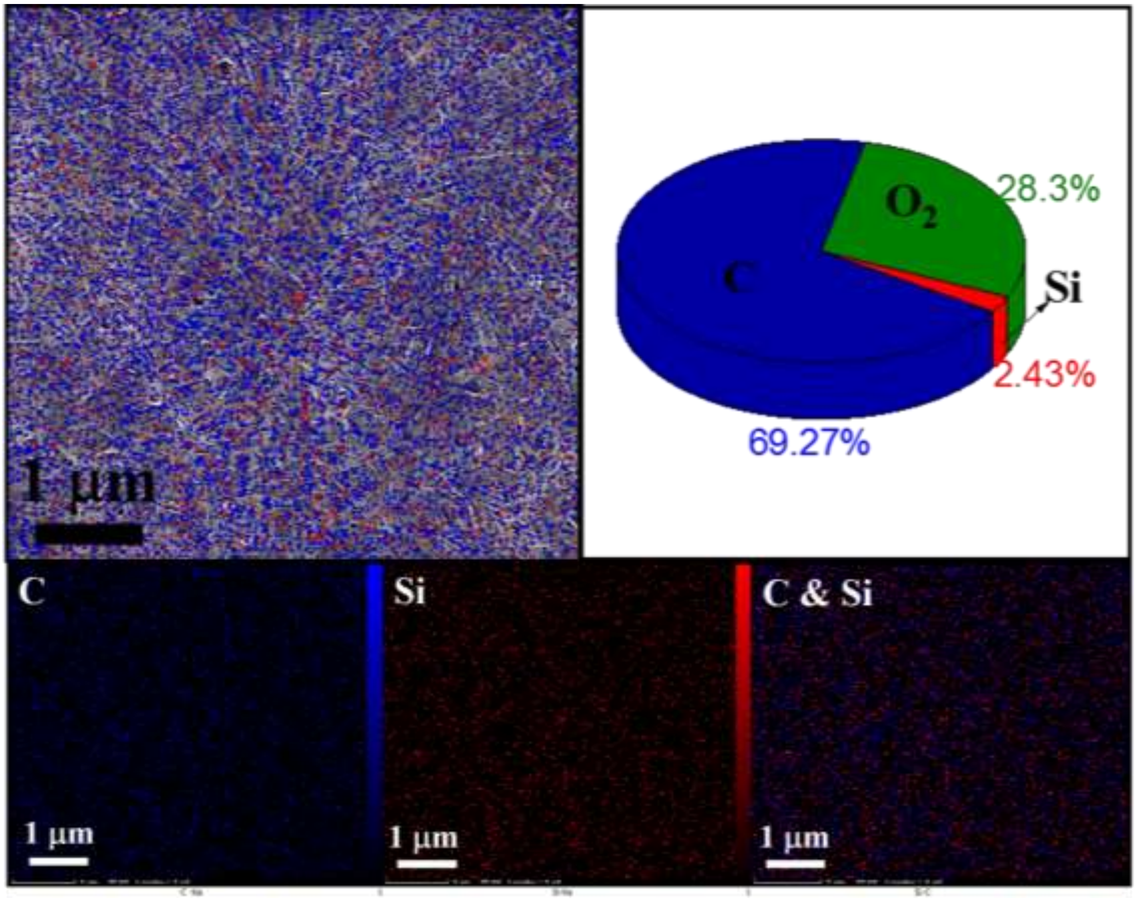

Figure 3.2.1. EDX mapping and atomic distribution of various elements on BC-NZ surface.

3.3. Surface morphology

BC’s FE-SEM images before and after NZ coating are shown in Figure 3.3.1. By comparing unmodified BC and BC-NZ, it can be found that NZ has covered the BC surface considerably, and also, BC surface pores have become smaller. Therefore, the morphology of the BC surface was changed by the coating, as shown in FESEM. The morphology change suggests that treatment with NZ can enhance BC's barrier property. Hence, WCA measurement was performed as a criterion for hydrophobicity.

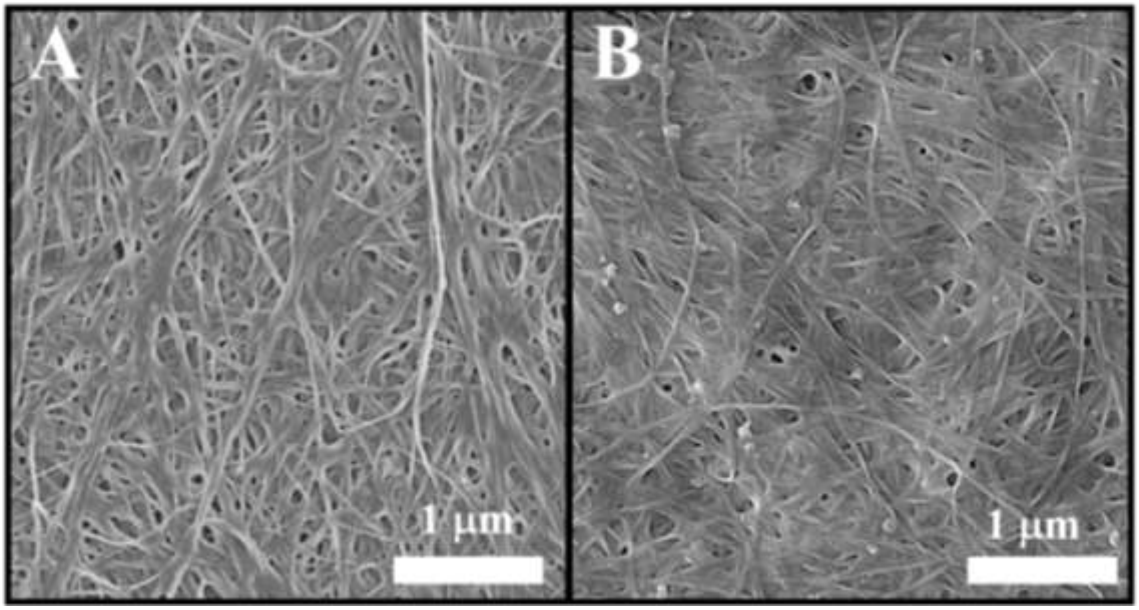

Figure 3.3.1. FESEM images of bare BC **(C)** and BC-NZ **(D)**

3.4. Water contact angle

A considerable change was observed for WCA of NZ-treated BC (85°) compared to bare BC (49°) (Figure 3.4.1 (A and B)). Higher WCA leads to higher hydrophobicity and also improves barrier property against water leakage in the BC-NZ membrane.

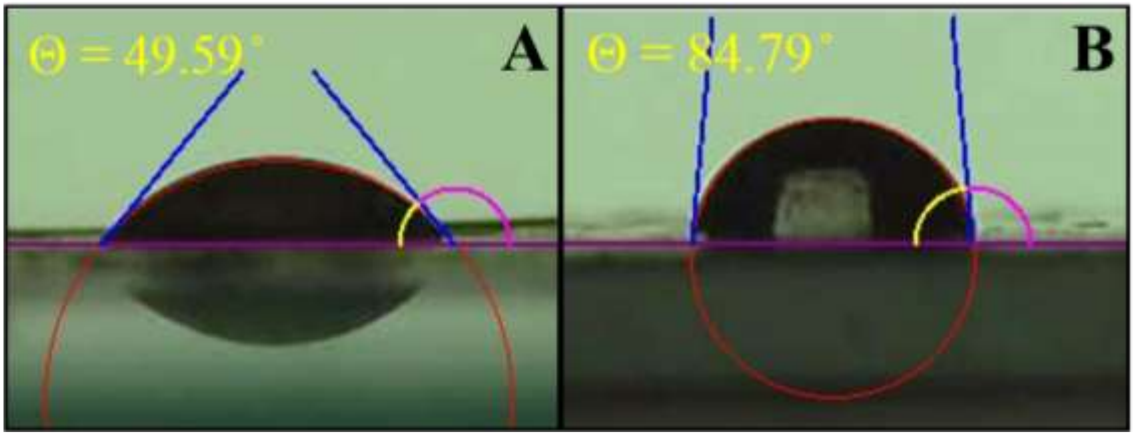

Figure 3.4.1. The water contact angle of (A) bare BC and (B) BC-NZ

It should be noted that wet BC has a water content of 98% w/w. Hence, the unmodified BC surface has noticeable leakage because of its high water affinity and cannot be used as a membrane or separator in air-cathode manufacturing. FE-SEM analyses and WCA could confirm a successful treatment of BC surface by NZ.

3.5. AFM imaging

AFM images (Figure 3.5.1) showed that surface roughness was decreased from 45.66 nm for BC to 32.51 nm for BC-NZ. Also, the values of valley depth and peak height showed a decrease after BC's treatment with NZ. It means that BC’s pores with micron-scale have become filled with NZ [100, 101]. It was also apparent in FESEM images. Hence, all AFM, FFSEM, and WCA results implied the hydrophobic features of treated BC.

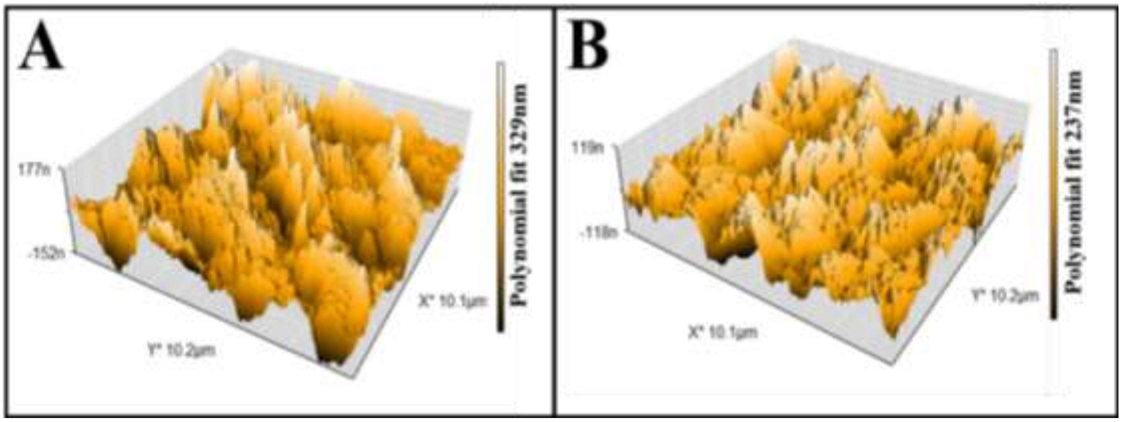

Figure 3.5.1. AFM image of bare BC **(C)** and BC-NZ **(D)**.

3.6. XRD analysis

BC crystallinity was proven by the presence of the diffraction peaks at 2θ 22.8°, 17.8°, and 15° correspondings to the planes 200, 110, and 110 (Figure 3.6.1), respectively [28, 29]. The effect of NZ coating on BC’s crystallinity was studied by the Segal equation. The crystallinity of 92% and 87% for BC and BC-NZ indicates a negligible effect of silane groups on BC crystal structure. This result confirmed the small decrease in TCI and LOI detected by ATR-FTIR spectra and commented in the previous section. Accordingly, both FTIR and XRD analyses verified each other.

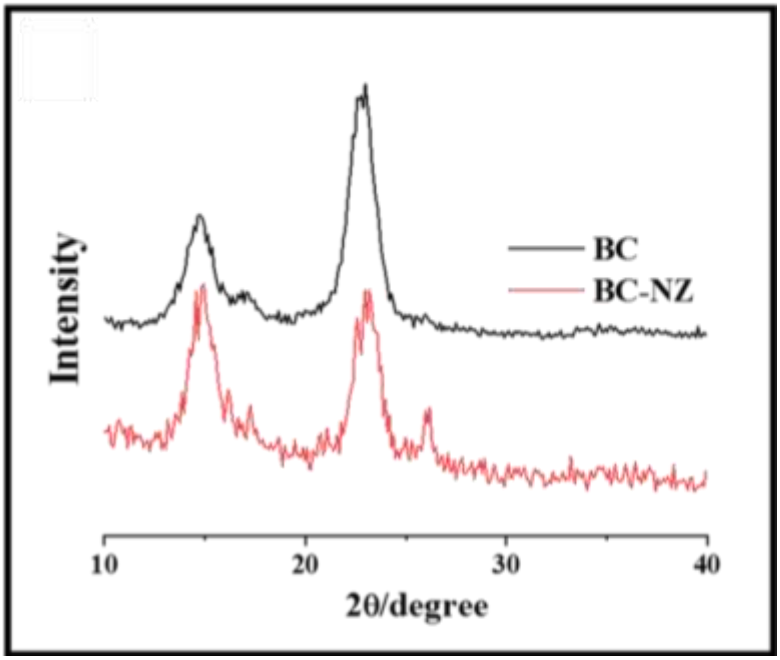

Figure 3.6.1. XRD spectra of BC and BC-NZ.

3.7. Thermal stability

TGA and its differentiation (DTG) curves of BC and BC-NZ are displayed in Figure 3.7.1. At temperatures below 100℃; the TGA curves exhibited a weight loss associated with the evaporation of the sample's moisture (3.5%). The main BC's degradation took place at the range of 320 to 340℃. DTG curves showed that after NZ treatment, the maximum rate of BC's decomposition occurred at higher temperatures (it shifted from 321℃ for BC to 338℃ for BC-NZ). Furthermore, the rate was lower in the case of BC-NZ. Hence, the thermal analysis suggests that NZ's silane groups improved the thermal stability of BC's nanofibers. This result is in agreement with previous BC silanization [93].

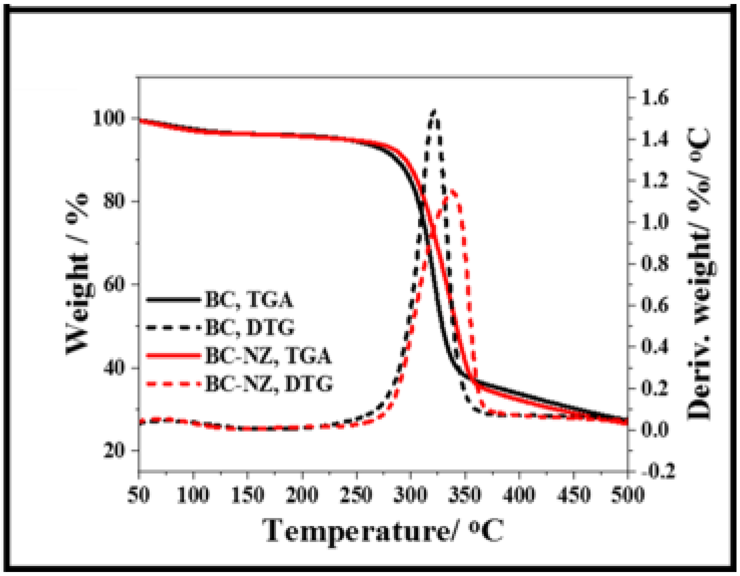

Figure 3.7.1. Thermal stability behavior of BC and BC-NZ.

3.8. Oxygen cross-over

The BC-NZ performance as a barrier against oxygen penetration was evaluated by recording dissolved oxygen (DO) (DELTA OHM, Italy) versus time to be compared with the values for Mylar as control and PTFE-GDE (Figure 3.8.1). The measurement was performed with three similar small cells in which BC-NZ, GDE, and Mylar separated inside PBS from the outside air (Nitrogen purged for 30 min at first to remove initial DO). After 9 h, the cell equipped by BC-NZ demonstrated a plateau at low DO compared to the GDE with growing trend of DO. The excellent anaerobic state was then given by the new MEA. Indeed, NZ has provided hydrophobicity to prevent anolyte leakage and also excellent barrier properties against oxygen penetration. It is a very positive point for the use of NZ compared to PTFE.

3.9. Evaporation rate

The evaporation rate of anolyte from the surface of the air-cathode is another critical parameter in SCMFC. To do this aim, all three cells were weighted in a 90 h duration to measure the PBS weight-loss by evaporation (Figure 3.9.1). BC-NZ and the GDE presented almost the same behavior. A little higher evaporation rate for BC-NZ can be due to the hydrophobicity and humidity balance in BC-NZ.

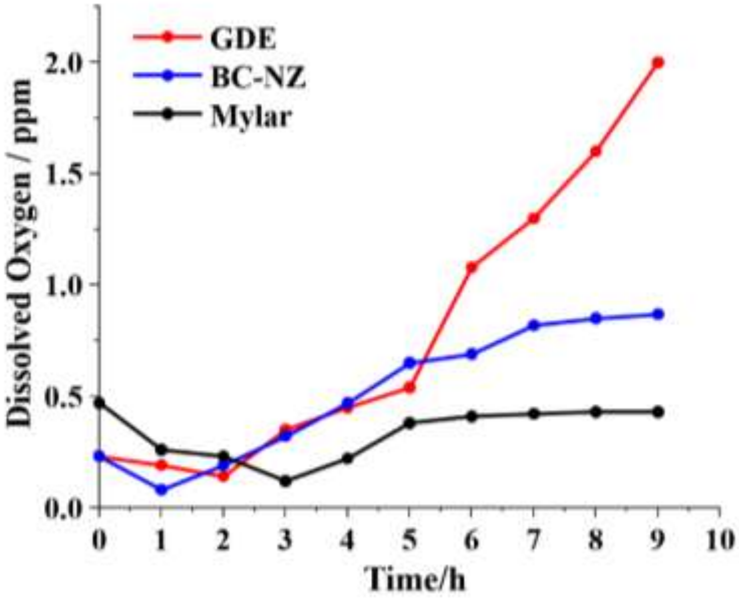

Figure 3.8.1. Dissolved oxygen versus time in a buffer solution of a small MFC chamber exposed to air by various air-cathodes.

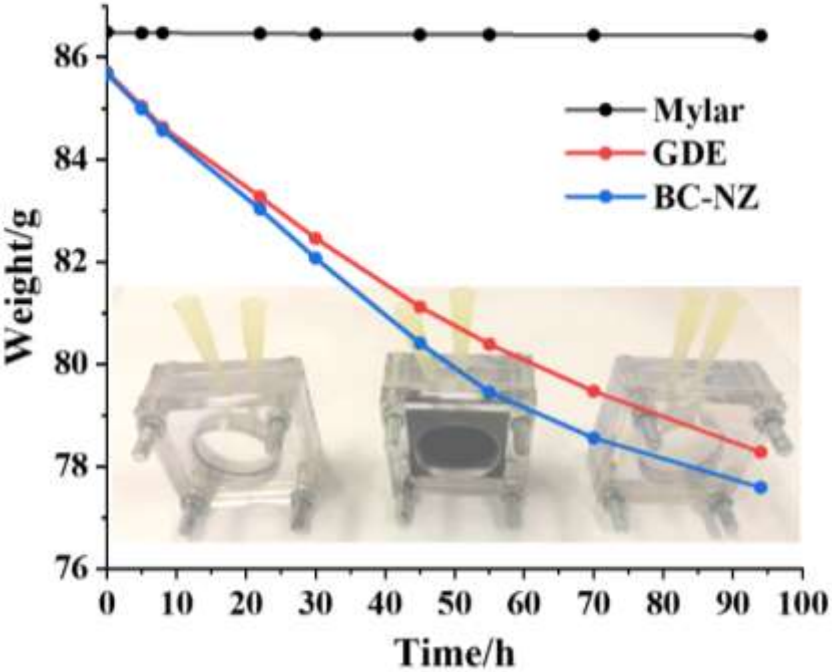

Figure 3.9.1. Weight loss versus time for small MFC filled with buffer and exposed to air through different air-cathodes.

3.10. Morphology analysis of carbon nanotubes coated bacterial cellulose

Figure 3.10.1 displays surface and cross-section images of the BC-CNT air-cathode after vacuum filtering of CNT on BC. CNT covered BC surface so densely that BC fibers are not visible in the surface image. Also, BC and CNT's interface was signed by a red dash line in Figure 3.10.1 B. It is evident that CNT was strongly connected to the BC surface by the binder-less coating method. Being CNT a conductive material, the filtering approach enables to transform BC into conductive cellulose. Also, it should be noted that despite using no binder, a homogeneous coating occurred. The coating thickness is less than 25 μm with a mass loading of below 1 mg/cm^2.

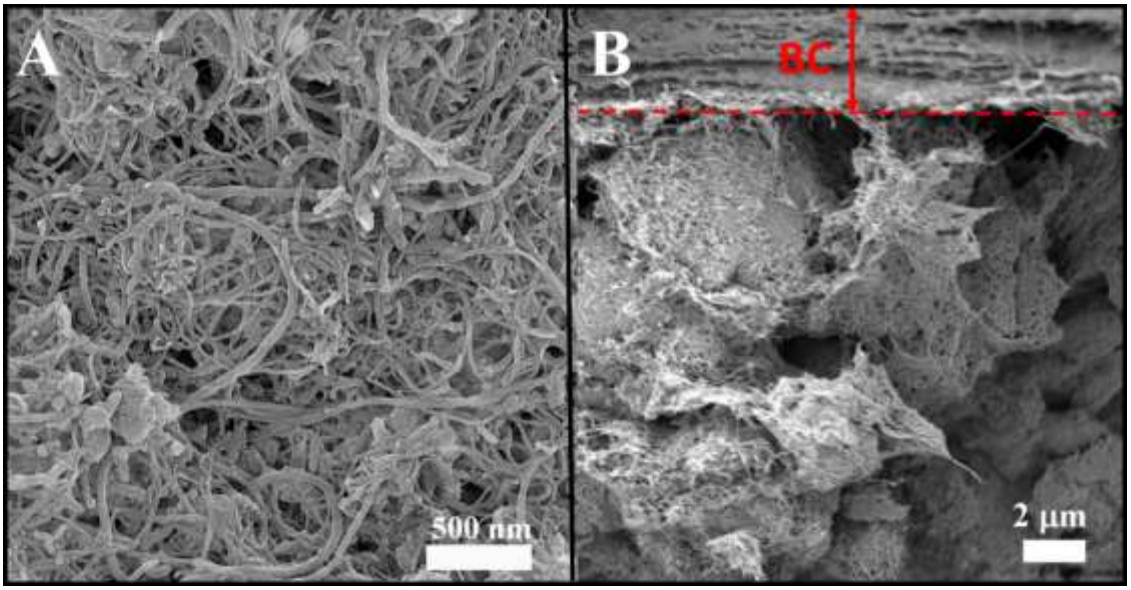

Figure 3.10.1. FESEM images of **(A)** CNTs coated BC surface, **(B)** cross-sectional image of BC-CNT.

3.11. Hydrophobicity effect of BC on its performance as an MEA in MFC

It is vital to know the suitable hydrophobization degree of BC for MEA application. A moderated WCA may present higher performance. It can be found from the theory, previously brought up for air-cathode's gas diffusion layer (GDL) by Ci et al. [57]. To the best of our understanding, this is the first time that the hypothesis has been considered by the MEAs. As can be seen in Figure 3.11.1, ORR requires enough electrons, protons, and oxygen. For the case of the MEA, protons can cross BC-NZ and meet electrons and air-oxygen at the BC-CNT interface. As observed, high contact angle (130°) can decrease the number of protons arriving at the BC-CNT interface and thus results in a limiting ORR rate. On the other hand, the low contact angle (49°) leads to leakage, and, therefore, because of the lower concentration of water-soluble oxygen rather than that of air oxygen, ORR is controlled by the oxygen. Hence, a balanced WCA (85°) is needed to provide sufficient protons and oxygen molecules for the reaction sites and also act as a barrier to anolyte leakage.

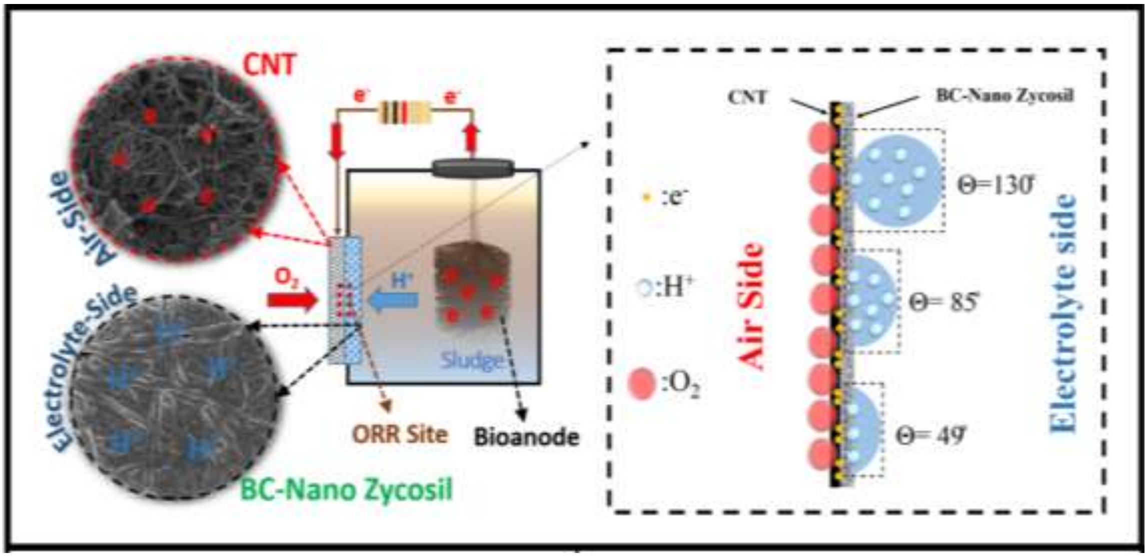

Figure 3.11.1. The role of BC-CNT-NZ in SCMFC and the effect of WCA on MEA's performance.

3.12. Conclusions

According to the results discussed in this chapter, a novel membrane electrode assembly based on hydrophobic BC and a thin CNT layer was fabricated. The cheap NZ organosilane was coated on one side of the BC-CNT membrane without any chemical treatment using no binders, just by vacuum filtration. The presence of methyl and alkoxy groups of the NZ organosilane on BC was proven by ATR-FTIR and EDX, showing a uniform surface coating of Si atoms on BC-NZ with the atomic percentage of 2.43. Also, XRD analyses indicated a minor decrease in BC's crystallinity after treatment with NZ and confirmed LOI calculated by ATR-FTIR-spectra. As a conclusion, the surface chemistry of BC-NZ showed a successful surface silanization of BC by NZ. Moreover, FESEM images demonstrated the surface pores between BC's nanofibers became smaller, and the contact angle showed an increase from 49 ° to 85 ° after NZ coating. Hence, the hydrophobicity feature of BC-CNT was improved by NZ coating. Comparing the dissolved oxygen of the chamber in the presence of the MEA showed the role of the NZ-treated BC in minimizing the crossover of oxygen to the chamber. Therefore, through a low-cost method, cheap BC became conductive by a thin layer of CNT, and also its high hydrophilic nature was moderated by simple brush coating of hydrophobic NZ. By reported properties of BC-CNT-NZ, it can be used as an attractive MEA in MFCs.

Chapter 4

Electrochemical performance of Bacterial cellulose-Nanozycosil based membrane electrode assembly in a single chamber microbial fuel cell

In this chapter, the fabricated cellulosic membrane electrode assembly is utilized as an air-cathode in a single chamber MFC. The electrochemical performance of the MEA is compared to a commercial gas diffusion electrode. Impedance analysis, linear sweep and cyclic voltammetry, rotating disk electrode experiment, and galvanostatic discharging are performed for better evaluation. Power density, polarization test, capacitive and resistive response of the SCMFC are discussed. Also, a detailed discussion is provided for comparing this work with previous investigations.

Elsevier is acknowledged for the permission to reprint some parts of the following publication:

- *M Mashkour, M Rahimnejad, M Mashkour, F Soavi, Increasing bioelectricity generation in microbial fuel cells by a high-performance cellulose-based membrane electrode assembly. Applied Energy, 282 (2021), 116150. Copyright (2021).*

4.1. Electrochemical impedance spectroscopy

The EIS spectra of commercial GDE and BC-CNT-NZ are shown in Figure 4.1.1. The BC-CNT-NZ Nyquist diagram is not visible except by magnification and exists in an impedance region that is much smaller compared to the GDE's. At 20 mHz, the real and imaginary components of impedance for the MEA were respectively 114.283 Ω and 122.28Ω compare to 2.8 kΩ and 10.8 kΩ for GDE showing much higher resistances. At the high-frequency region, the Nyquist plot of BC-CNT-NZ showed a semicircle attributed to the CNT and the SS current collector connection. At the middle frequency region, a line is seen by a slope around 45° representing the diffusion of the ions into the BC-CNT-NZ porous structure (with 55Ω of diffusion resistance), which is modeled with the Warburg element. Besides, in the low-frequency range, BC-CNT-NZ, the capacitive behavior appears much more distinguished compared to its Warburg part. [102, 103].

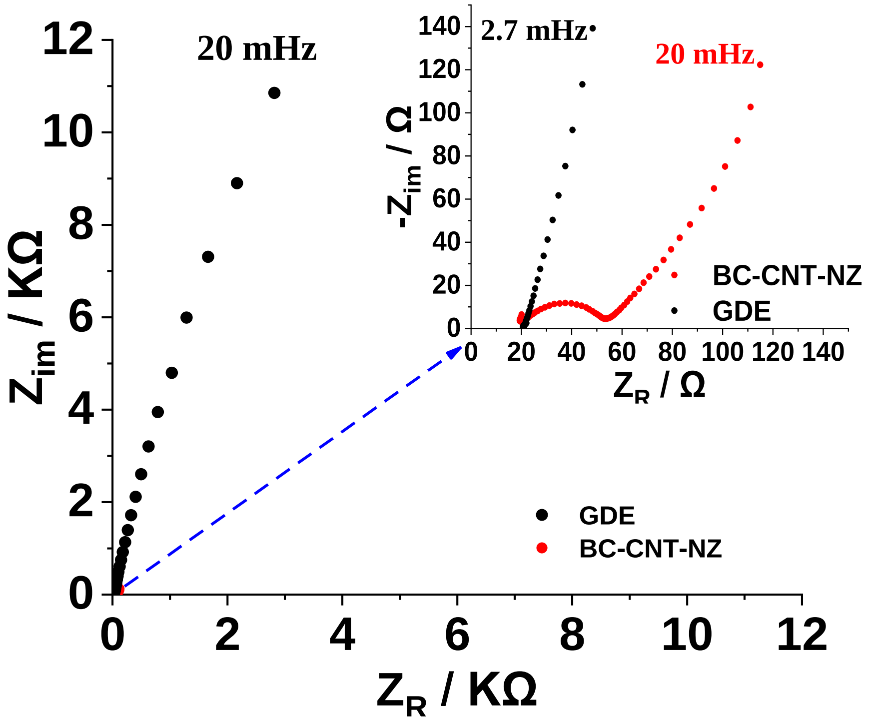

Figure 4.1.1. Nyquist plots of the air-cathodes (BC-CNT-NZ and GDE) as working electrodes at SCMFC in three-electrode mode (carbon brush as auxiliary and Ag/AgCl as reference) in the frequency range of 100 KHz to 20 mHz.

Also, the capacitive response of BC-CNT-NZ at the lowest measured frequency (20 mHz) is 65 mF. This value was calculated by Eq 4.1.1 [104]:

$$C=1/Z_i2\pi f \tag{4.1.1}$$

Where Z_i shows the impedance imaginary component at the frequency (f). The capacitive response of the GDE calculated at 20 mHz by Eq. 4.1.1 presented 733 μF. Therefore, by EIS measurement, it was found that the cellulosic MEA had higher capacitance with lower resistance rather than the GDE.

4.2. Linear sweep voltammetry

The LSV in Figure 4.2.1 A showed that ORR's onset potential for the MEA compared to the GDE was at least 100 mV higher. It is of great importance for the SCMFCs to operate at high voltage. Additionally, the BC-based MEA generated much more current versus the voltage range investigated. At -0.3 V vs. reference electrode (Ag/AgCl), a current of 0.75 mA was recorded.

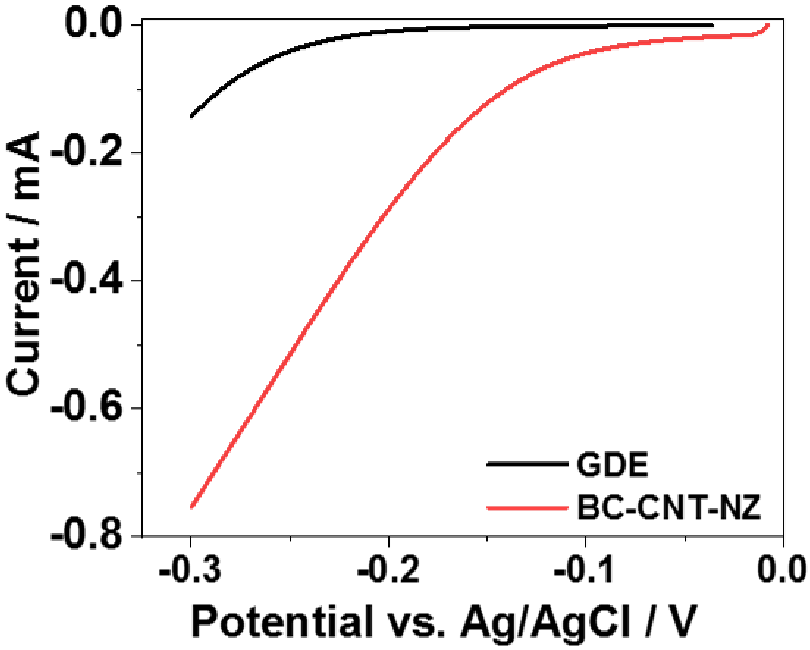

Figure 4.2.1. LSV of BC-CNT-NZ and GDE at 10 mV/s in sludge in three-electrode mode; carbon brush and Ag/AgCl as counter and reference electrodes, respectively.

Moreover, the linear part of the LSV had a higher slope for the MEA, and it was in accordance with the lower impedance of the electrode calculated by EIS results. LSV findings also indicated that the MEA with higher catalytic property than the GDE could perform as an appropriate air-cathode in MFC.

4.3. Cyclic voltammetry analysis

Furthermore, by CV analysis, the voltammetric capacitance of the electrodes was measured (Figure 4.3.1). The MEA's voltammetric currents are much higher than GDE's; hence higher capacitance was expected for BC-CNT-NZ rather than GDE. The calculated capacitance for BC-based and GDE cathodes was 84.44 mF and 2.47 mF, respectively, confirming the EIS results. LSV and CV showed some details about the catalytic activity and also the capacitance of the electrodes.

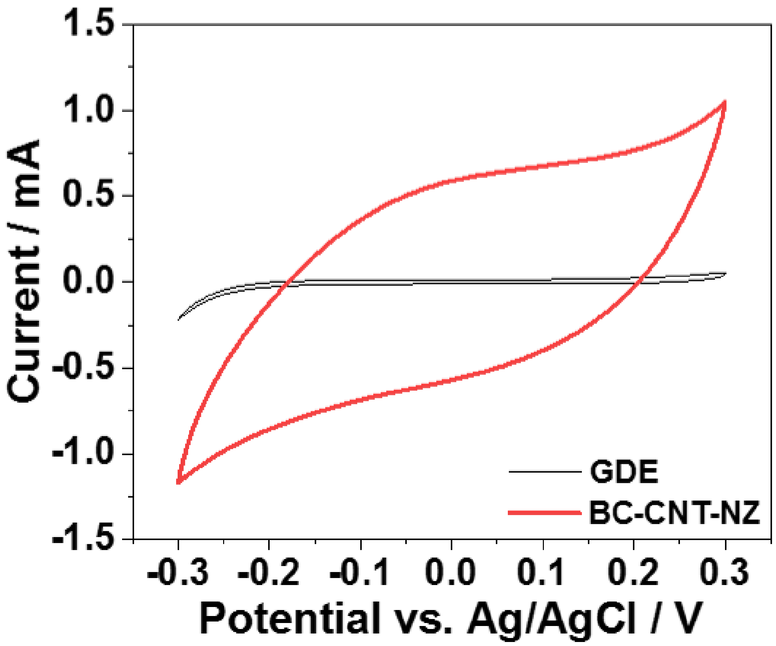

Figure 4.3.1. CV of BC-CNT-NZ and GDE at 10 mV/s in sludge in three-electrode mode; carbon brush and Ag/AgCl as counter and reference electrodes, respectively.

4.4. Rotating disk electrode experiment

In order to study the ORR catalytic activity of the MEA, a bare glassy carbon (GC) and a CNT modified GC were tested by an RDE in a buffer solution with an oxygen saturated state. Figure 4.4.1 A shows the LSV results of the RDE at a scan rate of 5 mV/s and a rotating speed of 0, 400, 900, 1600, and 2500 rpm. The CNT modified GC-RDE current density is formed from faradic and capacitive components. From the LSV curves, the K-L plots were obtained (reported in Figure 4.4.1 B) in a potential range in which both mass transfer and kinetic limitations influenced the response. To avoid the capacitive current, the current density at each potential of the LSV was subtracted by the value measured at an Ar-saturated solution. The K-L plots slope (β) (Eq.2.6.4.1) depends on the number of transferred electrons in the ORR [87].

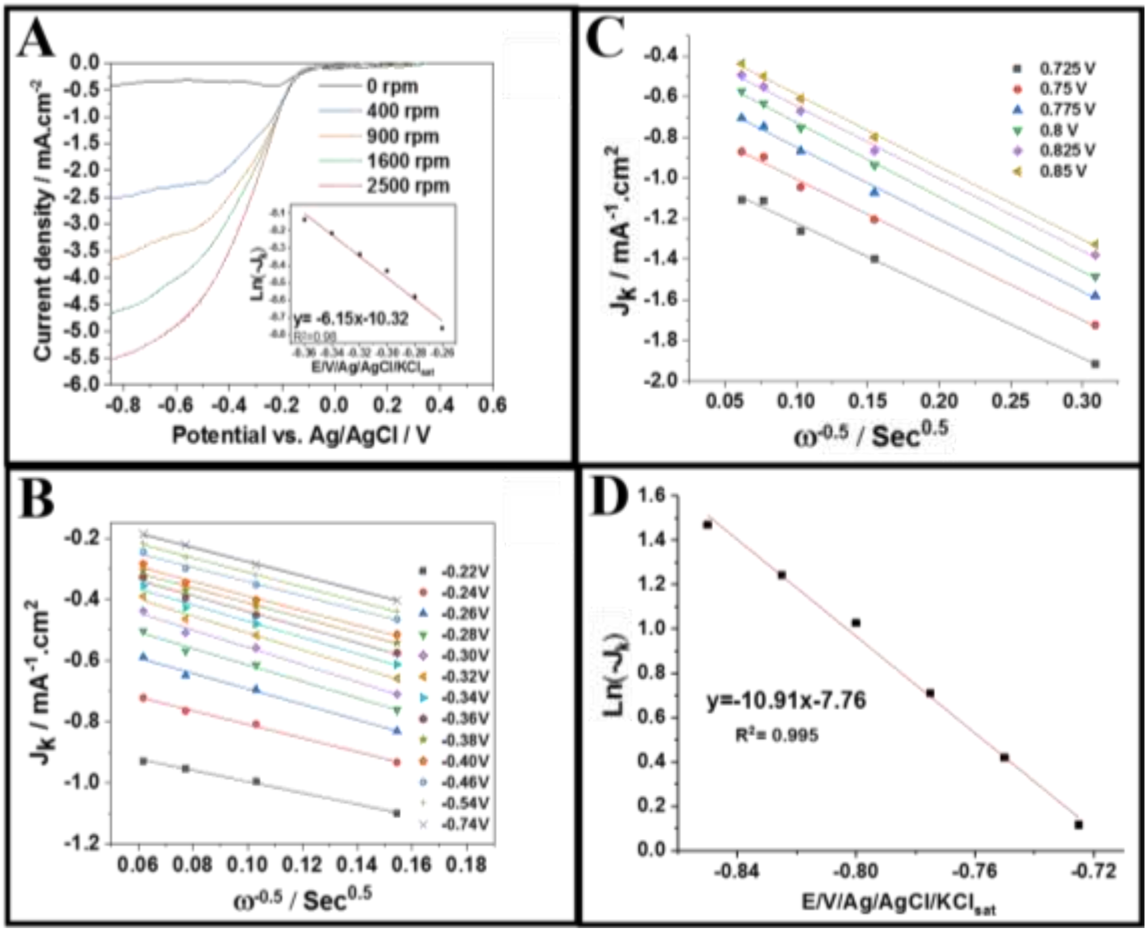

Figure 4.4.1. LSV and Tafel plots**(A)**, K-L plots **(B)** of GC-CNT, K-L plots **(C),** and Tafel plots of bare GC **(D)** in various rotating speeds in a standard three-electrode cell.

The higher slope means fewer transferred electrons. The slope of K-L of CNT-GC was 1.84 compared to 3.56 that calculated for bare GC (Figure 4.4.1 C). RDE results indicated that CNT positively affected the number of electrons taking part in ORR. Furthermore, the

Tafel plot slope for CNT coated GC was 6.15 (inset of Figure 4.4.1 A) compared to that 10.91 for GC (Figure 4.4.1 D).

4.5. Polarization curves and power density

Figure 4.5.1 A demonstrates the LSV polarization and power density curves of the SCMFC assembled by the MEA and the GDE cathodes. The SCMFC produced a maximum power density of about 80 mW/m2 by the MEA, showing more than three times higher than the cell’s output in the presence of the GDE (25 mW/m^2). The OCVs for the two cells were almost the same, while for the GDE, the SCMFC initial potential drop was much higher than that for the BC-based MEA. Also, the slope of the linear part of the polarization curve at the region of the middle-high currents for the MEA was lower compared to the GDE’s polarization slope. These two features were in accordance with the lower resistance and the higher capacitance of BC-CNT-NZ vs. the GDE cathode. The polarization curves' slope demonstrated internal resistances of 0.8 kΩ and 1.84 kΩ for SCMFCs with the MEA and GDE, respectively. The role of each anode and cathode was further clarified by monitoring the potentials of the single electrode during polarization tests of the SCMFCs, and the results are visible in Figure 4.5.1 B. The anodes behavior in both cells was almost similar, while the MEA cathode showed a lower voltage drop at the lowest currents and a lower slope at the range of mid-high currents rather than that of the GDE. This result showed that the SCMFC response had been mainly affected by the air-cathode performance and improved by substituting the GDE with the MEA. In this study, the noticeable point was that a homogenous contact between BC and CNT junction led to a low ohmic drop in the SCMFC. A maximum power density of 2.42 mW m^{-2} in an SCMFC was reported in one previous study in which a chemically modified BC was utilized as a membrane separating a carbon cloth GDE from the anolyte [72]. The low reported performance in that work may be due to the poor connection between BC and GDE. We have successfully fabricated an effective monolithic MEA with a very good and low resistance coating of CNT on BC in this work.

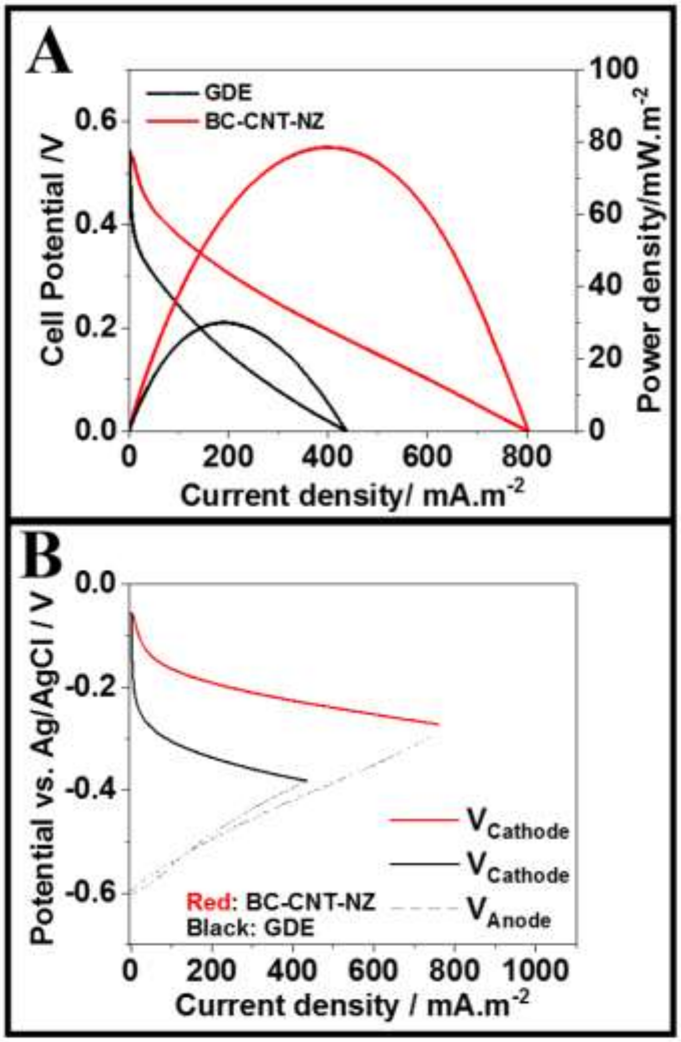

Figure 4.5.1. Power density and polarization of the SCMFCs by LSV test in two-electrode mode and a scan rate of 0.2 mV/s **(A)** and polarization test of single electrodes by recording the electrodes' potential vs. Ag/AgCl reference electrode **(B)**

As mentioned earlier in the previous chapter, BC-NZ showed good barrier property against crossing oxygen. In MFC, cathode potential depends on the cathode's access to oxygen. If oxygen is not supplied, the cathode potential decreases to low values. It is a mass transfer limitation. To validate the barrier property of BC-NZ, the CNT coated side, and NZ coated side were exposed to the anolyte and the air, respectively. Indeed, the MEA's sides were reversed in the SCMFC. As shown in Figure 4.5.2, the cell voltage decreased to 180 mV, considerably lower than the value seen in Figure 4.5.1. Furthermore, the power density produced in this case was around 5 mW/m^2 compared to 80 mW/m^2 in the case of correct sides. The main reason for the decrement by reversing the MEA's sides was the lack of access to oxygen for the CNT-coated side. Thus, this electrochemical method proved that BC-NZ is an excellent barrier against oxygen cross-over.

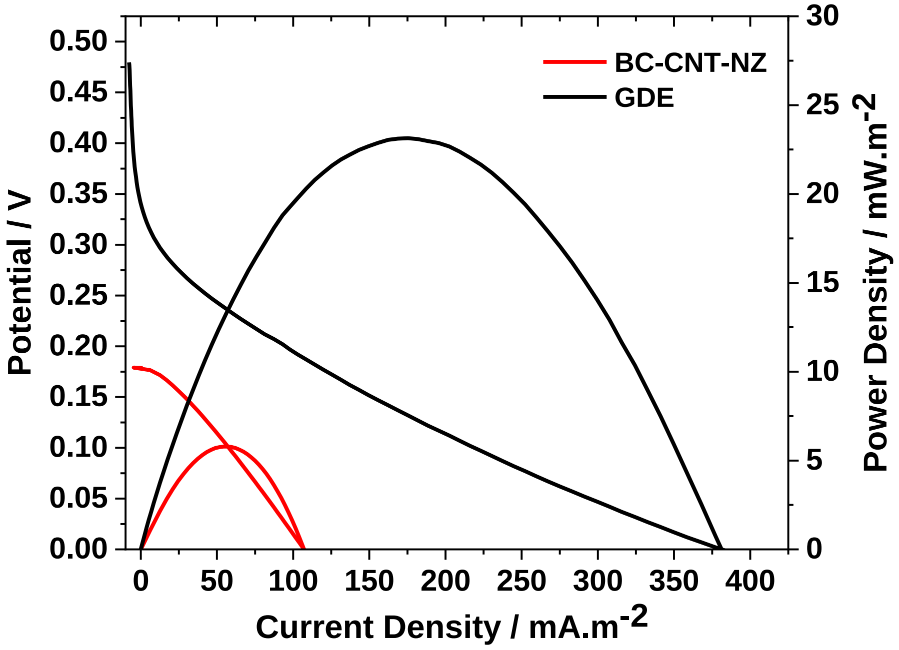

Figure 4.5.2. Power density and polarization curves of the SCMFCs by LSV test in two-electrode mode and a scan rate of 0.2 mV/s (In the presence of GDE and reversed sides BC-CNT-NZ).

4.6. Galvanostatic discharging and capacitive response

The voltage behavior of the GLV test with 2 s discharging duration is visible in Figure 4.6.1. The test is beneficial to study the MFC apparent capacitance [77]. A lower potential drop per discharge duration by a constant discharging current implies the cell's higher capacitance. As it is visible, the SCMFC voltage drop in the presence of the MEA was lower than that with GDE. By discharging currents (from 0.5 mA to 3 mA), the GDE equipped SCMFC demonstrated lower capacitance than the cell with MEA. It was due to the higher capacitance of the MEA than the GDE's, which is clear from potential changes for each air-cathode [80]. For each discharging duration, MEA's voltage decreased slower than the GDE's. While, for the anodes, as expected, a similar potential change was seen. Moreover, comparing the potential drop for the cathodes and carbon brush anodes in this thesis showed that for electricity production in the SCMFC, the main limiting factor was the air-cathode.

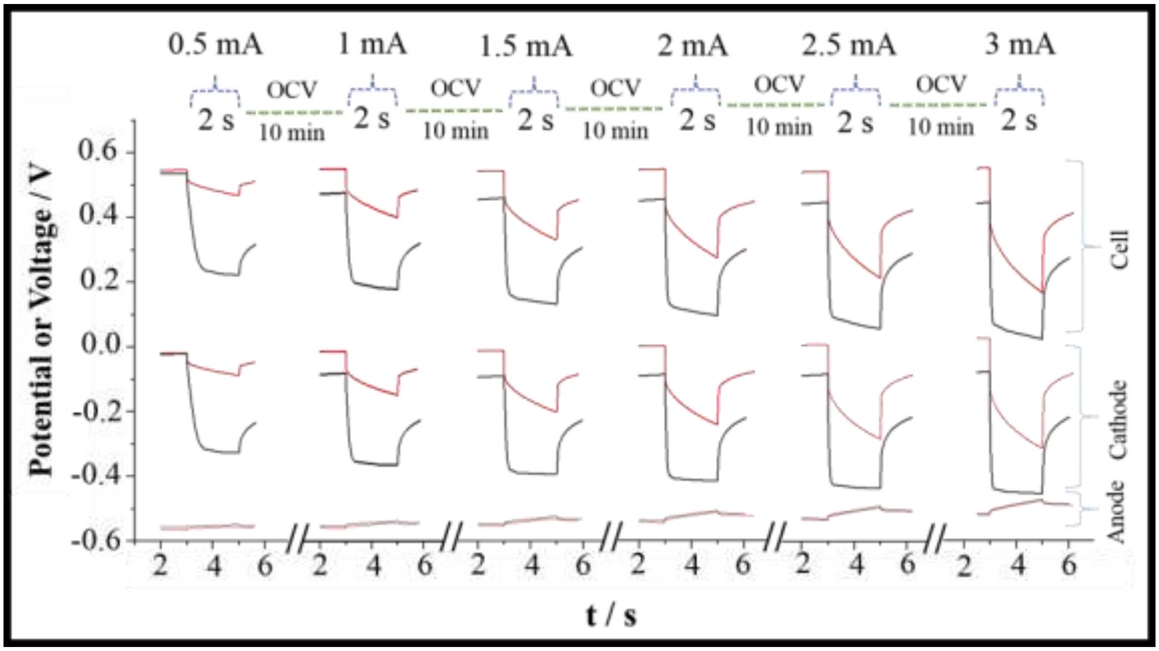

Figure 4.6.1. The voltage of the SCMFCs and potential of single anodes and air-cathodes vs. time by six steps of GLV discharging with 10 minutes of rest time in OCV between discharging periods. (red: BC-CNT-NZ, black: GDE)

4.7. Pulse power output

To calculate the pulse power density of the SCMFC, the cells were discharged by various discharging currents during different pulse times of 0.1, 0.5, 1, and 2 s (Eq. 2.6.5.1). The peak pulse power of 800, 1030, 1210, and 1790 mW/m^2 was generated by the currents of 1.6, 2.2, 2.8, and 4 mA for the SCMFC with the MEA cathode. This cell produced around two-times higher power compared to that of the cell with the GDE. It was noticeable that the generated power density further increased by decreasing the pulse duration. The results brightly show the potential application of MFC as electronic consumer power supplies. However, in real cases like pH and temperature sensors and light-emitting diodes, a higher working voltage is required. Serial connection of the cells and using DC-DC converter provide the sufficient voltage level. According to Figure 4.7.1, if enough voltage is supplied, 3 mA, 4 mA, 4.5 mA, and 7 mA is possible to operate the consumer in a duration of 2 s, 1 s, 0.5 s, and 0.1 s.

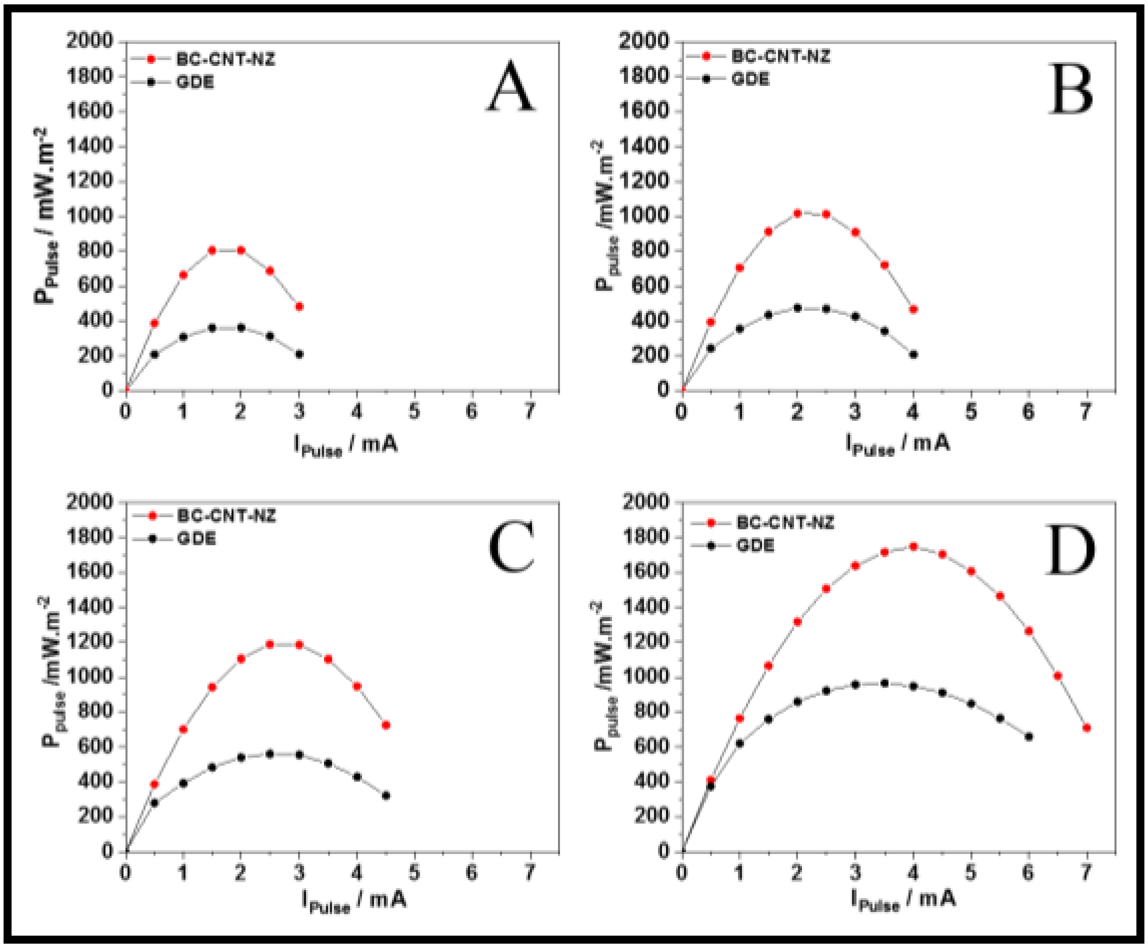

Figure 4.7.1. The pulse power density of the SCMFC obtained by GLV discharges with a pulse time of 2 s **(**A**)**, 1s **(**B**)**, 0.5 s **(**C**),** and 0.1 s **(**D**)**.

4.8. Ragone plot

Figure 4.8.1 shows the Ragone plots for the two cells with the MEA and GDE air-cathodes. To reach the plot, GLV tests by various discharging currents were performed and led to the complete discharge of the cell in multiple durations (t_{pulse} in Eq. 2.6.5.1). The plot was studied to demonstrate the relation between power and energy generation in the SCMFC [105]. The points in the Ragone plot are functions of the current load and discharge duration. In Figure 4.8.1, the range of discharging current is 0.5 mA - 3.5 mA. Generally, for energy storage systems, higher and lower current for discharging give rise to shorter and longer duration, which are also clearly visible in both air-cathodes' Ragone plots. As shown, for the SCMFC with the GDE, both power and energy outputs are lower than those of the MEA. By fast discharging (around 1s) and discharging with a longer duration (more than 10s), the MEA enhanced both generated energy and power. Improvement in the cell behavior by the MEA may be due to its lower ohmic drop and higher capacitance than GDE's.

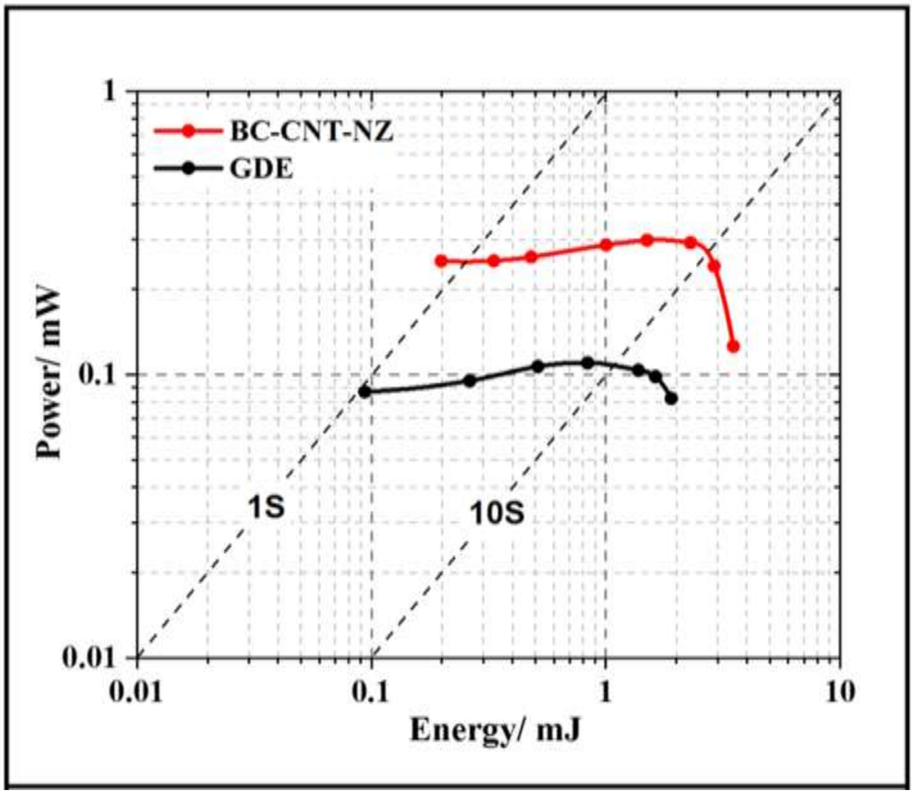

Figure 4.8.1. Ragone plots of the SCMFC with GDE and BC-CNT-NZ air-cathodes

4.9. Columbic efficiency

To achieve the maximum CE in the SCMFC, the maximum number of air-cathodes was utilized (Figure 4.9.1). Four GDE air-cathodes in one cell and four MEAs in the other cell were connected to carbon fiber brush anode in each cell. As can be seen in Figure 4.9.1, the CE by the cell with MEAs increased to 11.7 %, which was approximately three folds higher than that for the GDEs (4.2 %). It was a predictable result because of the current and capacitance behavior and the higher ORR rate of the CNT. The result can also be due to the reduced oxygen crossover by the MEAs (Figure 4.5.2 and Figure 3.8.1), by which anaerobic condition in the reactor was improved, and then exoelectrogens were allowed to produce more electrons.

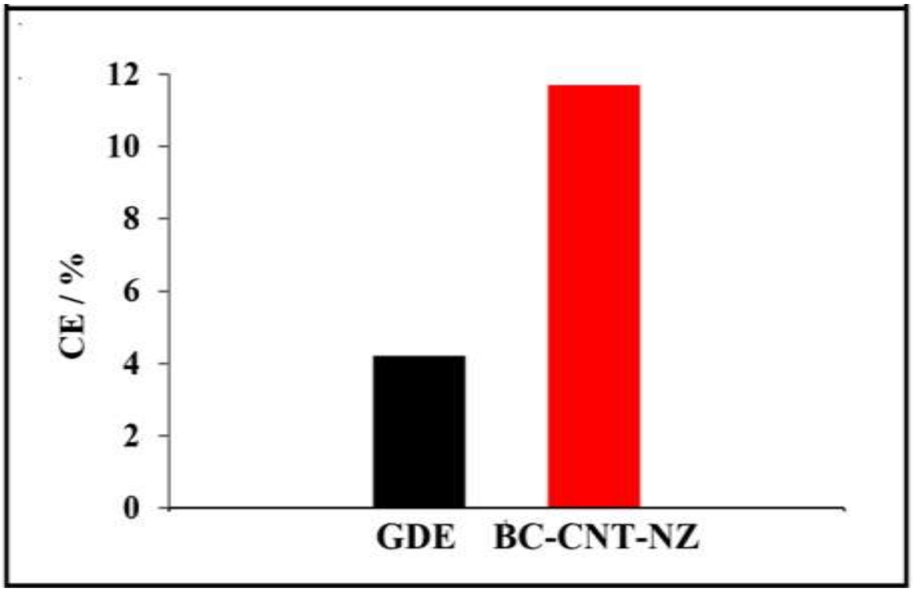

Figure 4.9.1. Columbic efficiency of the SCMFC with GDE and BC-CNT-NZ air-cathodes

4.10. Our BC-based MEA's performance in comparison with previous studies

Table 6.10.1 provides some details for the use of membranes and air-cathodes made by cellulosic materials in MFC configurations collected from the literature. SCMFCs compared to DCMFCs show higher performance. Biffinger et al. could produce a power output of 40 $mW.m^{-2}$ in a mini Double Chamber MFC (DCMFC) with a membrane made by cellulose nitrate and graphite felts for anode and cathode. In that work, the MFC's performance with cellulose nitrate compared to Nafion was lower [106]. As a proton exchange membrane, BC was also utilized in big size DCMFC in which electrodes were from graphite plates. The system increased the power output more than two-fold higher than the commercial membrane. It has shown BC's strong potential as an inexpensive alternative to the costly Nafion [107]. Ci et al. performed cellulose modification by the esterification and then utilized the esterified cellulose instead of hydrophobic PTFE coating on carbon cloth cathode. They improved MFC's performance through the substitution and decreased the air-cathode cost by eliminating costly PTFE [57]. In another investigation, Wang et al. used a membrane made by mixed-cellulose ester to be placed as a separator for

GDE. The performance of the cellulosic separator was similar to that of Nafion [108]. Marzorati et al., in 2017, used the cellulosic shell of maize stalks as a separator in a cylindrical SCMFC on commercial GDE-carbon black and reached a power density of 44 $mW.m^{-2}$ [109]. In a recent investigation, Vilela et al. fabricated Poly (4-styrene sulfonic acid) modified BC to be used as the separator in an SCMFC. The could produce 2.42 $mW.m^{-2}$ power density in the system with platinum-coated GDE [72]. All GDEs mentioned above were manufactured by costly PTFE as a hydrophobic layer and Nafion or PTFE as binders for catalyst coating. In addition, the cellulosic membranes used in the above-described work performed as separate layers for GDEs without a homogeneous connection between membranes and GDEs. Non-homogeneous junction leads to huge internal resistance in MFC and limits electricity generation. The MEA in this thesis has a monolithic structure with very low resistance. It improved the MFC's power output and performed much better compared to the GDE. However, the method for calculating power should be considered for reasonable comparing the MFCs' performance. LSV, Resistance loading and galvanostatic discharge all are different approaches for calculating the power density of MFCs. Hence, the reported power densities may differ by setting different values such as: resistance values, scan rate, pulse time and discharge current. For example, Ci et al. utilized resistance loading method but did not mention the value of pulse time for each loading[57], Vilela et al. applied discharging test by 5 μA pulses and 3 minutes pulse duration [72]. In this thesis, to report power density, LSV anlysis and GLV discharging resulted in peak power densities of about 80 $mW.m^{-2}$ and 1790 $mW.m^{-2}$, respectively.

Table 4.10.1. Performance of different MFC configurations with cellulosic membranes and air-cathodes in producing electrical power

Cellulose membrane	**Anode**	**Cathode**	**Configuration**	**Hydrophobic layer**	**Binder**	**Volume**	**Power density**	**Ref**
Cellulose nitrate	graphite felt	Graphite felt	DCMFC	-	-	1.2 ml	40 mW/m^2	[106]
BC	Carbon plate	Carbon plate	DCMFC	-	-	45 lit	73-200 mW/m^2	[107]
-	Carbon felt	Carbon cloth-cellulosic GDL with platinum	SCMFC	Esterified cellulose nano fiber	Nafion	27 ml	1518.3 mW/m^2	[57]
Mixed cellulose ester filter	Carbon brush	Commercial GDE with platinum 0.5 mg/cm^2	SCMFC	PTFE	-	250 ml	780.7 mW/m^2	[108]
Giant canes and Maize stalks cellulose	Carbon cloth	Carbon cloth GDE with carbon black	SCMFC	PTFE	PTFE	-	44 mW/m^2	[109]
Poly(4-styrene sulfonic acid)/BC	Carbon brush	Carbon cloth GDE with platinum 0.1 mg/cm^2	SCMFC	PTFE	-	900 ml	2.42 mW/m^2	[110]
BC based MEA	Carbon brush	BC-CNT	SCMFC	NZ	Binder-less	250 ml	80-1790 mW/m^2	This work

4.11. Future of our cellulosic MEA in MFC technology

In this thesis, the MEA fabrication cost was approximately 0.09 € for dimensions of 2.5 cm × 2.5 cm and it was noticeably lower than the cost of 0.34 € for the commercial GDE of the same size. Furthermore, the SCMFC performance with the new-introduced MEA was considerably higher than that with the commercial GDE. In multi-cathode design of SCMFCs and the stack of MFCs, the cost of energy generation highly depends on the electrodes' cost. Thus, the BC-based MEA introduced in this thesis is a cost-effective and also energy-efficient approach for scale-up and MFC’s commercialization. The challenges exist still for coating with higher carbon and catalyst mass loading needed for higher redox activity, higher energy generation in MFC systems. Cellulose, as the most widely abundant biopolymer, can play a vital role in the fabrication of low-cost MFC compartments. Higher performance MFC with cheaper constituents will be more attractive to use this system for generating electricity and treating wastewater.

4.12. Conclusions

In summary, this chapter introduced, to the best of our knowledge, the first monolithic MEA based on hydrophobic conductive BC for use in SCMFC. The cellulosic MEA boosted the SCMFC energy output noticeably. Binder-less CNT coating, simple brush coating of NZ resulted in a low-cost MEA and improved electrochemical properties required for an air-cathode of an SCMFC. The EIS results and the polarization data showed considerably lower resistance for the MEA compared to the GDE. It was attributed to the homogeneous junction BC-CNT and high conductivity of CNT. Comparing polarization curves and power densities of the SCMFC in the presence of the MEA in two different modes proved electrochemically the role of the NZ-treated BC in minimizing the crossover of oxygen to the anode chamber. Hence, columbic efficiency also increased by three folds with enhancing anaerobic conditions. The higher catalytic activity of MEA in comparison with the GDE can be attributed to the role of both CNT and NZ modified BC for providing extra oxygen and required protons at ORR active sites. Furthermore, the MEA capacitance compared to the GDE was noticeably higher. By enhancing the mentioned features, the SCMFC's power density was also improved around 320% in the presence of BC-CNT-NZ compared to the GDE. Finally, it should be remembered that the best performance of the BC-based MEA has ever been recorded in this thesis for the MFC system.

Chapter 5

Bacterial cellulose-carbon nanotubes-electro polymerized polyaniline nanocomposite as a capacitive bioanode for supercapacitive microbial fuel cells

In this study, CNT was coated on BC by vacuum filtration and then decorated with PANI by electro-polymerization. The BC-CNT-PANI was investigated as a superpcapacitive bioanode in SCMFCs for the first time. The morphology of the coatings and the colonized bacteria were studied. The main novelty of this work is investigating the effect of the biofilm presence on the capacitive response of CNTs and PANI modified CNTs. The study was carried out by cyclic voltammetry and impedance spectroscopy analysis. Additionally, the effect of the bio-anodes' capacitance on the MFC's performance was measured by galvanostatic discharges. Moreover, the PANI modified electrode was short-circuited to BC-CNT to give a double anode coupled with the air-breathing cathode to improve the SCMFC's performance.

Elsevier is acknowledged for the permission to reprint some parts of the following publication:

- M Mashkour, M Rahimnejad, M Mashkour, F Soavi, Electro-polymerized Polyaniline Modified Conductive Bacterial Cellulose Anode for Supercapacitive Microbial Fuel Cells and Studying the Role of Anodic Biofilm in the Capacitive Behavior, Journal of Power Sources 478 (2020), 228822. Copyright (2020).

5.1 FESEM images of the BC-based electrodes

Figure 5.1.1 shows the FESEM images of the CNT coated layer on BC surface two coating steps; vacuum filtration (A, C) and then PANI coating by electro-polymerization on BC-CNT (B, D). Comparing the FESEM images reveals that after electro-polymerization, the PANI covered the CNTs homogeneously with a small agglomeration. Also, PANI was supposed to cross-link the CNTs with each other and the BC surface to form a much more durable coating relative to the BC-bare CNT without PANI. It should be noted that the coating was accomplished by a quick process, and no chemical initiator such as iron chloride was required.

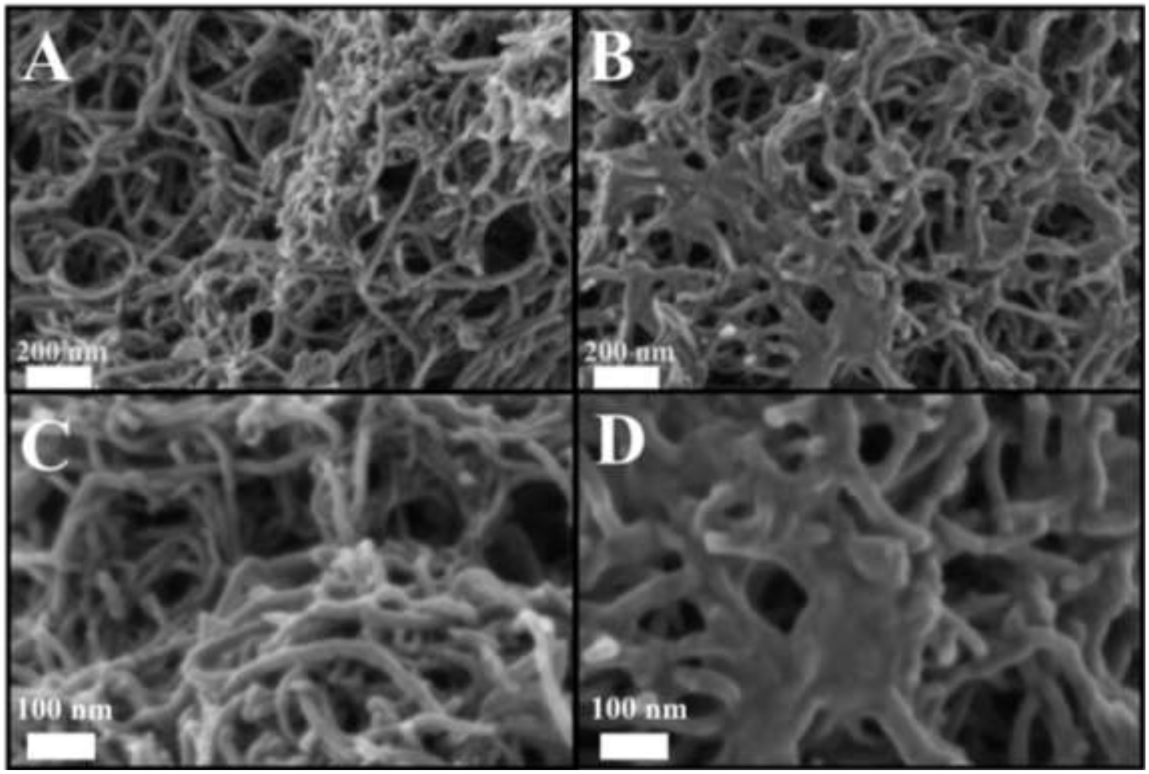

Figure 5.1.1. FESEM images of (**A, C**) CNT coated BC surface after vacuum filtration and (**B, D**) electro-polymerized PANI on BC-CNT.

5.2 EIS analysis

In order to investigate the impact of microbial biofilm on the electrochemical response of anodes, EIS tests were performed in the MFC before colonization and after that (after 21 days and 50 days). Figure 5.2.1 A&B shows the Nyquist curves for the BC-CNT and PANI modified BC-CNT anodes, respectively.

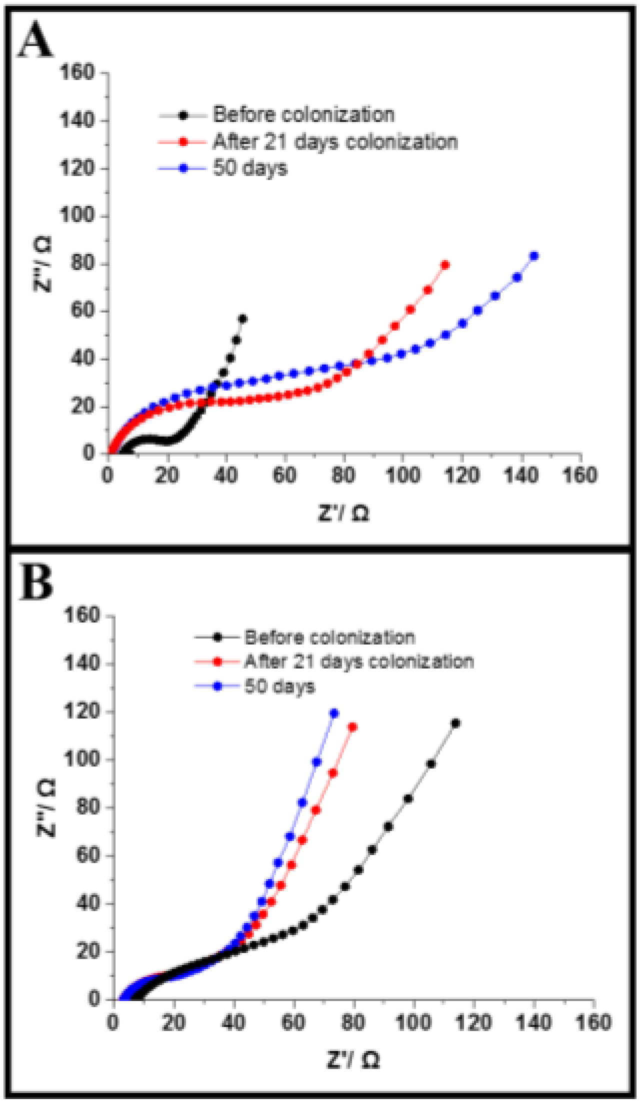

Figure 5.2.1. Nyquist plots for BC-CNT (**A**) and BC-CNT-PANI (**B**) electrodes tested in MFC by a three-electrode setup before and after colonization.

All the plots have a depressed semicircle at the high-frequency region with a low-frequency tail. The semicircle diameter (that may also be formed by two overlapped semicircles) can be due to charge transferring resistance at the interface of electrode/electrolyte (R_{ct}). Also, the tail in the low-frequency region can be due to the electrodes' diffusive processes and capacitive properties. Before colonization, for BC-CNT and BC-CNT-PANI, R_{ct} was 14.52 Ω and 41.28 Ω respectively. As already stated, the PANI has low conductivity at neutral pH. The higher Rct of PANI-modified anode also proved it compared to BC-CNT at Nyquist plots. However, the R_{ct} of the electrodes showed an opposite trend after biofilm formation. Indeed, after colonization in 21 days, R_{ct} increased for BC-CNT up to 48 Ω while for BC-CNT-PANI, it decreased to 24 Ω. Similar behavior was also seen after 50 days. After this duration, R_{ct} for BC-CNT and PANI modified BC-CNT was calculated 72 Ω and 21 Ω, respectively. The reversed trend for R_{ct} after colonization suggested a positive impact of PANI coating on the formed biofilm's charge transfer activity.

Table 5.2.1. R_{ct}, CPE, and n values of BC-CNT and BC-CNT-PANI calculated by Randles equivalent circuit and curve fitting.

	BC-CNT				BC-CNT-PANI			
	$R_{ct}(\Omega)$	CPE ($\Omega^{-1}.s^{n}$)	n	χ^2	$R_{ct}(\Omega)$	CPE ($\Omega^{-1}.s^{n}$)	n	χ^2
Before Colonization	14.52	9.8×10^{-2}	0.84	2.4×10^{-3}	41.28	3.55×10^{-2}	0.68	1.1×10^{-3}
After 21 days colonization	48	4.36×10^{-2}	0.6	1.6×10^{-3}	24	4.34×10^{-2}	0.77	2.7×10^{-3}
After 50 days	72	3.68×10^{-2}	0.54	2.1×10^{-3}	21	4.49×10^{-2}	0.81	3.4×10^{-3}

The Nyquist curves' tails at the low-frequency region were modeled by the constant phase element (CPE). The CPE impedance is defined:

$$Z_{CPE} = \frac{1}{Q\,(j2\pi f)^{n}} \qquad (7.2.1)$$

In which f is the frequency. Once n value approaches 1.0, a phase angle close to -90^0 is seen, and then Q equals capacitance. For the case of n=0.5, Q represents the Warburg line with diffusion-controlled processes and the phase angle of -45^0. The n value for PANI modified anode before biofilm formation was 0.68, and after 21 days and then 50 days reached 0.77 and 0.81, respectively. For BC-CNT, a reverse trend was shown for the n value, and the n values, before colonization, after 21 days, and after 50 days, were calculated 0.77, 0.6, and 0.54. The R_{ct}, CPE, and n values of the electrodes are provided in Table 5.2.1. In order to achieve a deeper understanding of the biofilm impact on electrode performance, phase angle and capacitance vs. frequency as Bode Plots have been studied and demonstrated in Figure 5.2.2 and Figure 5.2.3.

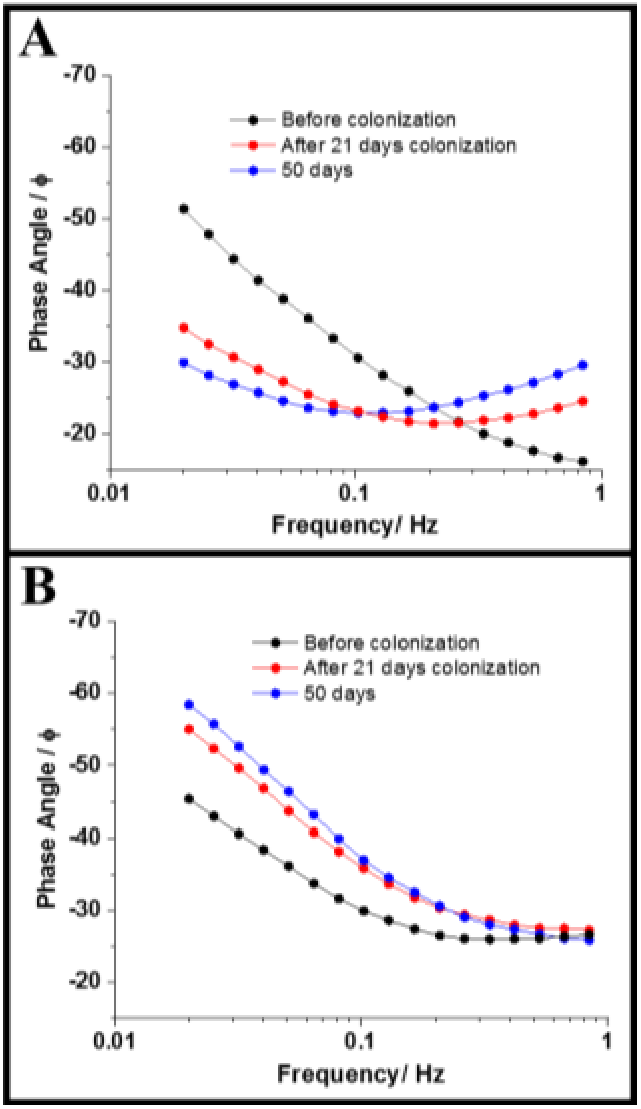

Figure 5.2.2. Bode Plots in terms of phase angle vs. frequency for BC-CNT (**A**) and BC-CNT-PANI (**B**) electrodes tested in MFC by a three-electrode setup before and after colonization.

The organic matter decomposition by microorganisms of anodic biofilm to electrons and protons is performed by a slow reaction. Thus the low-frequency range of EIS spectra is of considerable significance. [111]. To do this aim, the capacitance values in Figure 5.2.3 were measured at frequencies below 10 Hz using Eq (5.2.2)[112]:

$$C_R = \frac{-Z"(\omega)}{2\pi f|Z(\omega)|^2} \tag{5.2.2}$$

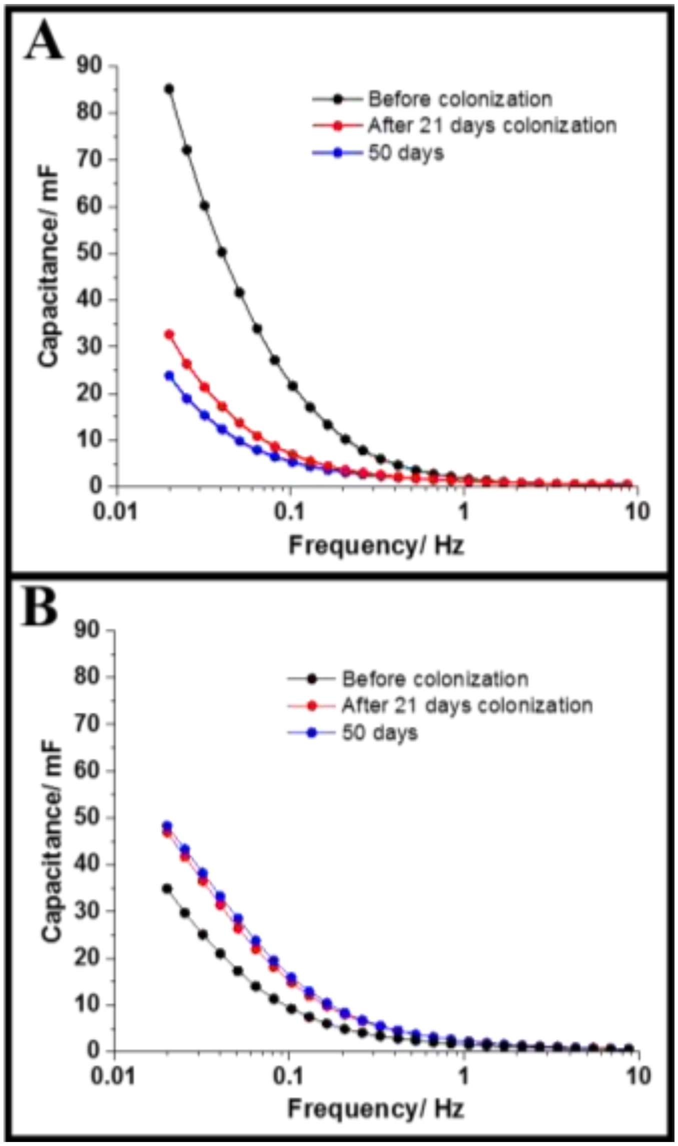

Figure 5.2.3. Bode Plots in terms of capacitance vs. frequency for BC-CNT (**A**) and BC-CNT-PANI (**B**) electrodes tested in MFC by a three-electrode setup before and after colonization.

Figures 5.2.2 and 5.2.3 revealed that BC-CNT and PANI modified BC-CNT electrodes presented different trends before colonization than after that. Before colonization, BC-

CNT-PANI, compared to BC-CNT, had lower capacitance and a more significant deviation from an ideal capacitor's behavior. Indeed, BC-CNT-PANI’s capacitance was 36 mF, in phase angle of -46°, while for the BC-CNT, the values were 87 mF and -52°, respectively.

However, after 21 days, the capacitance of BC-CNT reached 34 mF at a phase angle of -36°, and then after 50 days, the capacitance decreased to a lower value of 24 mF at -30°. On the other side, for the PANI modified BC-CNT, the capacitance of 49 mF at a phase angle of -55° was reported after 21 days. It also further increased to 50 mF at -60° after 50 days.

Therefore, the R_{ct} decreased, and the capacitive behavior and phase angle of BC-CNT-PANI improved with biofilm formation. In comparison, the opposite behavior was seen for BC-CNT. For better understanding, it should be noted that PANI is hydrophilic, and Thus, PANI coating may improve the nutrients transferring to the anodic biofilm. Hence, electrons and protons generation is enhanced, and thus, electrical charge increases. Furthermore, unlike CNTs featuring toxicity effects on bacteria [113, 114], PANI with biocompatible nature helps the anode surface bioactivity.

5.3. Using additional capacitive bio-anode as the negative electrode of MFC’s internal supercapacitor

The extra positive and negative charges, respectively, at the polarized cathode and anode surface, are balanced by negative and positive counter ions dissolved in SCMFC electrolyte. The ions move to the electrodes with opposite charges and make an electrochemical double layer (EDL) at the anode and cathode surface. This is the concept of internal supercapacitor in an MFC system which was previously introduced by Soavi et al. and Santoro et al. [104, 73]. The additional anode was BC-CNT-PANI which showed higher capacitance and lower resistance than those of BC-CNT. Because of higher activity of biofilm formed on PANI modified additional anode and thus more produced electrons on its surface compared to those on BC-CNT surface, coupling additional electrode as the negative electrode to the air-cathode provides an internal EDLC with high capacitance (Figure 5.3.1). This internal EDLC lets the SCMFC obtain high power output in a short-time discharging process.

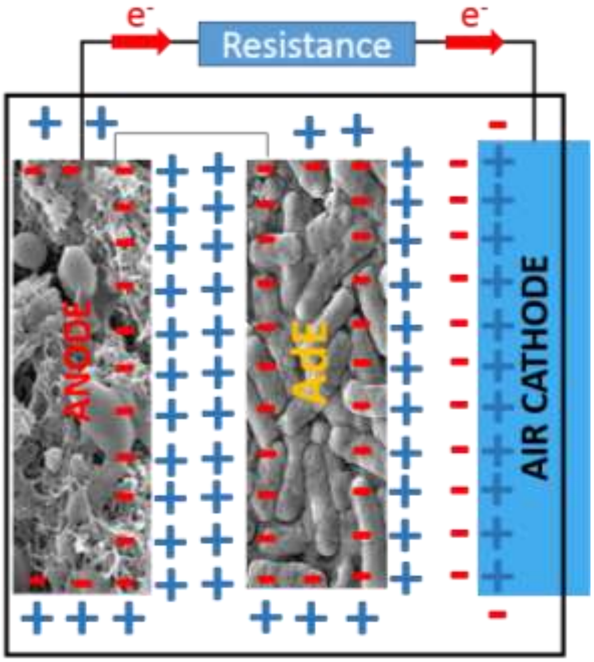

Figure 5.3.1. The concept of internal supercapacitor in an SCMFC.

5.4. CV and EIS of single electrodes and dual electrode

CV and EIS experiments were performed for BC-CNT, PANI modified BC-CNT, and short-circuited anodes ((BC-CNT & BC-CNT-PANI) after biofilm formation (50 days). Figure 5.4.1 presents the voltammetry experiment results at a scan rate of 0.2 mV/s and evidences BC-CNT-PANI's higher redox activity compared with BC-CNT's activity. For BC-CNT, PANI modified BC-CNT, and BC-CNT & BC-CNT-PANI, the voltammetric capacitance was 349 mF, 800 mF, and 1156 mF, respectively. The results were in accordance with the low frequencies of EIS data. Figure 5.4.2 indicates the Nyquist plots for BC-CNT, BC-CNT-PANI, short-circuited BC-CNT & BC-CNT-PANI.

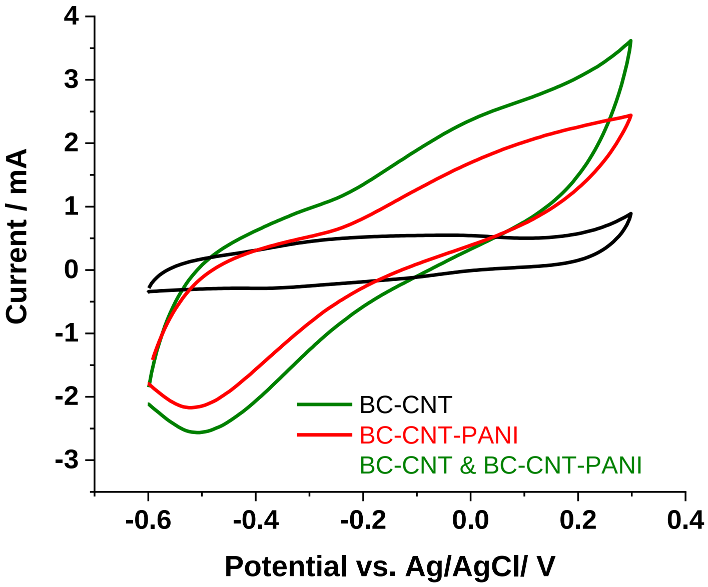

Figure 5.4.1. Cyclic voltammograms of different bio-anodes in SCMFC by a three-electrode setup after colonization

The Nyquist plots showed that R_{ct} for the case of BC-CNT & BC-CNT-PANI was 13.5Ω which was lower than the value of BC-CNT and PANI-modified electrode individually. It also further confirmed that PANI modified BC-CNT compared to BC-CNT had a lower R_{ct}.

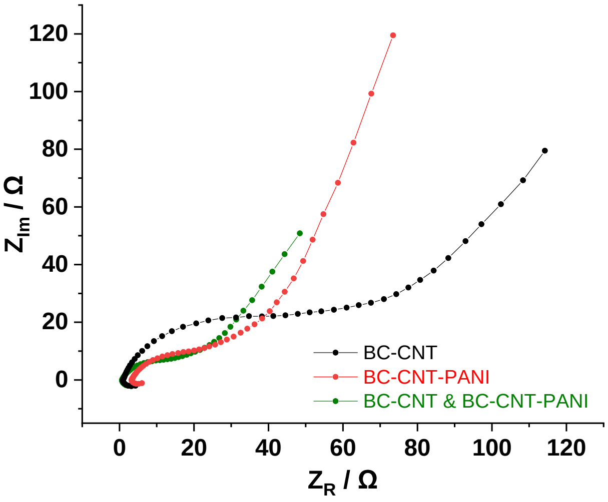

Figure 5.4.2. Nyquist plots for BC-CNT, BC-CNT-PANI individually and after short-circuiting in three-electrode mode after 50 days with active biofilm.

The CV provided in the inset of Figure 5.4.3 demonstrated that PANI modified glassy carbon, at pH=7, has a higher voltammetric current in Ar than in oxygen saturated solution. A similar result was already reported and showed that PANI at neutral pH is not electro-active to oxygen [115]. The CV test showed PANI-like exoelectrogens performing in neutral pH require anaerobic conditions for redox activity. According to this behavior, for neutral pH, PANI is compatible with exoelectrogens' living conditions. It may be a reason for PANI biocompatibility in anodic conditions of MFCs.

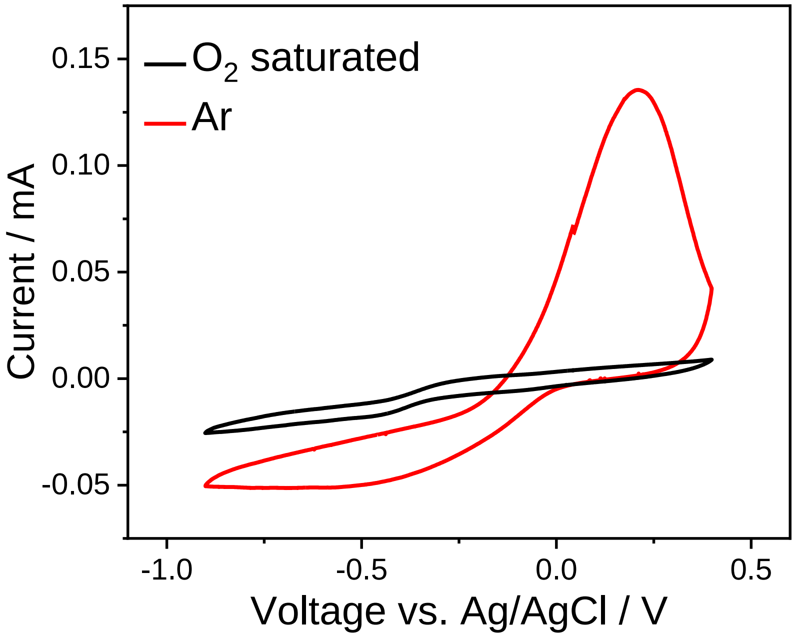

Figure 5.4.3. Cyclic voltammograms of PANI modified glassy carbon in oxygen and Ar saturated PBS by three-electrode mode

5.5 FESEM images of the biofilm formed on the BC-based anodes

Successful biofilm formation on BC-CNT and BC-CNT-PANI after colonization was shown in FESEM images of the anode. As can be observed, the density of biofilm formed on BC-CNT-PANI (Figure 5.5.1 B), compared to that on BC-CNT, is higher (Figure 5.5.1 A). This result can verify the PANI biocompatibility positive effect on biofilm growth highlighted by the EIS mentioned above analyses. Additionally, the microorganisms' average size on both BC-CNT and PANI coated BC-CNT observed in Figure 5.5.1 C&D respectively is between 2 μm and 3 μm.

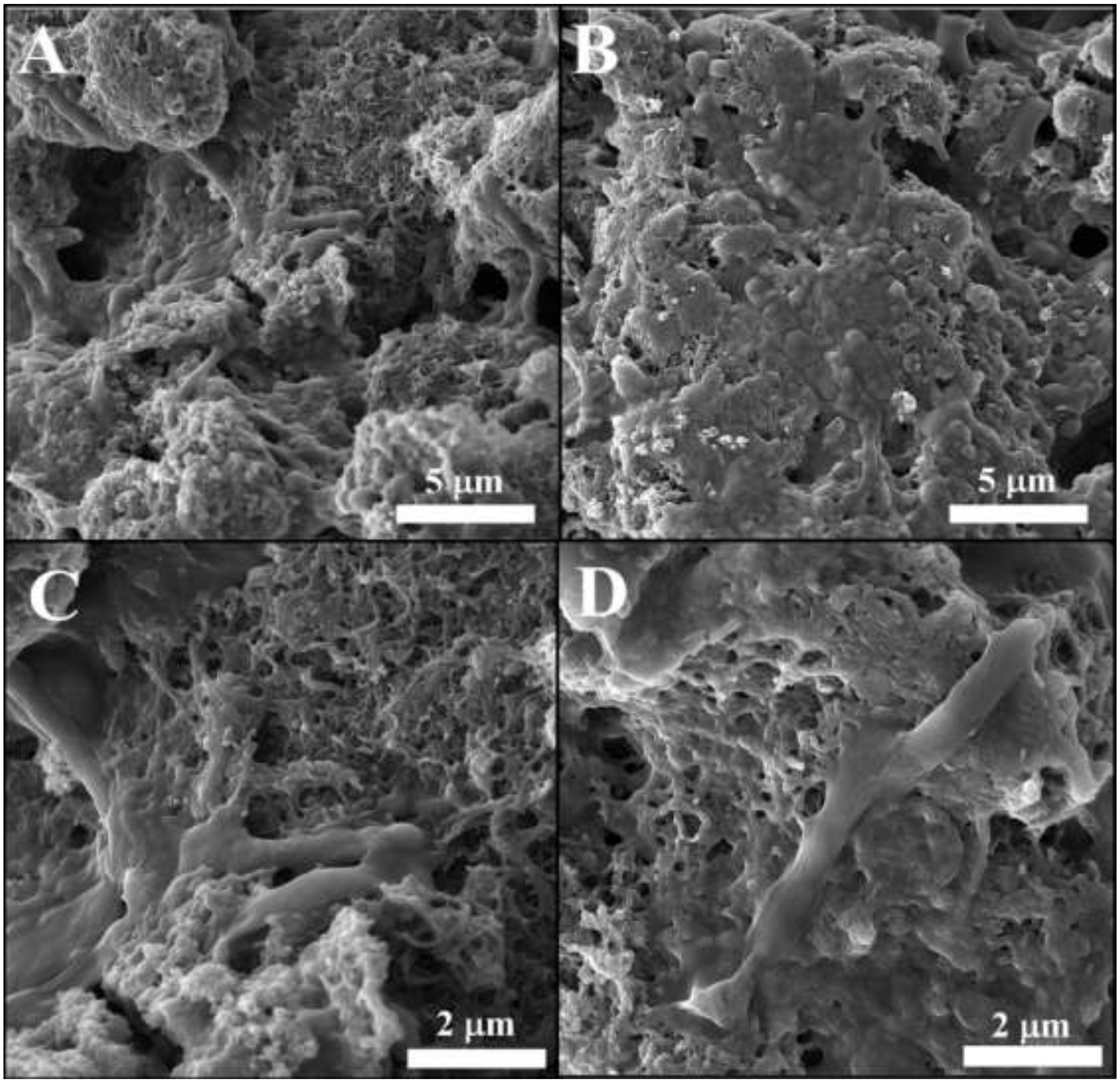

Figure 5.5.1. FE-SEM images of BC-CNT surface (A, C) and BC-CNT-PANI surface (B, D) after colonization and biofilm formation.

5.6 Polarization tests and power density

Figure 5.6.1 shows the polarization tests and power density results of the SCMFC in three cases for anode; BC-CNT, BC-CNT-PANI, and short-circuiting the anodes. Air-breathing cathode for all three instances was activated carbon coated SS mesh. The peak power density in the presence of BC-CNT was 270 mW/m^3. By PANI modification, the value increased to 330 mW/m^3. By the dual-anode, the power output of SCMFC was further enhanced to 435 mW/m^3. The result for the dual-anode case was expected as short-circuiting BC-CNT and PANI modified anode provides a higher surface of the active biofilm, lower R_{ct}, and finally higher capacitance. Short-circuiting the anodes increased the power density by 32% and 61% compared to single BC-CNT-PANI and single BC-CNT, respectively.

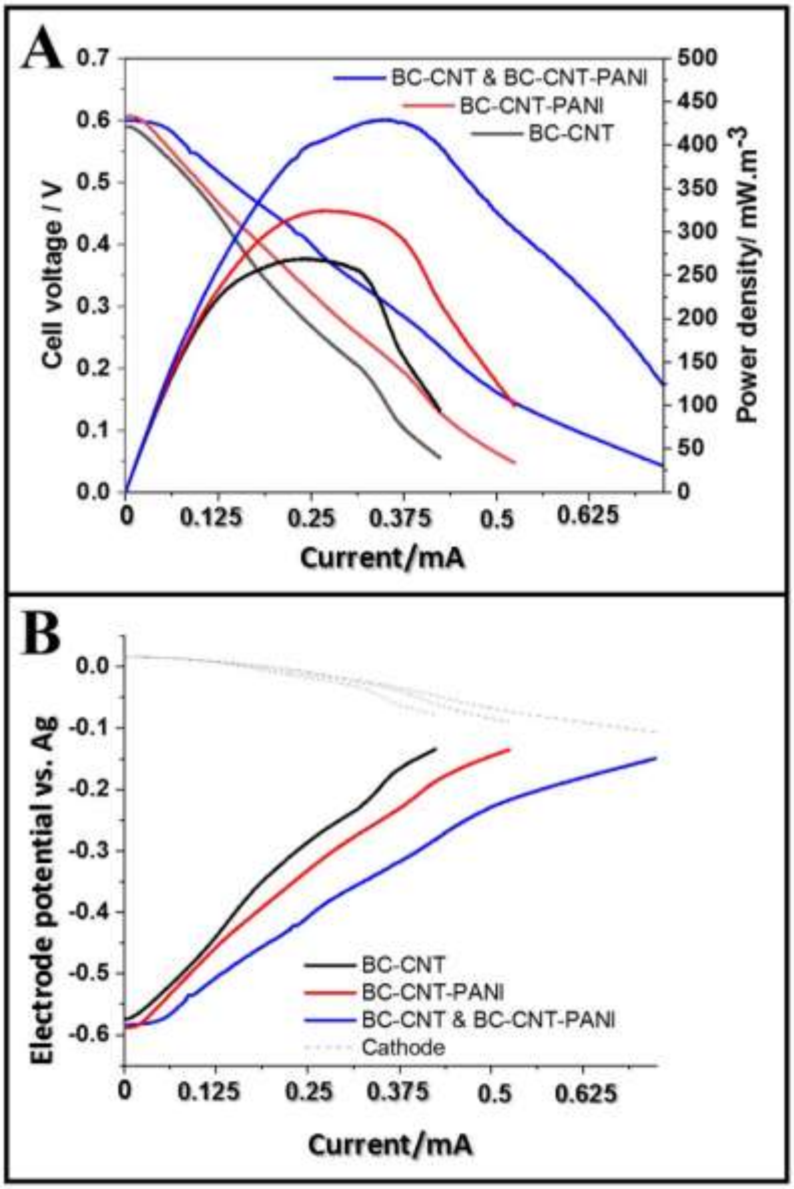

Figure 5.6.1. Polarization curve and power density of the full MFC cells (**A**) and single electrodes polarization curves (**B**) in the presence of different anodes (BC-CNT, BC-CNT-PANI, and dual-anode BC-CNT & BC-CNT-PANI) by LSV at 0.2 mV.s^{-1} after biofilm formation (50 days).

In polarization curves, the middle part slope is considered internal resistance of MFC or the system's equivalent series resistance (ESR). The SCMFC with BC-CNT-PANI featured an ESR around 1.12 kΩ compared to 1.33 kΩ for the cell in the presence of BC-CNT. While short-circuiting the anodes further improved the system and provided the lowest ESR of 0.84 kΩ. This pattern indicates that ESR is highly reliant on anode impedance, which, as seen above, demonstrates decrement in the order BC-CNT > BC-CNT-PANI> BC-CNT&BC-CNT-PANI.

In order to gain an understanding of the role of each electrode in cell efficiency, Figure 5.6.1 B demonstrates the trends in the potentials of cathode and anode during the polarization experiment. The cathodes' potential profiles nearly overlapped for the three cases, whereas the anode profile was distinct. In all three cells, the anodes' voltage drop was the major loss during the polarization analysis, which shows that the cathode did not restrict SCMFC performance. The anodes polarization' slope showed a decrease in the order BC-CNT > BC-CNT-PANI> BC-CNT&BC-CNT-PANI, i.e., like the trend seen for the complete cells.

5.7 Galvanostatic discharging

Similar to what was performed in the polarization test, GLV was also carried out in MFC for three different cases. GLV discharge was done during four distinct pulse times, including 0.1, 0.5, 1, and 2 s, by various pulse currents (0.5 mA to 15 mA with 0.5 mA steps). Figure 5.7.1 indicates the measured pulse power vs. discharging current at determined pulse times.

The trend of maximum pulse power generated by the SCMFC at distinct pulse times was similar to the curves obtained by LSV. Additionally, decreasing pulse time led to higher produced power. Short-circuited dual anodes generated the highest power output of 3.5 mW by 11 mA discharge current for a duration of 0.1 s. By the current of 4 mA discharged for 2 s, the same cell supplied 1.5 mW. All the GLV experiments showed that PANI-modified anode rather than bare BC-CNT could produce higher current and power. It can be due to the modified anode's higher capacitance, verified by EIS and CV experiments and discussed further below.

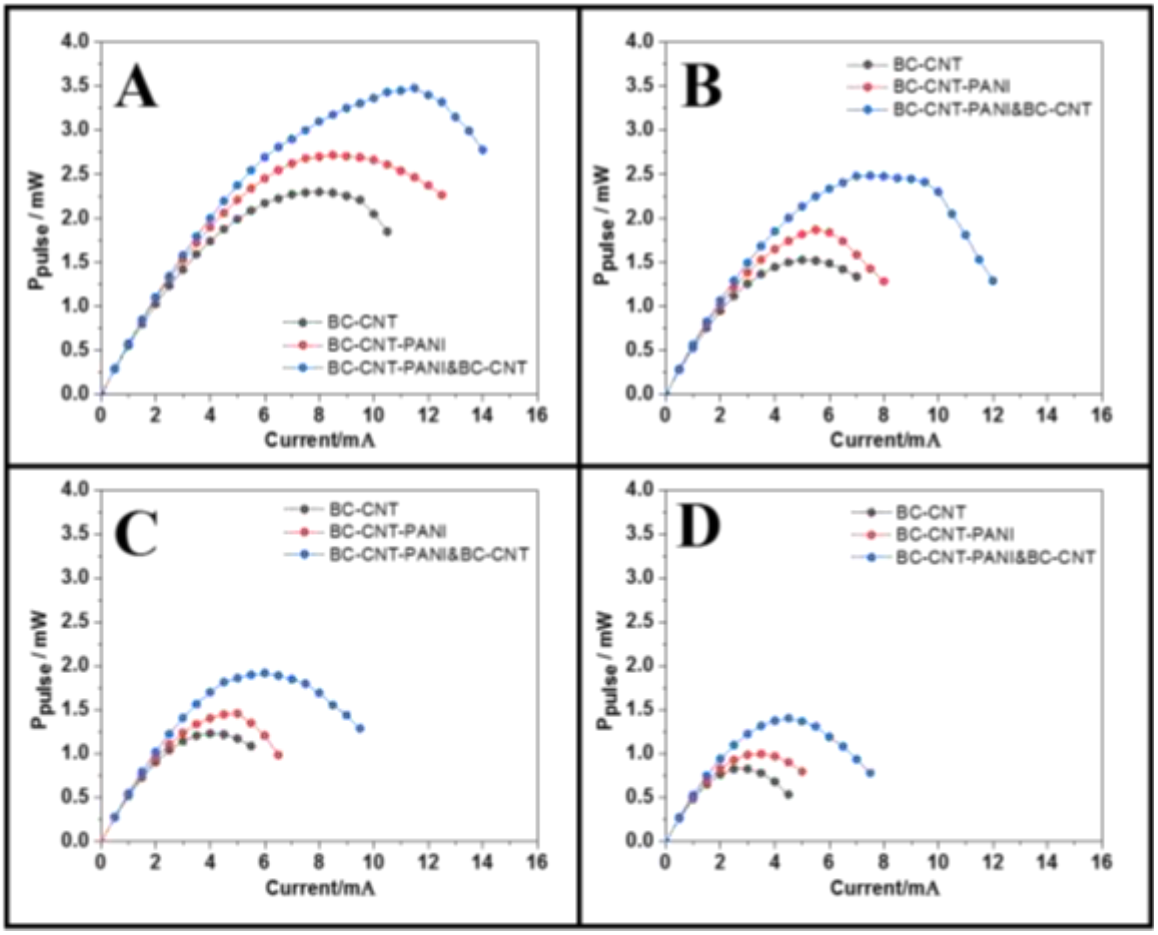

Figure 5.7.1. Pulse power delivered by MFC with BC-CNT, BC-CNT-PANI, and BC-CNT &BC-CNT-PANI anodes under GLV discharge with pulses of (**A**) 0.1s, (**B**) 0.5s, (**C**) 1s, and (**D**) 2s.

5.8 Ohmic and capacitive voltage drop

Figure 5.8.1 shows the variation in cell voltage of the MFCs in the presence of different anodes during 1 s of 3 mA discharging. As discharging begins, the voltage of the cell sharply decreases. The voltage drop (ΔV_{ohmic}) depends on the cell ESR. After the initial voltage drop, the potential decreases linearly per time due to the cell's "apparent capacitive" ($\Delta V_{capacitance}$). In GLV discharging, the SCMFC capacitance is related to the reciprocal of voltage vs. time plot slop (see Eq. 2.6.5.2)[116]. It is obvious that the initial voltage drop for BC-CNT, BC-CNT-PANI, and BC-CNT&BC-CNT-PANI are almost the same (ΔV_{ohmic} of 53 mV, 57 mV, and 46 mV, respectively). Unlike ΔV_{ohmic}, $\Delta V_{capacitance}$ significantly depended on the type of anode over 1 s discharging. The highest value was

217 mV recorded for the cell with BC-CNT. With PANI modified anode, $\Delta V_{capacitance}$ for the SCMFC was 150 mV, and with the dual anode, 104 mV was measured. Thus, the $\Delta V_{capacitance}$ of the cells further showed that the PANI coating enhanced the capacitance of the anode.

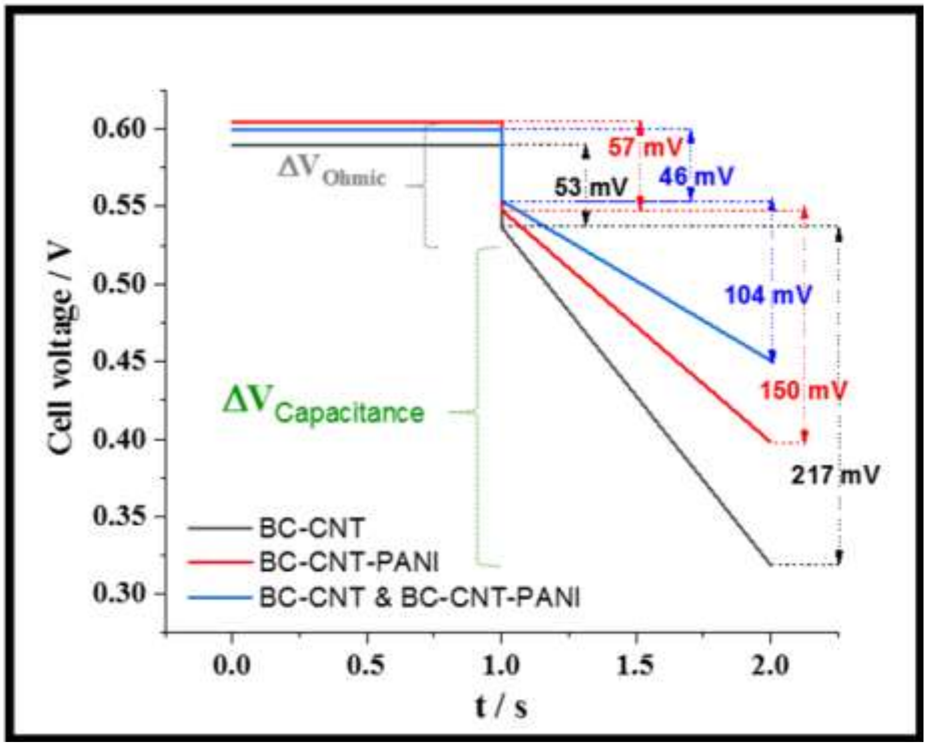

Figure 5.8.1. GLV discharges at 3 mA: Cell voltage profile under 1s pulses with the indication of the ohmic drop and capacitive voltage decrease during the pulse.

The capacitive voltage drop ($\Delta V_{capacitance}/t_{pulse}$) was also measured for various pulse times at 3mA, and the reverse values of the slope $(\Delta V_{capacitance}/t_{pulse})^{-1}$ are provided in Figure 5.8.2 A. It demonstrates that increasing pulse duration led to smaller slopes. Moreover, the slope at each pulse time decreased in the order BC-CNT> BC-CNT-PANI>BC-CNT&BC-CNT-PANI. The corresponding cell capacitances are reported in Figure 5.8.2 B, and they increase in the order BC-CNT< BC-CNT-PANI<BC-CNT&BC-CNT-PANI. The dependency of the capacitance on time can be explained by considering that in supercapacitive MFCs, two different types of processes occur at the same time: the faradic discharge and capacitive (or pseudocapacitance for PANI-based cell) discharge. The latter process is defined by the rapid formation of electrical double-layers at the

electrode/electrolyte interfaces. The former is related to the slow MFC redox processes, namely oxygen reduction at the air-breathing cathode and oxidation of organic compounds at the bio-anode.

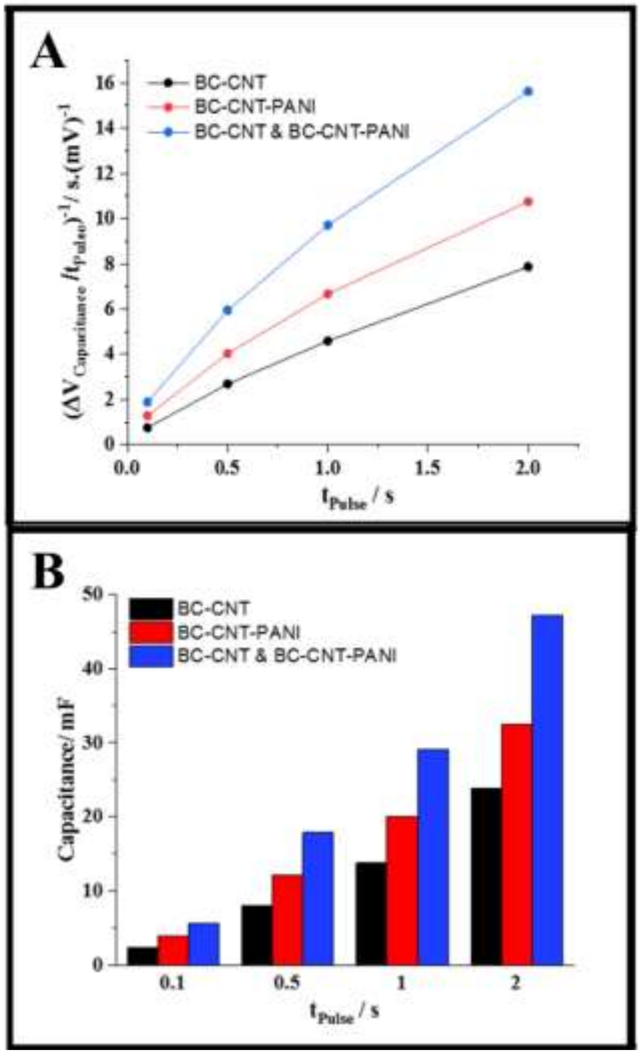

Figure 5.8.2. Capacitive voltage drop vs. different pulse time (**A**), cell capacitance vs. different pulse time (**B)** for the SCMFCs with BC-CNT, BC-CNT-PANI, and BC-CNT&BC-CNT-PANI anodes.

For short-duration pulses, MFC's voltage profile is mainly derived by its capacitive feature. Instead, at the longer duration, the main useful parameters on the MFC voltage profile are faradaic processes which are noticeable and actively contribute to sustaining the cell voltage and make less its decrease. This mixed behavior which is time-dependent has already been explained and defined as MFC's "apparent capacitance" [77].

5.9 MFC capacitance and power output

The capacitance effect on power production in SCMFCs is shown in Figure 5.9.1. The figure indicates the power vs. capacitance (calculated by Eq. 2.6.5.1 and Eq. 2.6.5.2, respectively). GLV discharging with a pulse duration of 2 s and various discharging currents were utilized in the curves. As a noticeable result, the higher capacitance of MFC led to generating higher power output by the cell. PANI modified anode by its positive impact on both biofilm activity and bio-anode's capacitive response indicated by CV and EIS results, presented the best power performance.

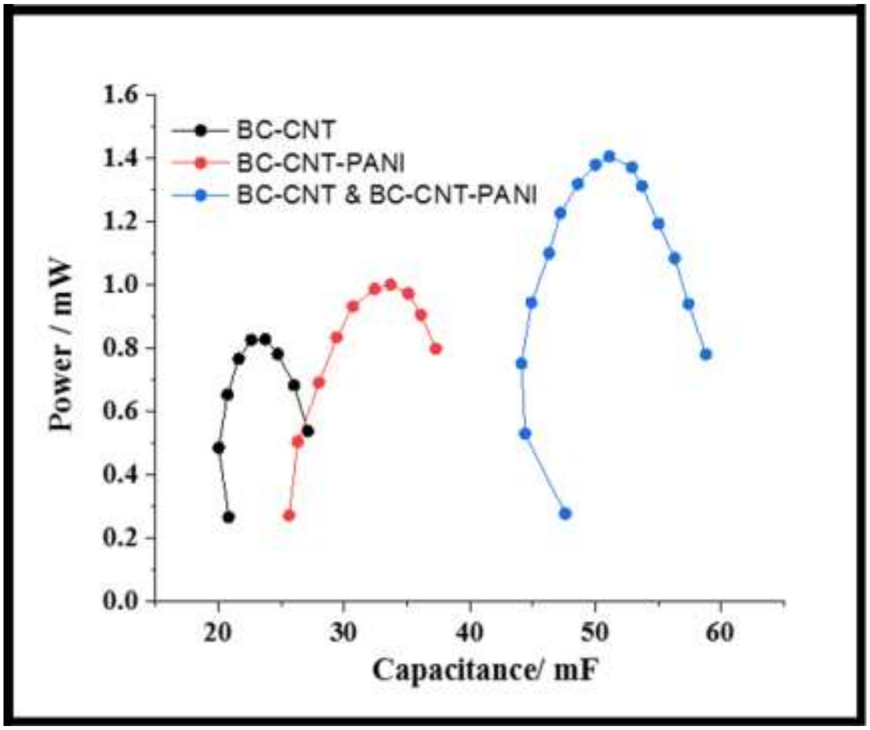

Figure 5.8.1. Power generation versus cell capacitance by different discharging currents and pulse time of 2s for the SCMFCs with BC-CNT, BC-CNT-PANI, and BC-CNT&BC-CNT-PANI anodes.

5.10 Conclusions

In this chapter, we suggested a pseudocapacitive bio-anode fabricated by BC, CNTs, and PANI. It was used as a flexible hydrogel bio-anode in an SCMFC with an air-breathing cathode. CNTs coated the thin BC membrane by using vacuum filtering without any binders. Then, PANI was electrochemically synthesized on the BC-CNT by fast and easy chronopotentiometry. CVs revealed the BC-CNT-PANI’s higher redox activity compared to that of BC-CNT. Impedance results demonstrated that the BC-CNT’s capacitance decreased by colonization, while for BC-CNT-PANI, that increased. Also, R_{ct} of BC-CNT and PANI modified BC-CNT after colonization showed an increment and decrement, respectively. Additionally, GLV discharges confirmed the higher capacitance of the BC-CNT-PANI anode. The slope of single electrode polarization curves revealed that the anodes were the main limiting factors in the cells. Biofilm formation effect on PANI and CNT's capacitance and its impact on power production of SCMFC was investigated in this thesis for the first time. Furthermore, a 'dual anode" made by short-circuiting BC-CNT and BC-CNT-PANI, increasing the total active surface of the anode, presented the highest capacitance and suggested an MFC with high power output.

Chapter 6

Conclusions

In this PhD thesis, two methods have been investigated in order to use cellulose based supercapacitors in Microbial fuel cell (MFC) technology. The first strategy is the use of capacitive cellulose based Membrane electrode assembly (MEA) air-breathing cathode and the second one is the use of capacitive bio-anode based on porous media hydrogel cellulose nanocomposites.

For the first part:

The fabricated MEA has water contact angle (WCA) of 85 ° for the surface exposed to the anolyte which results in providing lots of active sites on the MEA for oxygen, protons and electrons to meet each other for higher rate of oxygen reduction reaction (ORR). Bacterial cellulose (BC) has noticeably hydrophilic nature and performs as proton exchange membrane. In order to utilize BC in MEA structure, it also requires to become a hydrophobic surface for preventing leakage. Nano zycosil (NZ) has a vital role in the MEA structure as it changes hydrophilic BC (WCA of 49°) to a moderated hydrophobic surface. In this thesis, NZ is introduced as a hydrophobic agent for BC for the first time and as a cheap alternative to costly commercial hydrophobic agents like polytetrafluoroethylene. For other side of the MEA exposed to the air, carbon nanotubes (CNTs) make a homogeneous coating through a binder-less approach and form a monolithic MEA. The MEA compared to commercial gas diffusion electrode (GDE) shows lower oxygen cross-over which is beneficial to anaerobic condition of anodic biofilm. It was also proved through an electrochemical concept. Low cell voltage by reversed sides of the MEA implied on barrier property of the MEA against oxygen transfer. Therefore, BC-CNT-NZ with the mentioned physical and chemical features of its bulk and surfaces can be a suitable MEA for MFCs.

Nyquist plots showed much lower charge transfer resistance (R_{ct}) for BC-CNT NZ air-cathode compared to that for the GDE. Also, the capacitance calculated by impedance analysis demonstrated much higher capacitance of the MEA than that of the GDE. It is attributed to high capacitance of CNT as capacitive carbon compared to Vulcan used in the GDE.

Also, by comparing the slope of middle part of polarization curves for the two air-cathodes, internal resistance of the system with BC-CNT-NZ MEA was lower than that with the GDE.

Columbic efficiency of the cell with MEA was three folds than that with GDE which is due to perfect anaerobic condition and higher current density of the MEA MFC

The higher catalytic activity of MEA in comparison with the GDE is explained by the catalytic activity of high surface area CNT in ORR and the success of the BC-NZ in transferring protons to ORR active sites at BC-CNT interface.

Impedance spectroscopy, cyclic voltammetry showed that the MEA capacitance is higher than the commercial GDE and also galvanostatic discharging indicated that the cell capacitive behavior increased by the use of BC-CNT-NZ.

By enhancing the cell capacitance, ORR catalytic activity and also decreasing cell resistance in presence of the cellulosic MEA, the cell power density was also improved and reached the best performance of the BC-based MEAs for MFC system.

For the second part:

BC-CNT and electro-polymerized PANI modified BC-CNT as bio-anodes utilized in supercapacitive MFCs, showed different electrochemical behavior before and anode colonization.

R_{ct} of PANI modified anode was higher than that of BC-CNT before colonization. PANI is a conductive polymer while in neutral pH like MFC media its conductivity is very low. On the other hand, after colonization of bacteria on the anodes, the story became different and R_{ct} of BC-CNT-PANI decreased while that of BC-CNT increased. Finally modified electrode showed lower resistance than the bare bio-anode.

For the capacitance of the BC based anode, before and after colonization PANI modified electrode showed lower and higher capacitance, respectively compared to BC-CNT.

PANI biocompatibility compared to toxicity of CNTs to anodic biofilm can explain the mentioned behavior of both resistance and capacitance of the anodes.

PANI modified electrode showed higher generated current in non-dissolved oxygen case rather than in saturated oxygen case in buffer solution and neutral pH. Accordingly, PANI may be a good choice for anaerobic anodic condition in neutral pH media.

PANI modified anode compared to BC-CNT showed lower internal resistance and also higher power density.

Using colonized BC-CNT-PANI as additional anode through short-circuiting that to BC-CNT enhanced the capacitance of the system by making an internal supercapacitor in the MFC

Galvanostatic discharging showed that longer duration of discharging gives higher cell capacitance while shorter discharging duration results in higher power output.

Finally PANI coating and using additional capacitive PANI modified anode could enhance both capacitance and power output of MFC as a supercapacitive system.

Bibliography

1. Luzzi, A. and A. Luzzi, *In Pursuit of the Future: 25 years of IEA Research towards the realisation of Hydrogen Energy Systems*. 2004: Energy Strategies.
2. Farhad, S., M. Saffar‐ Avval, and M. Younessi‐ Sinaki, International journal of energy research, 2008. **32**(1): p. 1-11.
3. Sims, R.E., Mitigation and Adaptation Strategies for Global Change, 2003. **8**(4): p. 349-370.
4. Twidell, J. and T. Weir, *Renewable energy resources*. 2015: Routledge.
5. Demirbas, A., Energy Edu. Sci. Technol, 2000. **6**: p. 19-40.
6. Panwar, N., S. Kaushik, and S. Kothari, Renewable and sustainable energy reviews, 2011. **15**(3): p. 1513-1524.
7. Kralova, I. and J. Sjöblom, Journal of Dispersion Science and Technology, 2010. **31**(3): p. 409-425.
8. González, A., E. Goikolea, J.A. Barrena, and R. Mysyk, Renewable and Sustainable Energy Reviews, 2016. **58**: p. 1189-1206.
9. Sharma, K., A. Arora, and S.K. Tripathi, Journal of Energy Storage, 2019. **21**: p. 801-825.
10. Shown, I., A. Ganguly, L.C. Chen, and K.H. Chen, Energy Science & Engineering, 2015. **3**(1): p. 2-26.
11. Winter, M. and R.J. Brodd, *What are batteries, fuel cells, and supercapacitors?* 2004, ACS Publications.
12. Brousse, T., D. Bélanger, and J.W. Long, J. Electrochem. Soc, 2015. **162**(5): p. A5185-A5189.
13. Jayalakshmi, M. and K. Balasubramanian, Int. J. Electrochem. Sci, 2008. **3**(11): p. 1196-1217.
14. Halper, M.S. and J.C. Ellenbogen, The MITRE Corporation, McLean, Virginia, USA, 2006: p. 1-34.
15. Frackowiak, E. and F. Beguin, Carbon, 2001. **39**(6): p. 937-950.
16. Conway, B.E., Electrochemistry Encyclopedia, 2003.
17. Yang, Z., J. Tian, Z. Yin, C. Cui, W. Qian, and F. Wei, Carbon, 2019. **141**: p. 467-480.
18. Lokhande, C., D. Dubal, and O.-S. Joo, Current Applied Physics, 2011. **11**(3): p. 255-270.

19. Skotheim, T.A. and J. Reynolds, *Conjugated polymers: theory, synthesis, properties, and characterization*. 2006: CRC press.

20. Heeger, A.J., Angewandte Chemie International Edition, 2001. **40**(14): p. 2591-2611.

21. Chawla, P.R., I.B. Bajaj, S.A. Survase, and R.S. Singhal, Food Technology and Biotechnology, 2009. **47**(2): p. 107-124.

22. Ummartyotin, S., J. Juntaro, M. Sain, and H. Manuspiya, Industrial Crops and Products, 2012. **35**(1): p. 92-97.

23. Razaq, A., L. Nyholm, M. Sjödin, M. Strømme, and A. Mihranyan, Advanced Energy Materials, 2012. **2**(4): p. 445-454.

24. Wang, Z., P. Tammela, P. Zhang, M. Strømme, and L. Nyholm, Journal of Materials Chemistry A, 2014. **2**(21): p. 7711-7716.

25. Wang, Z., P. Tammela, M. Strømme, and L. Nyholm, Advanced Energy Materials, 2017. **7**(18): p. 1700130.

26. Anothumakkool, B., R. Soni, S.N. Bhange, and S. Kurungot, Energy & Environmental Science, 2015. **8**(4): p. 1339-1347.

27. Wang, Z., P. Tammela, M. Strømme, and L. Nyholm, Nanoscale, 2015. **7**(8): p. 3418-3423.

28. Mashkour, M., M. Rahimnejad, and M. Mashkour, Journal of Power Sources, 2016. **325**: p. 322-328.

29. Mashkour, M., M. Rahimnejad, M. Mashkour, G. Bakeri, R. Luque, and S.E. Oh, ChemElectroChem, 2017. **4**(3): p. 648-654.

30. Liu, L., Z. Niu, L. Zhang, W. Zhou, X. Chen, and S. Xie, Advanced Materials, 2014. **26**(28): p. 4855-4862.

31. Williams, M.C., J.P. Strakey, and W.A. Surdoval, Journal of power sources, 2005. **143**(1-2): p. 191-196.

32. Potter, M.C., Proceedings of the royal society of London. Series b, containing papers of a biological character, 1911. **84**(571): p. 260-276.

33. Cohen, B., J. Bacteriol, 1931. **21**(1): p. 18-19.

34. Rahimnejad, M., G. Najafpour, A. Ghoreyshi, T. Jafari, and F. Haghparast, Linnaeus Eco-Tech, 2010: p. 627-635.

35. Jafary, T., M. Rahimnejad, A.A. Ghoreyshi, G. Najafpour, F. Hghparast, and W.R.W. Daud, Energy conversion and management, 2013. **75**: p. 256-262.

36. Mashkour, M. and M. Rahimnejad, Biofuel Res. J, 2015. **2**(4): p. 296-300.

37. Nelson, D.L., A.L. Lehninger, and M.M. Cox, *Lehninger principles of biochemistry*. 2008: Macmillan.

38. Ivars-Barceló, F., A. Zuliani, M. Fallah, M. Mashkour, M. Rahimnejad, and R. Luque, Applied Sciences, 2018. **8**(7): p. 1184.

39. Jiang, Y., Q. Liang, N. Chu, W. Hao, L. Zhang, G. Zhan, D. Li, and R.J. Zeng, Science of The Total Environment, 2020. **741**: p. 140198.

40. Masoudi, M., M. Rahimnejad, and M. Mashkour, Electrochimica Acta, 2020: p. 136168.

41. Logan, B.E., Nature Reviews Microbiology, 2009. **7**(5): p. 375-381.

42. Logan, B.E., B. Hamelers, R. Rozendal, U. Schröder, J. Keller, S. Freguia, P. Aelterman, W. Verstraete, and K. Rabaey, Environmental science & technology, 2006. **40**(17): p. 5181-5192.

43. Rahimnejad, M., G. Najafpour, A. Ghoreyshi, M. Shakeri, and H. Zare, International journal of hydrogen energy, 2011. **36**(20): p. 13335-13341.

44. Mecheri, B., R. Gokhale, C. Santoro, M.A. Costa de Oliveira, A. D'Epifanio, S. Licoccia, A. Serov, K. Artyushkova, and P. Atanassov, ACS applied energy materials, 2018. **1**(10): p. 5755-5765.

45. Cheng, S., H. Liu, and B.E. Logan, Environmental science & technology, 2006. **40**(1): p. 364-369.

46. Bard, A.J. and L.R. Faulkner, Electrochemical Methods, 2001. **2**(482): p. 580-632.

47. Rozendal, R.A., F. Harnisch, A. Jeremiasse, and U. Schroder, 2010.

48. Scott, K. and E.H. Yu, *Microbial electrochemical and fuel cells: fundamentals and applications*. 2015: Woodhead Publishing.

49. Yeager, E., Journal of Molecular Catalysis, 1986. **38**(1-2): p. 5-25.

50. Rahimnejad, M., G. Bakeri, G. Najafpour, M. Ghasemi, and S.-E. Oh, Biofuel Research Journal, 2014. **1**(1): p. 7-15.

51. Theodosiou, P., J. Greenman, and I. Ieropoulos, International Journal of Hydrogen Energy, 2019. **44**(9): p. 4450-4462.

52. Oliot, M., L. Etcheverry, A. Mosdale, R. Basséguy, M.-L. Delia, and A. Bergel, Journal of Power Sources, 2017. **356**: p. 389-399.

53. Aferta, L., G. Syahbirin, and S. Mulijani, International Journal for Research in Applied Sciences and Biotechnology (IJRASB), 2018. **5**(3): p. 9-14.

54. Kodali, M., S. Herrera, S. Kabir, A. Serov, C. Santoro, I. Ieropoulos, and P. Atanassov, Electrochimica acta, 2018. **265**: p. 56-64.

55. Aleksejeva, O., F. Barrière, Z. Blum, L. Bouffier, W.-R. Cai, S. Cirovic, N.L. Costa, S. Dong, M. Etienne, and M. Falk, *Bioelectrochemistry: Design and Applications of Biomaterials*. 2019: Walter de Gruyter GmbH & Co KG.
56. Santoro, C., A. Agrios, U. Pasaogullari, and B. Li, International journal of hydrogen energy, 2011. **36**(20): p. 13096-13104.
57. Ci, J., C. Cao, S. Kuga, J. Shen, M. Wu, and Y. Huang, ACS Sustainable Chemistry & Engineering, 2017. **5**(11): p. 9614-9618.
58. Jwa, E., Y.-M. Yun, H. Kim, N. Jeong, S.-C. Park, and J.-Y. Nam, International Journal of Hydrogen Energy, 2019. **44**(2): p. 652-660.
59. Kim, K.-Y., W. Yang, Y. Ye, N. LaBarge, and B.E. Logan, Bioresource technology, 2016. **208**: p. 58-63.
60. Leong, J.X., W.R.W. Daud, M. Ghasemi, K.B. Liew, and M. Ismail, Renewable and Sustainable Energy Reviews, 2013. **28**: p. 575-587.
61. Angioni, S., L. Millia, G. Bruni, D. Ravelli, P. Mustarelli, and E. Quartarone, Journal of Power Sources, 2017. **348**: p. 57-65.
62. Mashkour, M., T. Kimura, M. Mashkour, F. Kimura, and M. Tajvidi, ACS applied materials & interfaces, 2018. **11**(1): p. 1538-1545.
63. Li, S., D. Huang, J. Yang, B. Zhang, X. Zhang, G. Yang, M. Wang, and Y. Shen, Nano Energy, 2014. **9**: p. 309-317.
64. Mashkour, M., Z. Moradabadi, and A. Khazaeian, Journal of Applied Polymer Science, 2017. **134**(30): p. 45118.
65. Sheykhnazari, S., T. Tabarsa, M. Mashkour, A. Khazaeian, and A. Ghanbari, International journal of biological macromolecules, 2018. **120**: p. 2115-2122.
66. Shi, Z., G.O. Phillips, and G. Yang, Nanoscale, 2013. **5**(8): p. 3194-3201.
67. Poli, F., G. Spina, A. Terella, M. Mashkour, M.L. Focarete, D. Fabiani, C. Santato, D. Momodu, N. Manyala, and F. Soavi. *Green Materials for Sustainable Supercapacitors*. in *Meeting Abstracts*. 2019. The Electrochemical Society.
68. Wang, X., D. Kong, Y. Zhang, B. Wang, X. Li, T. Qiu, Q. Song, J. Ning, Y. Song, and L. Zhi, Nanoscale, 2016. **8**(17): p. 9146-9150.
69. Mashkour, M., M. Sharifinia, H. Yousefi, and E. Afra, Carbohydrate polymers, 2018. **202**: p. 504-512.
70. Lv, P., Q. Feng, Q. Wang, D. Li, J. Zhou, and Q. Wei, Fibers and Polymers, 2016. **17**(11): p. 1858-1865.

71. Li, X., P. Lv, Y. Yao, Q. Feng, A. Mensah, D. Li, and Q. Wei, Chemical Engineering Journal, 2020. **379**: p. 122316.

72. Vilela, C., D.M. Cordeiro, J.V. Boas, P. Barbosa, M. Nolasco, P.D. Vaz, S. Rudić, P. Ribeiro-Claro, A.J. Silvestre, and V.B. Oliveira, Bioresource Technology Reports, 2019: p. 100376.

73. Santoro, C., F. Soavi, A. Serov, C. Arbizzani, and P. Atanassov, Biosensors and Bioelectronics, 2016. **78**: p. 229-235.

74. Soavi, F. and C. Santoro, Current Opinion in Electrochemistry, 2020.

75. Wang, H., J.-D. Park, and Z.J. Ren, Environmental science & technology, 2015. **49**(6): p. 3267-3277.

76. Dewan, A., H. Beyenal, and Z. Lewandowski, Environmental science & technology, 2009. **43**(12): p. 4600-4605.

77. Poli, F., J. Seri, C. Santoro, and F. Soavi, ChemElectroChem, 2020. **7**(4): p. 893-903.

78. Santoro, C., F. Soavi, C. Arbizzani, A. Serov, S. Kabir, K. Carpenter, O. Bretschger, and P. Atanassov, Electrochimica acta, 2016. **220**: p. 672-682.

79. Soavi, F. and C. Santoro, Current Opinion in Electrochemistry, 2020. **22**: p. 1-8.

80. Deeke, A., T.H. Sleutels, H.V. Hamelers, and C.J. Buisman, Environmental science & technology, 2012. **46**(6): p. 3554-3560.

81. Deeke, A., T.H. Sleutels, A. Ter Heijne, H.V. Hamelers, and C.J. Buisman, Journal of power sources, 2013. **243**: p. 611-616.

82. Malvankar, N.S., T. Mester, M.T. Tuominen, and D.R. Lovley, 2012.

83. Agnès, C., M. Holzinger, A. Le Goff, B. Reuillard, K. Elouarzaki, S. Tingry, and S. Cosnier, Energy & Environmental Science, 2014. **7**(6): p. 1884-1888.

84. Jannelli, N., R.A. Nastro, V. Cigolotti, M. Minutillo, and G. Falcucci, Applied Energy, 2017. **192**: p. 543-550.

85. Nam, S., A.D. French, B.D. Condon, and M. Concha, Carbohydrate polymers, 2016. **135**: p. 1-9.

86. DeGarmo, E.P., J.T. Black, R.A. Kohser, and B.E. Klamecki, *Materials and process in manufacturing*. 1997: Prentice Hall Upper Saddle River.

87. Malaie, K., C. Jeyabharathi, H. Wulff, M.R. Ganjali, F. Soavi, and F. Scholz, New Journal of Chemistry, 2018. **42**(24): p. 20156-20162.

88. Bard, A.J., L.R. Faulkner, J. Leddy, and C.G. Zoski, *Electrochemical methods: fundamentals and applications*. Vol. 2. 1980: wiley New York.

89. Houghton, J., C. Santoro, F. Soavi, A. Serov, I. Ieropoulos, C. Arbizzani, and P. Atanassov, Bioresource technology, 2016. **218**: p. 552-560.

90. Santoro, C., F.B. Abad, A. Serov, M. Kodali, K.J. Howe, F. Soavi, and P. Atanassov, Applied energy, 2017. **208**: p. 25-36.

91. Cao, X., P. Liang, X. Song, Y. Wang, Y. Qiu, and X. Huang, Science China Technological Sciences, 2019. **62**(10): p. 1703-1709.

92. Zanini, M., A. Lavoratti, L.K. Lazzari, D. Galiotto, M. Pagnocelli, C. Baldasso, and A.J. Zattera, Cellulose, 2017. **24**(2): p. 769-779.

93. Sai, H., R. Fu, L. Xing, J. Xiang, Z. Li, F. Li, and T. Zhang, ACS applied materials & interfaces, 2015. **7**(13): p. 7373-7381.

94. Phuong, H.T., N.K.D. Hong, and D.T. Ngo.

95. Siuda, J., W. Perdoch, B. Mazela, and M. Zborowska, Materials, 2019. **12**(12): p. 2006.

96. Tsalagkas, D., R. Lagaňa, I. Poljanšek, P. Oven, and L. Csoka, Ultrasonics sonochemistry, 2016. **28**: p. 136-143.

97. Mashkour, M., M. Tajvidi, F. Kimura, H. Yousefi, and T. Kimura, ACS applied materials & interfaces, 2014. **6**(11): p. 8165-8172.

98. Tabarsa, T., S. Sheykhnazari, A. Ashori, M. Mashkour, and A. Khazaeian, International journal of biological macromolecules, 2017. **101**: p. 334-340.

99. Poletto, M., A.J. Zattera, and R.M. Santana, Journal of Applied Polymer Science, 2012. **126**(S1): p. E337-E344.

100. Kannangara, D. and W. Shen, Colloids and Surfaces A: Physicochemical and Engineering Aspects, 2008. **330**(2-3): p. 151-160.

101. Fernandes, M., M. Gama, F. Dourado, and A.P. Souto, Microbial Biotechnology, 2019. **12**(4): p. 650-661.

102. Sekar, N. and R.P. Ramasamy, J Microb Biochem Technol S, 2013. **6**(2).

103. Berthier, F., J.-P. Diard, and R. Michel, Journal of Electroanalytical Chemistry, 2001. **510**(1-2): p. 1-11.

104. Soavi, F., L.G. Bettini, P. Piseri, P. Milani, C. Santoro, P. Atanassov, and C. Arbizzani, Journal of power sources, 2016. **326**: p. 717-725.

105. Santoro, C., X.A. Walter, F. Soavi, J. Greenman, and I. Ieropoulos, Electrochimica Acta, 2019. **307**: p. 241-252.

106. Biffinger, J.C., R. Ray, B. Little, and B.R. Ringeisen, Environmental science & technology, 2007. **41**(4): p. 1444-1449.

107. Ko, Y., H. Oh, and H. Lee, J Microb Biochem Technol, 2015. **7**(3): p. 145-151.

108. Wang, Z. and B. Lim, Environmental technology, 2017. **38**(8): p. 979-984.

109. Marzorati, S., A. Schievano, A. Colombo, G. Lucchini, and P. Cristiani, Journal of Cleaner Production, 2018. **170**: p. 1167-1176.

110. Vilela, C., A.C. Silva, E.M. Domingues, G. Gonçalves, M.A. Martins, F.M. Figueiredo, S.A. Santos, and C.S. Freire, Carbohydrate Polymers, 2020. **230**: p. 115604.

111. Ramasamy, R.P., V. Gadhamshetty, L.J. Nadeau, and G.R. Johnson, Biotechnology and bioengineering, 2009. **104**(5): p. 882-891.

112. Nègre, L., B. Daffos, P.-L. Taberna, and P. Simon, Journal of the Electrochemical Society, 2015. **162**(5): p. A5037-A5040.

113. Zhu, B., X. Xia, N. Xia, S. Zhang, and X. Guo, Environmental science & technology, 2014. **48**(7): p. 4086-4095.

114. Luongo, L.A. and X.J. Zhang, Journal of hazardous materials, 2010. **178**(1-3): p. 356-362.

115. Cui, C. and J.Y. Lee, Journal of Electroanalytical Chemistry, 1994. **367**(1-2): p. 205-212.

116. Caizán-Juanarena, L., C. Borsje, T. Sleutels, D. Yntema, C. Santoro, I. Ieropoulos, F. Soavi, and A. ter Heijne, Biotechnology advances, 2020. **39**: p. 107456.